PARAMETRIC VIBRATION OF COMPOSITE BEAMS WITH INTEGRATED SHAPE MEMORY ALLOY ELEMENTS

By

Xiangrong Su

A doctoral thesis submitted in fulfilment of the requirements for the award of Doctor of Philosophy (PhD) of the University of Glasgow

Supervisor: James Watt Professor Matthew P. Cartmell

Dedication

To my family

Copyright

Abstract

This research is concerned with parametric vibration in composite beam structures with shape memory alloy elements. As a precursor to this investigation, a flexible steel beam of rectangular uniform cross-section is considered with a lumped end mass under a parametric excitation. A single frequency harmonic excitation in the vertical direction is applied to the system. As an extension of previsouly developed model by Cartmell (1990) and Forehand and Cartmell (2001), three nonlinear equations of motion, representing the first and second bending modes and the first torsion modes, are derived by recourse to the Lagrangian formulation. The variables in the equations of motions are $u_1(t)$, $u_2(t)$ and $\phi_1(t)$ respectively. They are coupled together and various nonlinearities appear in the equations. The three equations are used to predict different parametric resonances of the form $\Omega \approx 2\omega_1$, $\Omega \approx 2\omega_2$, $\Omega \approx \omega_1 + \omega_2$ by application of the perturbation method of multiple scales. Expressions for the transition curves for the three resonances have been derived which show the regions of stable and unstable solutions in a detuning parameter-excitation amplitude plane. Very close agreement is obtained between theoretical and experimental results for all the three resonance conditions. Laboratory tests confirm that these instabilities are bounded in practice by nonlinear effects.

To investigate the effects of shape memory alloy on the dynamical properties of a composite material beam structure, two shape memory alloy strips are centrally-bonded to a glass epoxy beam with a lumped end mass. The two SMA strips are theoretically pre-strained and heated up to their full austenitic phase, and shown to generate large recovery forces due to this phase transformation. The forces are considered as compressive forces, and a theoretical model is introduced to evaluate the influences of the forces on the natural frequencies and the bending modes of the composite beam structure. The results show that the increase of the forces decrease the natural frequencies and reduce the excursion of the first and second bending modes. The beam system is then subjected to a vertical excitation. In order to utilize the Lagrangian formulation once again, the generalised forces corresponding to the generalised coordinates $u_1(t)$, $u_2(t)$ and $\phi_1(t)$ are derived in terms of the SMA recovery force. The three equations of motion of the free lateral vibration of the beam system are then derived. Three different parametric resonances are also predicted. Further

study shows that the increase of the magnitude of the recovery force results in an increase of the instability region.

An experimental investigation is conducted on two composite beam structures and each with an end mass, one with two centrally-bonded shape memory alloy (SMA) strips and the other with two diagonally-bonded SMA strips. The study suggests that when the strips are activated, the central-strip configuration can increase the natural frequencies of the bending modes noticeably more than the diagonal-strip one under certain circumstances, whilst the diagonal-strip configuration can easily be seen to change the frequencies of the torsion modes than the central-strip set-up.

Acknowledgement

“Although we know there's much to fear, we were moving mountains long before we knew we could……now I'm standing here, my heart's so full I can't explain.” The words were out from my heart when I was going to write this part. I cannot help giving special recognitions to the following colleagues and friends as angles God sent out to help me moved this mountain and warmed me throughout the journey.

First and foremost, James Watt Professor Matthew Philip Cartmell. It was Matthew who was instrumental in finding the Phemister Scholarship for me to come into Glasgow and make this journey possible. Also, his immeasurable contribution through the gift of knowledge, advice and guidance over the last three years is greatly appreciated. I really couldn’t have asked better supervision. It is my honour to work for a highly respected professor who is undoubtedly one of the leading names in parametric vibrations in the world.

A special thanks to Dr. David Forehand, for helping me settle down during the first year when I came in. Without his input, time and expertise to many aspects of this research, it would not have been as successful.

I am also very appreciative of Mr. Brian Robb and Mr. Bernard Hoey, for their incorporating my demanding needs for technician time and assistance throughout my experimental work. In addition, Mr Kenny Stevenson and Mr Walter Robinson, for their support with the computer packages I used. I also wish to acknowledge Dr. Arthur Whittaker for lending me his book. The book helped me make a progress and move on quickly (a smile face). An acknowledgement also goes to Mrs. Kirstin Heggie, an international student advisor, she was very nice and helpful when I applied to extend my student visa.

In connection with my research, I thank Mr. Marcin Bochenski and Prof Warminski, whilst doing the experiments in Lublin University of Technology in Poland, provided advice and assistance on hammer impact tests. I am very grateful for their hospitality when I was there.

Finally, I like to say a huge thanks to my family and friends. My most loved grandparents, they both passed away just a few months before I finished. However, their care and love are still with me. Thanks to my mum and dad for your understanding and support, to my sister

and brother for their encouragement. Pippa, I'd like to specially thank you for cooking for me. Your nice meals cheered me up, also thanks for making me laugh when I was down. ☺. It is also worthwhile to mention Maria and Stephen, Bill and Li, David Blenkinson, Kate Pearce etc. They have been very kind and helpful one way or another.

X. Su

May, 2009

List of Figures

List of Tables

Table of Contents

Nomenclature

l	Beam length from the top of the base-clamp to the point where the beam enters the end mass
l_0	Length from the top of the base-clamp to the centre of mass of the end mass
m_0	Mass of the end mass
m	Beam mass per unit length
$u(z,t)\,, v(z,t)\,, \phi(z,t)$	General displacement functions
$f_1(z)\,,\ f_2(z)\,, g_1(z)$	Mode shapes of undamped free vibrations
$u_1(t)\,, u_2(t)\,, \phi_1(t)$	Modal co-ordinates
$\omega_1, \omega_2\,, \omega_t$	Natural frequencies of undamped free vibrations
$\zeta_1, \zeta_2\,, \zeta_t$	Damping ratios
$B_1\,, B_2$	Integration constants
$\bar{p}^2$	Cross-coupling term
W_B	Support excitational displacement
E	Young's modulus
I_Y	Moment of inertia of beam about y-axis
EI_Y	Flexural rigidity about y-axis
I_G	Moment of inertia of the end mass
G	Shear Modulus
J	Polar moment of inertia, for a round shaft or concentric tube only
GJ	Torsional rigidity
c	Constant to account for the beam's non-circular cross-section
$\varepsilon\sigma\ \varepsilon\alpha\ \varepsilon\delta$	Detuning parameters
F_a	Recovery force generated in the SMA strips when they are activated
$F_{u1}\ F_{u2}\ F_{\phi 1}$	Generalised forces

Chapter 1

Introduction

1.1 Motivation of the Research

The vibration problem of a simple cantilever beam carrying a concentrated mass is of great interest to the practical engineers (Magrab, 1979). For example, the system may be considered as a model of a robot arm with a mass in its end effector. Such a structure under parametric vibration has been studied by many researchers and there are several reasonably accurate mathematical models available to the analyst for understanding and prediction of its mechanical vibratory response characteristics. One of these models was developed by Cartmell (1990) and further modified by Forehand and Cartmell (2001). By deriving the necessary kinematic relationships for combined bending and torsional motions for a flexible vertical beam with a lumped end mass, and with the beam undergoing an excitation in the least flexible plane of the structure, these papers discussed the accurate modelling of such a simple structure in the context of a nonlinear, multi-dimensional problem. Therefore, utilising this theoretical model, or a modified one for a similar system but under a different parametric excitation direction, helps in understanding this model more and expanding its usage. In addition, as extensive use of composite materials is made in aeroplanes, satellites, and the transportation industry, and as a wide application of shape memory alloys is potentially extant, due to their unusual characteristics, the enhanced control of vibrational responses of composite structures under parametric excitation, and in particular with the help of integrated shape memory alloy elements can be exploited.

In this research, which starts by modifying the model of Cartmell (1990) and Forehand and Cartmell (2001), three nonlinear equations of motion are derived to predict the parametric resonances, for a flexible steel beam system under a parametric excitation. On the basis of this study, a glass epoxy (g-e) beam structure with two centrally-bonded shape memory alloy (SMA) strips under parametric vibration is studied, both analytically and experimentally, to provide an understanding of the SMA's effect on the dynamic properties of the beam. Furthermore this research provides a concept for a diagonal configuration of

integrated SMA elements on beam structures for future study with a view to specialised mode control.

1.2 Research Objectives

This research proposes a new analytical model for the parametric vibration study of composite beam structures with centrally-bonded SMA elements. As a precursor to this investigation, based on the model by Forehand and Cartmell (2001), three nonlinear equations of motion, for a flexible steel beam with a lumped end mass under a parametric excitation have been derived by recourse to the Lagrangian formulation. The equations are solved by the multiple scales method and then the result is to predict different parametric resonances. The nonlinearity in this problem is considered. Furthermore, two SMA strips are centrally bonded to a g-e beam with a lumped end mass, in a similar configuration to the steel structure. The utilisation of two different techniques on the bonded SMA strips, generally known in the literature as the Active Property Tuning (APT) and Active Strain Energy Tuning (ASET) methods, are both investigated to explore the influence of the strips on the dynamical properties of such a composite material beam structure. In the APT method, changes in the stiffness of the SMA strips during their activation, which accordingly affect the property of the whole structure, are studied. The results are verified via experimental investigations followed by discussions. In the ASET technique, the high recovery force generated when the SMA strips are activated is modelled as compressive force acting on the g-e beam. In order to utilize the Lagrangian formulation once again, the emphasis is focused on the derivation of the generalised forces corresponding to three generalised coordinates, and these are defined in terms of the actual SMA recovery forces. The three equations of motions involving the three generalised coordinates and their corresponding generalised forces are consequently derived. By solving the free vibration equation of the g-e beam-lumped end mass structure subjected to a compressive force, the influence of the SMA strips on the natural frequencies and the mode shapes is investigated. How the SMA strips modify the instability regions of the structure under parametric excitation is studied by solving the three governing equations of motion. In addition, this research also presents a study of the beam structure in which the two SMA strips are diagonally bonded to the beam instead of centrally. The centrally-bonded and diagonally-

bonded cases are compared and the results suggest that the diagonally-bonded configuration can play a role in controlling the torsion modes of the beam structure.

1.3 Organization of the Thesis

This thesis consists of eight main chapters. After this introduction, Chapter 2 presents a broad literature review related to the current work. Chapter 3 includes the analysis of the parametric vibration of a flexible steel cantilever beam of rectangular uniform cross-section with a lumped end mass under a single frequency harmonic excitation in the vertical direction. This chapter begins with the derivation of the equations of motion on the basis of Forehand and Cartmell (2001) model. Following this, an application of the multiple scales method is used to solve the equations. The different parametric resonances and their corresponding instability regions resulting from the solutions of the governing equations and experimental work are also explained in this chapter. An experimental study of the properties of two g-e beams, such as Young's modulus and shear modulus, are discussed in Chapter 4. Investigations into the effect of SMA strips on the natural frequencies and the mode shapes of a g-e beam-lumped end mass structure are explored in Chapter 5 when both APT and ASET methods are implemented. Chapter 6 summarises the formulation of generalised forces induced in a g-e beam-lumped end mass structure under parametric vibration with two centrally-bonded SMA strips when the ASET technique is used. The coordination transformation of the recovery force vector, and the virtual work done by the force are handled in this chapter. Experimental investigation into the influence of SMA strips on the dynamic properties of two g-e beam systems are introduced in Chapter 7. One system is with two centrally-bonded strips whilst the other is with two diagonally-bonded strips. The thesis is concluded by the discussion of future work in Chapter 8.

Chapter 2

Literature Review

2.1 Parametric Vibration in Elastic Systems

All mechanical engineering systems which undergo oscillatory motion are often described by a finite set of governing differential equations. If for some reason one or more parameters, such as the mass, damping, stiffness, appear as time varying coefficients in these equations, the system may be said to be subjected to parametric excitation, and this phenomenon is then called parametric vibration (Ibrahim 1978, Nayfeh and Mook 1979, Cartmell 1990). This is one aspect that parametric vibration differs from the familiar forced vibration, whose coefficients in the equations are all constant. The other difference between these two vibrations is that parametric vibration might occur in directions normal to the excitation, while forced vibration is understood to appear only in directions parallel to the excitation. Faraday (1831) was believed to be the first to observe parametric resonance on the free surface of a liquid. In his experiment, he noticed that the oscillation frequency of the surface waves in a fluid-filled cylinder under vertical excitation oscillates was twice the frequency of excitation itself. In the late 19^{th} century, Rayleigh made his own series of experiments and confirmed Faraday's observation. Melde (1859) performed an experiment on the vibrations of a string of which one end was fixed and the other attached to one prong of a tuning fork. He found that although the excitation was longitudinal, the string could be tuned to oscillate laterally at half the frequency of the fork. Not until 1954 were the findings made by Faraday and Rayleigh, from their experimental work, explained in mathematical terms. Benjamin and Ursell's (1954) study yielded a system of Mathieu equations, for which there were zones of linear instability defined by the amplitude and frequency of the vertical excitation. Beliaev (1924) analyzed a column pinned at both ends undergoing an axial periodic load. He reduced the governing differential equation to the Hill-Mathieu form and his results showed the principal parametric resonance of the column, that is, the column could be made to laterally vibrate with the half frequency of the excitation, even though the axial load may be smaller than the static buckling critical force. Beliaev's work has been extended. Later investigations incorporated such factors as different elastic members, such

as beams, rods, bars, etc; and various boundary conditions, inertia parameters, and different forms of excitations. Dugundji and Mukhopadhyay (1973) carried out a study on a horizontally-orientated cantilever beam subjected to vertical harmonic excitation of its base. The equations of motion were reduced to Mathieu equations. This caused combination resonance, with primary instability regions defined when exciting such that $\omega_F = \Omega_1 + \Omega_3$ and $\omega_F = \Omega_2 + \Omega_3$ (ω_F is the excitation frequency. Ω_1, Ω_2 and Ω_3 are natural frequencies of the first bending, the second bending and the torsional modes of the beam, respectively), with the two modes oscillated simultaneously, each at its own frequency Ω_1, Ω_2 and Ω_3. This showed that lateral bending and twist could be excited by vertical base motion. Cartmell and Robert (1987) theoretically and experimentally investigated the response of a vertically-orientated cantilever beam with an attached end mass system subjected to a parametric excitation. They also found that the parametric excitation promoted a sum-type combination resonance involving two modes of vibration. Analytical studies of the parametrically-excited pendulum can be traced back to the work of Leven and Koch (1981). They identified that the pendulum behaved in a chaotic way under certain parameter intervals. Miles (1985) analyzed the response of a double pendulum system under a parametric excitation through the vertical translation of the pivot of the slower pendulum. In his work, the ratio of the natural frequencies of the two normal modes approximated 2. His results showed that when the lower mode was excited by a principal parametric resonance, the resulting motion may be either a simple (rigid-body) translation of the entire system or coupled oscillations of the pendulums superimposed on such a translation. Watt and Cartmell (1994) designed a single-degree-of-freedom parametric oscillator, onto which was mounted a simple mechanical power take-off device, so that the axial input motion could be converted to a paremetric resonance in the torsional system to transfer energy to an external load, hereby acting potentially as a mechanical power transmission. Cartmell and Roberts (1988) presented a study of a L-shape beam structure. The structure comprised a horizontal beam and a smaller vertical beam. The horizontal beam was clamped at one end and the free end was coupled to the vertical beam. Two combination resonances, involving the fundamental and second bending modes and the fundamental torsion mode of the structure, could be generated when the external excitation of the support was at a frequency in the region of the second bending mode

frequency of the system when it oscillated in the least stiff plane. In his experiment, Mullin (1993) linked three rods, one being attached to a pivot, represented as Fig 2-1, and demonstrated that the triple rods could be stabilized by vertical vibrations of their pivot, even though the rods were longer than their critical lengths. As an extension of this work, Champneys and Fraser (2000) proposed a theory for this phenomenon. They derived a formula, which could predict a bound on the frequency and amplitude of excitation with the purpose for the unstable column to be stabilized by harmonic excitation. Experimental investigation has been carefully carried out by Cicek and Ertas (2002) on a beam-tip mass and pendulum system under random excitation, shown in Fig 2-2. In this research, the system consisted of a flexible beam, one end fixed and the free end coupled with a lumped tip mass, and a mass-pendulum was attached to the tip mass. They noted from their experiments that when the ratio of the first natural frequency of the pendulum to that of the beam was tuned to 0.5, the beam's mean-square response decreased, and the pendulum response increased, indicating an energy exchange between the two elements due to the autoparametric interaction between the modes of the system.

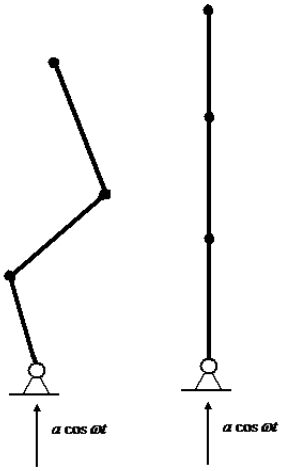

Fig 2-1 An inverted triple pendulum (Mullin 1992)

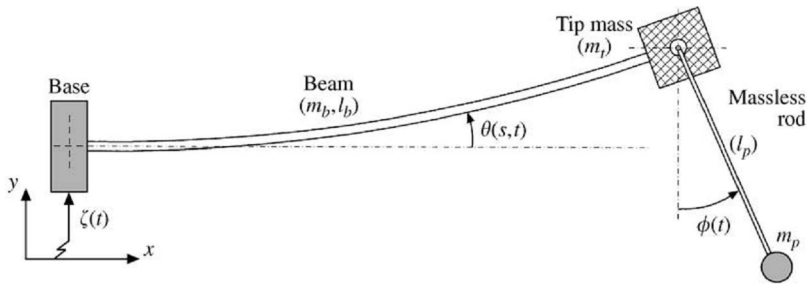

Fig 2-2 Beam-tip mass-pendulum system under random excitation (Cicek and Ertas 2002)

2.2 Nonlinear Problems in Parametric Vibration

Although the mechanics of vibrating systems subjected to parametric excitation are often described mathematically by a set of linear differential equations, this is, in general, the least precise model in the sense that such a formalisation can always be refined by the introduction of nonlinearity, so that the precision of its predictions is increased and its range

of application is extended. Furthermore, the nonlinear model may introduce the means of explaining or predicting behavioural phenomena which are outside the limits of the linear theory. Nonlinearities may enter a model in many ways. Their origin may be geometrical, or material, or they may be associated with nonlinear forces or the physical configuration. Any component of the equations of motion may be nonlinearly affected: the inertia terms, the stiffness terms, the damping terms, terms describing external excitation, and the boundary conditions. Nonlinearities can be important – especially with resonance conditions that differ from those obtained from linear theory. There is a great deal of literature that has been published on the study of the effects of various nonlinearities on the behaviour of parametrically excited systems. The studies showed that nonlinearities could modify the instability regions and limited the peak amplitude response; that they could change an originally stable system to a catastrophic unstable state; and they could cause different types of resonance, i.e. subharmonic, superharmonic or combination resonances, for example. In addition to those resonances already mentioned, the internal resonance is said to exist in multi-degree-of-freedom systems. It is because nonlinearities may provide such a mechanism that energy imparted into one mode may under certain conditions be exchanged with other modes. This is called nonlinear mode-coupling. Modal interaction can be especially pronounced when two or more of the linear natural frequencies are related by integers or near-integers. Depending on the order of the nonlinearity such frequency relationships can cause the corresponding modes to be strongly coupled, and result in internal resonances.

2.3 Solution Methodologies

There are three commonly applied analytical methods for approximately solving nonlinear systems: **the method of multiple scales**, **the method of harmonic balance and the method of averaging.** The multiple scales method was discussed in a few well-known books (Nayfeh 1973, Nayfeh and Mook 1979, Cartmell 1990, Thomsen 1997). It has been shown to be immensely useful for a wide range of nonlinear vibration problems. With this method, one generally assumes that the dependent variable(s) is (are) uniformly expanded in terms of two or more independent variables as $u(t,\varepsilon)=\sum_{j=0}^{m-1}\varepsilon^{j}u_{j}(T_0,T_1,\ldots T_m)+o(\varepsilon T_m)$, $j=0,1,2\ldots$. Here

the dependent variable $u(t,\varepsilon)$ is a function of the multiple independent time variables T_j, and these are referred to as scales. The variables T_j are generated with respect to real time t as $T_j = \varepsilon^j t$. Accordingly the time derivatives of the dependent variable(s) are expressed as follows, starting with the first time derivative T_0 : $d/dt = D_0 + \varepsilon D_1 + \cdots, d^2/dt^2 = D_0^2 + 2\varepsilon D_0 D_1 + \cdots,$ where $D_j = \partial / \partial T_j$. Upon substituting the expansion and its derivatives with respect to time into the original equations of motions and equating to zero the coefficients of like powers of ε yields a series of perturbation equations. By solving these equations and eliminating the secular terms that cause unbounded perturbations gives the solution of the assumed form. With the method of harmonic balance, one assumes a periodic solution in the form of a harmonic series $x(t) = \sum_0^N A_j \cos(j\omega t + j\phi_0)$. The series is then substituted into the equations of motion, and manipulating the results to group coefficients of like frequency. Each harmonic is then balanced by requiring that like-frequency coefficients on each side of the equations satisfy equality individually. Usually all unknown constants are expressed in terms of A_j and ϕ_0, which are determined by the initial conditions. The application of this method can be found in literatures like Cheung *et al* (1990), Zhang and Huseyin (2001), Maple (2002) and Cai *et al* (2006). The method of averaging requires that the differential equations of the system be written in the standard form, in which the right hand side is regarded as a slight perturbation proportional to a small parameter ε. With this method, the first step is to obtain the solution to the reduced linear equation by setting $\varepsilon = 0$ in the original equation of motion. One then assumes that the nonlinear solution is similar to the linear solution with different time variations in amplitude a and phase ϕ. In systems with weakly nonlinear behaviour the nonlinear terms will not be strongly contributory to the particular characteristic, such as resonance conditions etc, it is implied that the changes in a and ϕ are very slow. According to Krylov and Bogoliubov, by replacing the equations for $\dot{a}$ and $\dot{\phi}$ with their average values during one period of oscillation, a and ϕ can be determined through the integration of $\dot{a}$ and $\dot{\phi}$ in one period. Bondarev (1970) used this method to solve the differential equations of nonlinear vibration of a rectangular plate. In the study of the motion of a straight bar with hinged supports and excited by a harmonic axial

displacement, the method of averaging was applied by Anderson (1975) to solve the non-linear differential equations. The application of this method can also be found in the papers such as Hamdan (1990), Coppola (1997) and Basu *et al* (2007).

Out of the above three methods, the method of multiple scales and the method of averaging are generally accepted as perturbation methods, that is, they work by applying small nonlinear perturbations to linearized solutions. Their application is restricted to weakly nonlinear systems, so the nonlinear terms should be small compared to linear terms. During their analysis of the perturbation method of multiple scales applied to the dynamics of weakly nonlinear mechanical systems, Cartmell *et al* (2003) presented a short discussion on methodologies for ordering of nonlinear terms, and specifically the treatment of the "small" perturbation and ordering parameter ε. According to their research, one way to deal with ordering is to base it on physical meaning, leading to notions of "hard" or "soft" excitation, and "strong" or "weak" damping. "Hard" excitation and "strong" damping term might be expressed to zeroth order ε, and "soft" excitation and "weak" damping term to first or second order ε. In this case ε can be seen as a convenient universal scaling parameter for different, apparently unrelated, quantities within the equation of motion, such as damping, excitation amplitude, and coefficients of nonlinear terms. The other way for introducing ε is based on formal nondimensionalization of the dependent and independent variables, time for instance. In this case ε is introduced as a nondimensionalizing parameter into equation of motion so that a dimensionless variable replaces the original dependant variable in the equation. Several publications in the literature show that by using this method plus some other ordering scheme required by the physical problem, the inertial nonlinearities are automatically set to higher order ε (Watt and Cartmell 1994, example 2.3.1 in Murdock 1991). It is noted that ordering schemes described above under some situations are not always analytically derivable for all terms in the governing equations, and can be physically unacceptable. So it is important to proceed with caution though such an approach can possibly achieve accurate and meaningful results.

2.4 Application of Shape Memory Alloy Elements on Elastic Structures

2.4.1 Background

Composite materials have gained popular usage due to their wide applicability and economic benefit. They have excellent engineering properties such as light weight, corrosion resistance, high strength, stiffness, and control characteristics. Therefore, their uses are increasing broadly with application to structures in relevant fields such as the space and aviation industries, the transportation industry, sporting goods, medical instrument parts, and mechanical parts. Glass fibre reinforced composites can be very reliable engineering materials compared with other composites by virtue of a large technology base and experience in service (Mallick 1993). Epoxy resin as the matrix is widely used in the production of glass fibre composites due to its wetting power and adhesion to glass fibre, low setting shrinkage, considerable cohesion strength, adequate dielectric characteristics, and thermal properties. Because of the extensive use of composite materials, the guarantee of high durability and long-term performance of structural elements made of it is a very important issue. One of many methods used to achieve this objective could be the integration of composite materials with another class of high performance materials, such as shape memory alloys (SMAs). SMAs gained popularity since the shape memory effect was discovered in 1932, especially when the NiTinol alloy was developed in 1962. NiTinol is a commonly used shape memory alloy that contains a nearly equal mixture of nickel (55 wt.%) and titanium. NiTinol shows basically two significant effects: one is the spectacular thermal shape memory effect, its ability to “memorize” its original shape after deformed by heating the SMA above the characteristic transition temperatures. This phenomenon is caused by a phase transformation of the SMA microstructure from martensite to austenite when the transition temperature is reached. The transformation takes place at four characteristic temperatures known as M_f (martensite finish), M_s (martensite start), A_f (austenite finish) and A_s (austenite start). A typical relation between temperature and martensite phase concentration is shown in Fig 2.1 (Liang 1990). Due to this effect, the material can recover as much as 8% strains. Large force is generated when the material is returning to its original shape. It is called the recovery force in this thesis. NiTinol can also show an amazing amount of pure elastic deformability (superelasticity). This happens when the material is at its full austenite phase. It transforms into martensite phase when a load is applied, and recover its original shape when the load is removed by means of a hysteresis loop. The process is shown in Fig 2-2. Unlike the shape memory effect, superelasticity occurs without a

temperature change. Due to these two unique charateristics, SMA components offer great capabilities for active control of the static and dynamic behaviour of overall integrated structures.

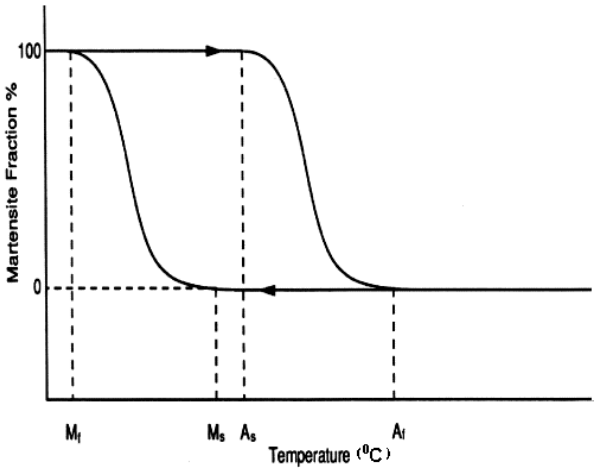

Fig 2-3 The phase transformation with temperature (Liang, 1990)

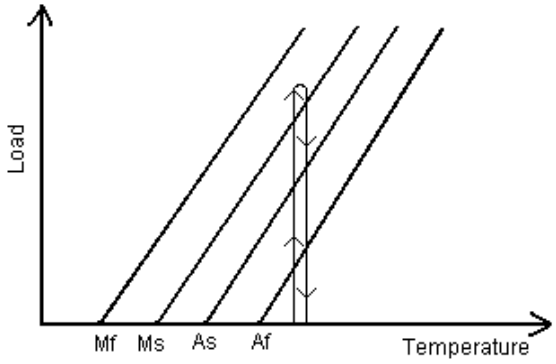

Fig 2-4 Load diagram of the superelaticity effect (University of Alberta smart material and micromachines website, 2001)

2.4.2 Embedded SMA Elements in Elastic Composite Structures

Rogers *et al* (1989) embedded SMA wires into composite plates by utilizing the phase transformation as a means to alter the static deflection and modal characteristics of these plates. With the same model, Rogers *et al* also presented the concepts of using SMA wires to control the natural frequencies and modes of vibrations of simply-supported plates. Zak *et al* (2003) investigated the changes in the fundamental natural frequency of a multi-layered composite plate with embedded SMA wires. They found that the natural freqency largely depended on the plate geometry and the form of boundary conditions, but could be successfully controlled by an optimal selection of the geometrical parameters and material properties. Lagoudas and Tadjbakhsh (1993) formulated a flexible rod with embedded line SMA actuators in three dimensions, and studied the deformed shapes of the rod under repeated thermal actuation and the resulting shape memory loss due to the development of residual stresses. Baz *et al* (1995) showed that internally fitted SMA wires could successfully be used to control the natural frequencies of clamped-clamped composite beams. Furthermore, Baz *et al* (2000) also investigated the use of embedded SMA components in the form of strips for shape control of composite beams as well as the natural frequencies of such structures. Icardi (2001) studied, both numerically and experimentally, the bending

deflection of a laminated solid cross-ply cantilever beam with embedded pre-stressed and pre-strained SMA. His study presents a preliminary understanding of the shape control of stiff laminated composite structural members. Zhang *et al* (2006) presented two types of SMA-embedded cantilever composites to investigate the influence of both the SMA arrangement and the temperature on the vibration characteristics of the system. One laminated plate contained unidirectional fine SMA wires; another one was with an embedded woven SMA layer. Their results showed that at high temperatures, the natural frequencies in both the beams were increased significantly. Both SMA orientations could effectively control the systems' damping as well. Thompson and Loughlan (1997) employed embedded SMA wires to enhance the post-buckling behaviour of laminated plate structures while under a uniaxial load. Their study showed that the activation of constrained pre-strained SMA wire actuators, located on a laminated plate's neutral plane, resulted in significant post-buckled deflection alleviation, even at load levels approximately three times the critical buckling value. Lee and Lee (2000) investigated the buckling and post-buckling behaviour of simply-supported and clamped composite plates with internally fitted SMA wires. They found that the activation of SMA wires could increase the critical load capacity of these composite plates. Lau (2002) studied the natural frequencies and damping ratios of a composite beam with embedded SMA wires. He found, with clamped-clamped boundary conditions, the actuation force of the pre-strained SMA wires increased the natural frequencies of the beam. It was because when the beam was fixed at both ends, the recovery force would generate a tensile force in the beam. The impact damage behaviour of carbon fibre/epoxy composite plates embedded with superelastic shape memory alloy wires was investigated by Meo *et al* (2005). They found that the ability of SMA wires to absorb kinetic energy during the impact due to their superelastic and hysteretic behaviour could increase the damage resistance of composite structures. Kang and Kim (2009) compared two kinds of glass/epoxy composites with and without SMA wires inserted in the neutral plane of the laminates, to identify the effect of SMA on their damage behaviour and residual strength subjected to low-velocity impact at low temperatures. In all these investigations the SMA components have been embedded in the host material, and the basic mechanism by which these SMA components affect the structure is either by producing in-plane forces or by changing its stiffness. However there are difficulties of using embedded pre-strained

SMA components with composite structures (Ni *et al,* 2007). For example, the large recovery stress of SMAs can pull SMA fibres out of the matrix; the interfacial failure between the SMAs and the matrix can occur because the fabrication process results in high residual stress within the SMA composites when cooled to room temperature; the complexity of the applications of the composite structures combined with the intricate nonlinear behaviour of the SMA itself makes analysis and design difficult .

2.4.3 Externally-attached SMA Elements in Elastic Structures

There are a good many reported instances in the literature of using externally-attached SMA actuators, consequent to two features: (1) better control authority as the SMA can be placed at different offset distances from the host; (2) much greater moment, generated by the actuation force from the SMAs in comparison to that in a composite structure with embedded SMAs with the same magnitude of actuation force. Baz *et al* (1990) designed an active controller by utilizing Nitinol actuators to suppress the vibrations of a flexible beam. In their work, the SMA wires were placed external to the beam and the controller was shown to work reasonably well on the first bending mode of the beam and could easily extend this to multi-modal vibration. Chaudhry and Rogers (1991) presented two configurations with external SMA wires fitted to a cantilever beam. One configuration was with a SMA wire attached only to two points, the fixed and free end of the beam; the other was that the wire passed through a few selective points on the beam. They demonstrated the possibility of using the configurations to induce deflections of the beam and thus the feasibility of using the configurations for bending shape control. In their paper (1997), Shu *et al* introduced a similar model to demonstrate shape control by an SMA wire on a cantilever beam. The wire was eccentrically mounted at the tip and at the foundation of the beam. Lu *et al* (2001) designed a cantilever actuator, which comprises a triangular corrugated core with SMA sheets as the two faces. Their work showed that the actuator could be made to operate against large restraining moments by using the constrained force caused by the SMA sheets due to phase transformation. Baz *et al* (1995) used embedded SMA wires to control the natural frequencies of a composite beam. The wires were embedded inside vulcanized rubber sleeves and placed along the neutral axis of the composite beam and could move freely during the activation. By utilizing the shape memory effect, the activated

SMA wires could increase or decrease the natural frequencies of the beam under certain conditions. Kim and Cho's actuator (2007) consisted of two SMA wires attached to the tip of a bar symmetrically on both sides. Distinct from the more commonly used shape memory effect, Gandhi and Chapuis (2002) examined the effectiveness of pseudoelastic SMA wires on the damping of flexural vibrations of a cantilever beam with a tip mass. Two SMA wires were symmetrically mounted to one end of the tip mass and there were angles between the wires and the beam. The beam was subjected to a harmonic excitation force near the tip. Their results show that the damping introduced by the SMA wires would increase for higher excitation-force amplitudes. The damping was also a function of the SMA wire cross-section area, wire length, and the angle between the wire and the beam, but independent of the tip mass.

However, no investigations of the effect of SMA on the instability regions of a composite beam structure under parametric vibration have been studied when the SMA elements are externally bonded.

2.5 Theoretical Investigations for Composite Beams with Integrated SMA Elements

For the past decade, a substantial amount of theoretical and experimental research has been performed on the modelling of composite structures with integrated SMA elements. The first step of modelling is normally to determine the characteristics of the SMA components that underlie the classical shape memory effect and superelasticity. The characteristics can be determined by experimental measurements or from constitutive models. A large amount of papers on SMA models have been published. There are quite a few classical models in the literature, proposed and developed by Tanaka (1986), Liang and Rogers (1990) and Brinson (1993), Lagoudas *et al* (1994a,b) and Cartmell *et al* (2000), which are widely used by researchers in their SMA integrated composite beams. These models are also often used in conjunction with experiments. The second step of the modelling is to investigate the interaction between the SMA elements and the matrix by using either numerical or analytical methods, or both. In their studies of a cantilever beam with two SMA layers to control its natural frequencies, Chan and Levy (1996) applied the model developed by Tanaka to obtain the Young's modulus and the recovery stresses of the two SMA layers.

Then the force balance condition in the individual layers and the beam, and their force interaction, was analyzed and the governing equation of the beam was derived from Euler theory. Finally, the expression for the natural frequencies of the beam, as a function of the Young's modulus and recovery stresses of the SMA layers, was obtained. Epps and Chandra (1997) employed the model developed by Liang and Rogers to study the active frequency tuning of a composite beam. Analytically, a composite beam with embedded sleeves containing SMA wires was modelled as a beam on an elastic foundation which was dependent upon the recovery force developed in the SMA wires. Using this model, a free vibration analysis of the beam was carried out to examine the natural frequencies. Baz *et al* (1990) used the finite element method to model their beam dynamics with two external SMA wires. The thermal and dynamic characteristics of the SMA wires were integrated into the stiffness matrix, mass matrix and force vector. Shu *et al* (1997) did a nonlinear geometrical static analysis first to investigate the deformed shape of a flexible beam caused by an externally-attached SMA wire at its activation. They then used Lagoudas' thermodynamic constitutive model for SMAs to obtain the actuation force, and finally both the beam and the SMA actuator were connected through an iterative scheme to translate an input electrical current history into the beam strain output. Their experimental results agreed well with the model simulation. The finite element method was used by Baz *et al* (1995) as well. In their element equations of motion, the element stiffness comprised three parts: the flexural rigidity of the beam element itself, the geometric stiffness that accounted for the axial and thermal loading from the SMA wires, and the elasticity of the SMA wires. Bernoulli-Euler theory was used to model the composite beam.

2.6 Objectives

- A study on a flexible steel beam structure under a different parametric excitation is to be carried out, the multiple scales method is to be used to solve the equations of motion, in order to investigate the parametric resonances and the effect of nonlinearity on their corresponding instability regions. Experimental work will be carried out to verify the theoretical results.

- A composite beam structure with two centrally-bonded SMA strips under parametric vibration is to be analyzed and tested, with the purpose of achieving enhanced dynamic control.
- A composite beam structure with two diagonal-configuration SMA strips will be discussed and tested, intending to tune specialised modes of the structure and provide a preliminary reference for future work.

Chapter 3

A Steel Cantilever With an End Mass Under Parametric Vibration

3.1 Introduction

A cantilever beam under parametric vibrations has been considered by many researchers. Dugundji and Mukhopadhyay (1973) studied a thin, plate-like, cantilever beam, well below static lateral buckling under gravity and subjected to lateral harmonic excitation of its base in the stiff direction, and found that primary combination resonances, involving two degrees of freedom, were shown to occur near forcing frequencies, with each mode oscillating at its own natural frequency. Cartmell and Roberts (1987) used the method of multiple scales to investigate the same instability regions of a cantilever beam carrying an end mass excited in the plane of the largest rigidity, i.e. y-axis direction in Figure 3-1, and also extended the system to a third degree of freedom to generate another type of combination resonance by working to second order perturbation. Their work was extended by Ibrahim and Hijawi (1998) to examine the influence of random parametric excitation on such a cantilever-end mass system response. In his paper published in 1990, Cartmell unified the necessary kinematics and dynamics for the system. He derived the necessary kinematic relationships for combined bending and torsional motions of the beam and from these derived three non-linear modal equations of motion by using Lagrange's formulation in conjunction with the kinetic and potential energy functions. Forehand and Cartmell (2001) added further justifications to the model by Cartmell (1990), whilst also showing that there is a cross-coupling term in the expression for the potential energy as a result of a two-mode Galerkin representation. In this chapter, the author investigates the excitation in the z-axis direction, shown in Figure 3-1, rather than excitation in the y-axis direction for the beam system. Three nonlinear equations of motion, representing the first and second bending modes and the first torsion modes are derived. A multiple scales analysis is followed to solve the equations of motion. A linear cross coupling term, which originally appears in the expression for the potential energy, and which propagates through to the lowest order perturbation equations, has been shown to be numerically negligible despite necessarily being ordered to $o(\varepsilon)$ in the perturbation analysis. Then, the consequences of the multiple scales analysis up

to the first order for three different combination resonances are explored, on the basis of this numerically justified simplification. Laboratory tests confirm that these instabilities are bounded in practice by nonlinear effects. In order to generate further combination resonances, a second order multiple scales expansion is investiaged. A considerable number of intermediate calculations are performed because of the higher order of expansion and a full list of resonances from second-order perturbation equations are obtained.

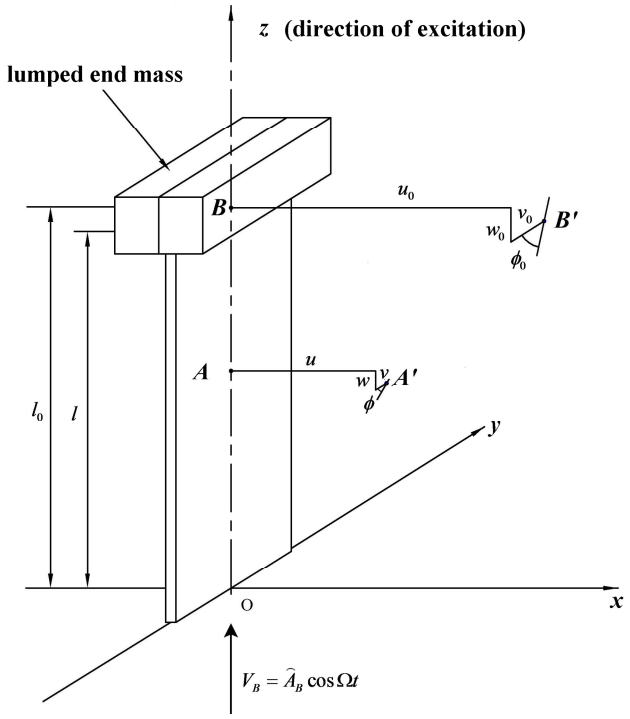

Fig 3-1 Physical representation of the steel system (adapted figure from Forehand and Cartmell (2001))

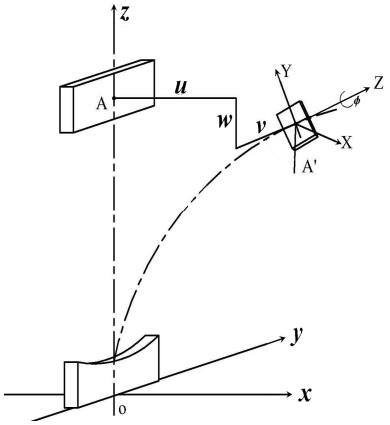

Fig 3-2 An element of the beam in both its undeformed and deformed states

3.2 Formulation of the Governing Equations

In order to make the arbitrary lateral displacement coordinate $u(z,t)$ and rotation coordinate $\phi(z,t)$ separable in time and space, the Galerkin type representation involving functions of linear modes is required, such that

$$u(z,t) = f_1(z)u_1(t) + f_2(z)u_2(t) \tag{1}$$

$$\phi(z,t) = g_1(z)\phi_1(t) \tag{2}$$

Thus three modes of vibration are to be considered, where $f_1(z)$, $f_2(z)$ and $g_1(z)$ are linear mode shape functions relating to the fundamental and second bending modes and the fundamental torsion mode respectively. These functions are readily derived by means of Euler-Bernoulli beam theory (see **Appendix 1**). $u_1(t)$, $u_2(t)$ and $\phi_1(t)$ are the corresponding modal co-ordinates of the three modes of interest.

3.2.1 Expression for the Kinetic Energy

As shown in Figure 3-1, point A is an arbitary location along the beam, whist point B is the centre of the end mass. When the beam system is subjected to combined bending and torsion, point A will move to a new position, denoted as A' and point B to B'. The movement can be considered in terms of displacements u, v, w and a twist angle ϕ. It can be seen from Figure 3-1 that u represents lateral displacement in the Oxz plane, whereas v defines motion in the Oyz plane and w is the vertical motion. The twist angle ϕ defines the rotation about the deformed Z-axis shown in Fig 3-2. The displacements and twist angle of point B, i.e. the centre of the end mass, are denoted with 0-subscripture. The total system kinetic energy comprises the kinetic energy of the beam due to its bending in the x direction and the kinetic energy of the end mass due to velocity $\dot{w}_0$ in the z-axis direction and $\dot{v}_0$ in the y-axis direction, and the rotational kinetic energy of the end mass about the Z-axis. Forehand and Cartmell (2001) have derived the equation of the kinetic energy as

$$T = \frac{1}{2} m_0 (\dot{u}_1^2 + \dot{u}_2^2 + (\dot{W}_B - \dot{w}_0)^2 + \dot{v}_0^2) + \frac{1}{2} I_0 \dot{\phi}_0^2 \qquad (3)$$

where m_0 denotes the end mass, u_1 and u_2 the modal displacement co-ordinates in bending, W_B the support excitation displacement, and I_0 the moment of inertia of the end mass about the deformed z-axis.

3.2.2 Expression for the Potential Energy

The total potential energy involves the strain energies due to bending and torsion, respectively and the gravitational potential energy of the end mass. It is given by

$$U = \int_0^l \frac{1}{2} EI_y (u'')^2 dz + \int_0^l \frac{1}{2} cGJ(\phi')^2 dz - m_0 g w_0 \tag{4}$$

The above equation can be expressed in the form of equation (7), after the displacements w_0 and v_0 are expressed in terms of the modal co-ordinates u_1 and u_2 using equations (39) and (41) from the paper by Forehand and Cartmell (2001). For convenience, equations (39) and (41) are re-written and re-numbered as here:

$$v_0(t) = B_1\phi_1 u_1 + B_2\phi_1 u_2 \tag{5}$$

$$w_0(t) = \frac{1}{2}\left(\int_0^l (f_1')^2 dz\right)u_1^2 + \left(\int_0^l (f_1' f_2' dz)u_1 u_2 + \frac{1}{2}\left(\int_0^l (f_2')^2 dz\right)u_2^2\right. \tag{6}$$

$$\begin{aligned} U = {} & \frac{1}{2}[EI_y \int_0^l (f_1'')^2 dz - m_0 g \int_0^l (f_1')^2 dz]u_1^2 + \frac{1}{2}[EI_y \int_0^l (f_2'')^2 dz - m_0 g \int_0^l (f_2')^2 dz]u_2^2 \\ & + [EI_y \int_0^l (f_1'' f_2'')dz - m_0 g \int_0^l (f_1' f_2')^2 dz]u_1 u_2 + \frac{1}{2} cGJ[\int_0^l (g_1')^2 dz]\phi_1^2 + m_0 g W_B \end{aligned} \tag{7}$$

where GJ is the torsional rigidity of the beam about the $z-axis$, assumed to be constant. Quantity c is the constant introduced into the stardard torsion equation (Timoshenko 1878) to deal with non-circular cross-section. It has been shown here that the modal co-ordinates u_1 and u_2 couple in the expression of the potential energy.

3.2.3 Equations of Motion

Applying Lagrange's equations in the form

$$\frac{d}{dt}\frac{\partial T}{\partial \dot{q}_i} - \frac{\partial T}{\partial q_i} + \frac{\partial U}{\partial q_i} = Q_{q_i} \tag{8}$$

where

$q_1 = u_1$; $q_2 = u_2$; $q_3 = \phi_1$ and the generalised force $Q_{q_i} = 0$ for $i = 1$ to 3.

enables the governing equations of motion to be derived from the energy expressions T and U.

The resulting equations are as follows.

$$\ddot{u}_1[1+B_1^2\phi_1^2+(Xu_1+Yu_2)^2]+2\dot{u}_1\dot{u}_2Y(Xu_1+Yu_2)+\dot{u}_1^2X(Xu_1+Yu_2)$$
$$+\dot{u}_2^2Z(Xu_1+Yu_2)+\ddot{u}_2(Xu_1+Yu_2)(Yu_1+Zu_2)+B_1^2\phi_1\ddot{\phi}_1u_1+2B_1^2\phi_1\dot{\phi}_1\dot{u}_1$$
$$+2B_1B_2\phi_1\dot{\phi}_1\dot{u}_2+B_1B_2\phi_1\ddot{\phi}_1u_2+B_1B_2\phi_1^2\ddot{u}_2+(RN-gX)u_1+(RS-gY)u_2$$
$$+\hat{A}_B\Omega^2\cos(\Omega t)(Xu_1+Yu_2)=0$$

$$\ddot{u}_2[1+B_2^2\phi_1^2+(Yu_1+Zu_2)^2]+2\dot{u}_1\dot{u}_2Y(Yu_1+Zu_2)+\dot{u}_2^2Z(Yu_1+Zu_2)$$
$$+\dot{u}_1^2X(Yu_1+Zu_2)+\ddot{u}_1(Xu_1+Yu_2)(Yu_1+Zu_2)+B_2^2\phi_1\ddot{\phi}_1u_2+2B_2^2\phi_1\dot{\phi}_1\dot{u}_2$$
$$+2B_1B_2\phi_1\dot{\phi}_1\dot{u}_1+B_1B_2\phi_1\ddot{\phi}_1u_1+B_1B_2\phi_1^2\ddot{u}_1+(RS-gY)u_1+(RP-gZ)u_2$$
$$+\hat{A}_B\Omega^2\cos(\Omega t)(Yu_1+Zu_2)=0$$

$$\ddot{\phi}_1[1+V(B_1u_1+B_2u_2)^2]+\dot{\phi}_1[2V(B_1\dot{u}_1+B_2\dot{u}_2)(B_1u_1+B_2u_2)]$$
$$+\phi_1[V(B_1\ddot{u}_1+B_2\ddot{u}_2)(B_1u_1+B_2u_2)]+\phi_1(\frac{cGJQ}{I_0})=0 \qquad \text{(9) to (11)}$$

Here, the geometrical constants are as follows:

$X=\int_0^l(f_1')^2dz$, $N=\int_0^l(f_1'')^2dz$, $Z=\int_0^l(f_2')^2dz$, $P=\int_0^l(f_2'')^2dz$, $Y=\int_0^l(f_1'f_2')dz$,

$S=\int_0^l(f_1''f_2'')dz$, $B_1=\int_0^l(l-z)g_1f_1''dz$, $B_2=\int_0^l(l-z)g_1f_2''dz$, $V=\frac{m_0}{I_0}$, $Q=\int_0^l(g_1')^2dz$,

$R=\frac{EI_y}{m_0}$, $W_B=\hat{A}_B\cos(\Omega t)$, where Ω is the frequency of the excitation.

See **Appendix 1** for definitions of these constants.

In section 3.1-3.2, the prime ' denotes differentiation with respect to z and $\cdot$ denotes differentiation with respect to t.

3.3 Analysis of the Governing Equations

Equations (9) to (11) contain certain linear terms. If equation (9) is taken as an example, these linear terms are the inertia term $\ddot{u}_1$, the stiffness term $(RN-gX)u_1$, rewritten as $\omega_1^2u_1$, the term $(RS-gY)u_2$, rewritten here as $\bar{p}^2u_2$, and the excitation term $\hat{A}_B\Omega^2\cos(\Omega t)(Xu_1+Yu_2)$ .The excitation term is a parametric excitation term as it appears as a time varying modification of the system parameters u_1 and u_2. Likewise, the stiffness

term in equation (10) is rewritten as $\omega_2^2 u_2$ and in equation (11) as $\omega_t^2 \phi_1$. The rest of the terms in equations (9) to (11) are nonlinear cubic terms. These nonlinearities arise because of the use of equations (5) and (6), which describe the geometrical relationship between u_1, u_2 and ϕ_1, v_0, w_0. A classical linear viscous damping term is assumed and inserted of the form $\frac{c_1}{m_0}\dot{u}_1$ into equation (9) (again, here equation (9) is taken as an example), which we re-write as $2\zeta_1\omega_1\dot{u}_1$.

3.4 Treatment of the System Equations

3.4.1 Ordering Scheme

Having identified the non-linearities presented in this structure, we can progress to investigate their effects. The non-linearities can be treated through perturbation methods. To accomplish this, equations (9) to (11) need to be ordered by introducing the perturbation parameter ε in a suitable manner. By assuming a nondimensionalisation scheme, where ε is arbitrary and of length dimension, two new bending coordinates are defined as $\bar{u}_1 = u_1 / \varepsilon$, $\bar{u}_2 = u_2 / \varepsilon$. Similarly for the torsional coordinate ϕ_1, we define the following, $\bar{\phi}_1 = \frac{\phi_1}{\varepsilon}\sqrt{\frac{1}{V}}$, where $V = \frac{m_0}{I_0}$ and the quantity $\sqrt{\frac{1}{V}}$ has the unit of $\sqrt{\frac{ML^2}{M}} = L$. $\bar{u}_1$, $\bar{u}_2$ and $\bar{\phi}_1$ are now all non-dimensionalized coordinates (noting that ϕ_1 in radians is itself dimensionless). The derivatives, obviously, come out as $\ddot{u}_1 = \varepsilon\ddot{\bar{u}}_1$, $\dot{u}_1 = \varepsilon\dot{\bar{u}}_1$ and in the same manner $\ddot{u}_2 = \varepsilon\ddot{\bar{u}}_2$, $\dot{u}_2 = \varepsilon\dot{\bar{u}}_2$, $\ddot{\phi}_1 = \varepsilon\sqrt{V}\ddot{\bar{\phi}}_1$, $\dot{\phi}_1 = \varepsilon\sqrt{V}\dot{\bar{\phi}}_1$. Based on understood physical meaning in context, we consider the damping term and the excitation amplitude to be of magnitude order $\varepsilon << 1$ and, that is $\hat{A}_B \to \varepsilon\hat{A}_B$, $\zeta_1 \to \varepsilon\zeta_1$. The linear term $\bar{p}^2$ is set to $\varepsilon\bar{p}^2$ due to numerical explorations and eventual justification (see **Appendix 2** for the reason and different factors which affect this ordering method). Substituting $\hat{A}_B \to \varepsilon\hat{A}_B$, $\zeta_1 \to \varepsilon\zeta_1$ and $\bar{p}^2 \to \varepsilon\bar{p}^2$ into equations (9) and (10), we obtain, upon cancelling through by ε and tidying up:

$$\ddot{\bar{u}}_1[1+\varepsilon^2 VB_1^2\bar{\phi}_1^2+\varepsilon^2(X\bar{u}_1+Y\bar{u}_2)^2]+2\varepsilon^2\dot{\bar{u}}_1\dot{\bar{u}}_2Y(X\bar{u}_1+Y\bar{u}_2)+\varepsilon^2\dot{\bar{u}}_1^2X(X\bar{u}_1+Y\bar{u}_2)$$
$$+\varepsilon^2\dot{\bar{u}}_2^2Z(X\bar{u}_1+Y\bar{u}_2)+\varepsilon^2\ddot{\bar{u}}_2(X\bar{u}_1+Y\bar{u}_2)(Y\bar{u}_1+Z\bar{u}_2)+\varepsilon^2VB_1^2\bar{\phi}_1\ddot{\bar{\phi}}_1\bar{u}_1+2\varepsilon^2VB_1^2\bar{\phi}_1\dot{\bar{\phi}}_1\dot{\bar{u}}_1$$
$$+2\varepsilon^2VB_1B_2\bar{\phi}_1\dot{\bar{\phi}}_1\dot{\bar{u}}_2+\varepsilon^2VB_1B_2\bar{\phi}_1\ddot{\bar{\phi}}_1\bar{u}_2+\varepsilon^2VB_1B_2\bar{\phi}_1^2\ddot{\bar{u}}_2+\omega_1^2\bar{u}_1+\varepsilon\bar{p}^2\bar{u}_2$$
$$+\varepsilon\hat{A}_B\Omega^2\cos(\Omega t)(X\bar{u}_1+Y\bar{u}_2)+2\varepsilon\zeta_1\omega_1\dot{\bar{u}}_1=0 \qquad (12)$$

$$\ddot{\bar{u}}_2[1+\varepsilon^2 VB_2^2\bar{\phi}_1^2+\varepsilon^2(Y\bar{u}_1+Z\bar{u}_2)^2]+2\varepsilon^2\dot{\bar{u}}_1\dot{\bar{u}}_2Y(Y\bar{u}_1+Z\bar{u}_2)+\varepsilon^2\dot{\bar{u}}_2^2Z(Y\bar{u}_1+Z\bar{u}_2)$$
$$+\varepsilon^2\dot{\bar{u}}_1^2X(Y\bar{u}_1+Z\bar{u}_2)+\varepsilon^2\ddot{\bar{u}}_1(X\bar{u}_1+Y\bar{u}_2)(Y\bar{u}_1+Z\bar{u}_2)+\varepsilon^2VB_2^2\bar{\phi}_1\ddot{\bar{\phi}}_1\bar{u}_2+2\varepsilon^2VB_2^2\bar{\phi}_1\dot{\bar{\phi}}_1\dot{\bar{u}}_2$$
$$+2\varepsilon^2VB_1B_2\bar{\phi}_1\dot{\bar{\phi}}_1\dot{\bar{u}}_1+\varepsilon^2VB_1B_2\bar{\phi}_1\ddot{\bar{\phi}}_1\bar{u}_1+\varepsilon^2VB_1B_2\bar{\phi}_1^2\ddot{\bar{u}}_1+\omega_2^2\bar{u}_2+\varepsilon\bar{p}^2\bar{u}_1$$
$$+\varepsilon\hat{A}_B\Omega^2\cos(\Omega t)(Y\bar{u}_1+Z\bar{u}_2)+2\varepsilon\zeta_2\omega_2\dot{\bar{u}}_2=0 \qquad (13)$$

In a similar manner, substituting the above expressions into equation (11) and cancelling through by ε and $\sqrt{V}$ gives

$$\ddot{\bar{\phi}}_1[1+\varepsilon^2V(B_1\bar{u}_1+B_2\bar{u}_2)^2]+\varepsilon^2\dot{\bar{\phi}}_1[2V(B_1\dot{\bar{u}}_1+B_2\dot{\bar{u}}_2)(B_1\bar{u}_1+B_2\bar{u}_2)]$$
$$+\varepsilon^2\bar{\phi}_1[V(B_1\ddot{\bar{u}}_1+B_2\ddot{\bar{u}}_2)(B_1\bar{u}_1+B_2\bar{u}_2)]+\omega_t^2\bar{\phi}_1+2\varepsilon\zeta_t\omega_t\dot{\bar{\phi}}_1=0 \qquad (14)$$

3.4.2 Application of the Perturbation Method of Multiple Scales

The ordered generalised co-ordinates, $\bar{u}_1$, $\bar{u}_2$ and $\bar{\phi}_1$, are written in asymptotic series form,

$$\bar{u}_1=\bar{u}_{10}+\varepsilon\bar{u}_{11}+\varepsilon^2\bar{u}_{12}+\cdots$$

$$\bar{u}_2=\bar{u}_{20}+\varepsilon\bar{u}_{21}+\varepsilon^2\bar{u}_{22}+\cdots$$

$$\bar{\phi}_1=\bar{\phi}_{10}+\varepsilon\bar{\phi}_{11}+\varepsilon^2\bar{\phi}_{12}+\cdots \qquad (15) \text{ to } (17)$$

The series are assumed to be uniformly convergent. The derivatives are also treated in this way, giving, up to second order,

$$\frac{d}{dt}=D_0+\varepsilon D_1+\varepsilon^2D_2+\cdots \qquad \frac{d^2}{dt^2}=D_0^2+2\varepsilon D_0D_1+\varepsilon^2(2D_0D_2+D_1^2)+\cdots$$

where $t=T_0$ and $T_n=\varepsilon^nT_0$. Then equations (12) to (14) are arranged so that terms of the same order of ε are grouped together. Therefore we have,

$$\varepsilon^0: \qquad D_0^2\bar{u}_{10}+\omega_1^2\bar{u}_{10}=0 \quad D_0^2\bar{u}_{20}+\omega_2^2\bar{u}_{20}=0 \quad D_0^2\bar{\phi}_{10}+\omega_t^2\bar{\phi}_{10}=0 \qquad (18)$$

ε^1:

$$D_0^2\bar{u}_{11}+\omega_1^2\bar{u}_{11}=-2D_0D_1\bar{u}_{10}-2\zeta_1\omega_1D_0\bar{u}_{10}-\bar{p}^2\bar{u}_{20}-\hat{A}_B\Omega^2\cos(\Omega t)(X\bar{u}_{10}+Y\bar{u}_{20})$$

$$D_0^2\bar{u}_{21}+\omega_2^2\bar{u}_{21}=-2D_0D_1\bar{u}_{20}-2\zeta_2\omega_2D_0\bar{u}_{20}-\bar{p}^2\bar{u}_{10}-\hat{A}_B\Omega^2\cos(\Omega t)(Y\bar{u}_{10}+Z\bar{u}_{20})$$

$$D_0^2\bar{\phi}_{11}+\omega_t^2\bar{\phi}_{11}=-2D_0D_1\bar{\phi}_{10}-2\zeta_t\omega_tD_0\bar{\phi}_{10} \qquad \text{(19) to (21)}$$

ε^2:

$$\begin{aligned}D_0^2\bar{u}_{12}+\omega_1^2\bar{u}_{12}=&-2D_0D_1\bar{u}_{11}-2D_0D_2\bar{u}_{10}-D_1^2\bar{u}_{10}-D_0^2\bar{u}_{10}B_1^2\bar{\phi}_{10}^2-D_0^2\bar{u}_{10}(X\bar{u}_{10}+Y\bar{u}_{20})^2\\&-2D_0\bar{u}_{10}D_0\bar{u}_{20}Y(X\bar{u}_{10}+Y\bar{u}_{20})-(D_0\bar{u}_{10})^2X(X\bar{u}_{10}+Y\bar{u}_{20})-\bar{p}^2\bar{u}_{21}\\&-(D_0\bar{u}_{20})^2Z(X\bar{u}_{10}+Y\bar{u}_{20})-D_0^2\bar{u}_{20}(X\bar{u}_{10}+Y\bar{u}_{20})(Y\bar{u}_{10}+Z\bar{u}_{20})\\&-B_1^2V\bar{\phi}_{10}D_0^2\bar{\phi}_{10}\bar{u}_{10}-2B_1^2V\bar{\phi}_{10}D_0\bar{\phi}_{10}D_0\bar{u}_{10}-2B_1B_2V\bar{\phi}_{10}D_0\bar{\phi}_{10}D_0\bar{u}_{20}\\&-B_1B_2V\bar{\phi}_{10}D_0^2\bar{\phi}_{10}\bar{u}_{20}-B_1B_2V\bar{\phi}_{10}^2D_0^2\bar{u}_{20}-2\zeta_1\omega_1D_0\bar{u}_{11}-2\zeta_1\omega_1D_1\bar{u}_{10}\\&-\hat{A}_B\Omega^2\cos(\Omega t)(X\bar{u}_{11}+Y\bar{u}_{21})\end{aligned}$$

$$\begin{aligned}D_0^2\bar{u}_{22}+\omega_2^2\bar{u}_{22}=&-2D_0D_1\bar{u}_{21}-2D_0D_2\bar{u}_{20}-D_1^2\bar{u}_{20}-D_0^2\bar{u}_{20}B_2^2\bar{\phi}_{10}^2-D_0^2\bar{u}_{20}(Y\bar{u}_{10}+Z\bar{u}_{20})^2\\&-2D_0\bar{u}_{10}D_0\bar{u}_{20}Y(Y\bar{u}_{10}+Z\bar{u}_{20})-(D_0\bar{u}_{20})^2Z(Y\bar{u}_{10}+Z\bar{u}_{20})-\bar{p}^2\bar{u}_{11}\\&-(D_0\bar{u}_{20})^2X(Y\bar{u}_{10}+Z\bar{u}_{20})-D_0^2\bar{u}_{10}(X\bar{u}_{10}+Y\bar{u}_{20})(Y\bar{u}_{10}+Z\bar{u}_{20})\\&-B_2^2V\bar{\phi}_{10}D_0^2\bar{\phi}_{10}\bar{u}_{20}-2B_2^2V\bar{\phi}_{10}D_0\bar{\phi}_{10}D_0\bar{u}_{20}-2B_1B_2V\bar{\phi}_{10}D_0\bar{\phi}_{10}D_0\bar{u}_{10}\\&-B_1B_2V\bar{\phi}_{10}D_0^2\bar{\phi}_{10}\bar{u}_{10}-B_1B_2V\bar{\phi}_{10}^2D_0^2\bar{u}_{10}-2\zeta_1\omega_2D_0\bar{u}_{21}-2\zeta_2\omega_2D_1\bar{u}_{20}\\&-\hat{A}_B\Omega^2\cos(\Omega t)(Y\bar{u}_{11}+Z\bar{u}_{21})\end{aligned}$$

$$\begin{aligned}D_0^2\bar{\phi}_{12}+\omega_t^2\bar{\phi}_{12}=&-2D_0D_1\bar{\phi}_{11}-2D_0D_2\bar{\phi}_{10}-D_1^2\bar{\phi}_{10}-D_0^2\bar{\phi}_{10}V(B_1\bar{u}_{10}+B_2\bar{u}_{20})^2\\&-D_0\bar{\phi}_{10}[2V(B_1D_0\bar{u}_{10}+B_2D_0\bar{u}_{20})(B_1\bar{u}_{10}+B_2\bar{u}_{20})]\\&-\bar{\phi}_{10}[V(B_1D_0^2\bar{u}_{10}+B_2D_0^2\bar{u}_{20})(B_1\bar{u}_{10}+B_2\bar{u}_{20})]\\&-2\zeta_t\omega_tD_0\bar{\phi}_{11}-2\zeta_t\omega_tD_1\bar{\phi}_{10}\end{aligned} \qquad \text{(22) to (24)}$$

3.5 Theoretical Analysis of the First-order Perturbation Equations

Solutions to the zeroth order perturbation equations are,

$$\bar{u}_{10}=A_1e^{i\omega_1T_0}+\bar{A}_1e^{-i\omega_1T_0},\bar{u}_{20}=A_2e^{i\omega_2T_0}+\bar{A}_2e^{-i\omega_2T_0},\bar{\phi}_{10}=C_1e^{i\omega_tT_0}+\bar{C}_1e^{-i\omega_tT_0}\ . \qquad \text{(25) to (27)}$$

Substituting these solutions into the first order equations leads to ($\omega_2>\omega_1$)

$$D_0^2\overline{u}_{11}+\omega_1^2\overline{u}_{11}=e^{i\omega_1 T_0}\left\{\begin{array}{l}-i2\omega_1 D_1A_1-i2\zeta_1\omega_1^2A_1-\dfrac{\hat{A}_B\Omega^2}{2}XA_1e^{-i\Omega T_0}-\dfrac{\hat{A}_B\Omega^2}{2}YA_2e^{-i(\Omega+\omega_1-\omega_2)T_0}\\-\dfrac{\hat{A}_B\Omega^2}{2}Y\overline{A}_2e^{-i(\Omega+\omega_1+\omega_2)T_0}-\dfrac{\hat{A}_B\Omega^2}{2}X\overline{A}_1e^{-i(\Omega+2\omega_1)T_0}-\dfrac{\hat{A}_B\Omega^2}{2}XA_1e^{i\Omega T_0}\\-\dfrac{\hat{A}_B\Omega^2}{2}YA_2e^{i(\Omega-\omega_1+\omega_2)T_0}-\dfrac{\hat{A}_B\Omega^2}{2}X\overline{A}_1e^{i(\Omega-2\omega_1)T_0}-\dfrac{\hat{A}_B\Omega^2}{2}Y\overline{A}_2e^{i(\Omega-\omega_1-\omega_2)T_0}\\+(i2\zeta_1\omega_1^2\overline{A}_1+i2\omega_1D_1\overline{A}_1)e^{-i2\omega_1T_0}-\overline{p}^2A_2e^{i(\omega_2-\omega_1)T_0}-\overline{p}^2\overline{A}_2e^{-i(\omega_1+\omega_2)T_0}\end{array}\right\}$$

$$D_0^2\overline{u}_{21}+\omega_2^2\overline{u}_{21}=e^{i\omega_2 T_0}\left\{\begin{array}{l}-i2\omega_2 D_1A_2-i2\zeta_2\omega_2^2A_2-\dfrac{\hat{A}_B\Omega^2}{2}ZA_2e^{-i\Omega T_0}-\dfrac{\hat{A}_B\Omega^2}{2}YA_1e^{-i(\Omega-\omega_1+\omega_2)T_0}\\-\dfrac{\hat{A}_B\Omega^2}{2}Y\overline{A}_1e^{-i(\Omega+\omega_1+\omega_2)T_0}-\dfrac{\hat{A}_B\Omega^2}{2}Z\overline{A}_2e^{-i(\Omega+2\omega_2)T_0}-\dfrac{\hat{A}_B\Omega^2}{2}ZA_2e^{i\Omega T_0}\\-\dfrac{\hat{A}_B\Omega^2}{2}YA_1e^{i(\Omega+\omega_1-\omega_2)T_0}-\dfrac{\hat{A}_B\Omega^2}{2}Y\overline{A}_1e^{i(\Omega-\omega_1-\omega_2)T_0}-\dfrac{\hat{A}_B\Omega^2}{2}Z\overline{A}_2e^{i(\Omega-2\omega_2)T_0}\\+(i2\zeta_2\omega_2^2\overline{A}_2+i2\omega_2D_1\overline{A}_2)e^{-i2\omega_2T_0}-\overline{p}^2A_1e^{i(\omega_1-\omega_2)T_0}-\overline{p}^2\overline{A}_1e^{-i(\omega_1+\omega_2)T_0}\end{array}\right\}$$

$$D_0^2\overline{\phi}_{11}+\omega_t^2\overline{\phi}_{11}=e^{i\omega_t T_0}\left\{-i2\omega_tD_1C_1-i2\zeta_t\omega_t^2C_1+(i2\zeta_t\omega_t^2\overline{C}_1+2i\omega_tD_1\overline{C}_1)e^{-i2\omega_tT_0}\right\}\qquad (28)\text{ to }(30)$$

Now the step is to consider how the first-order perturbation equations , i.e., equations (28) to (30) should be treated so that their paticular solutions do not invalidate the important underlying necessity for uniformity in the expansions, as assumed as equations (15) to (17). This uniformity is not likely to occur if certain terms are present in the above equations. Those terms are called secular terms. The danger of these terms will creat disproportionate increase in the magnitudes of $\overline{u}_{11}$, $\overline{u}_{21}$, and $\overline{\phi}_{11}$ if they are not removed. Equation (28) is taken as an example, the eaiest way of tackling the secular term problems is to take out the resonant exponet terms, which only contain the term $e^{i\omega_1 T_0}$ (noting the conjugates which contain $e^{-i\omega_1 T_0}$), in this case, the terms $-i2\omega_1D_1A_1$ and $-i2\zeta_1\omega_1^2A_1$. The terms $\dfrac{\hat{A}_B\Omega^2}{2}X\overline{A}_1e^{i(\Omega-2\omega_1)T_0}$, $\dfrac{\hat{A}_B\Omega^2}{2}Y\overline{A}_2e^{i(\Omega-\omega_1-\omega_2)T_0}$, $\dfrac{\hat{A}_B\Omega^2}{2}YA_2e^{-i(\Omega+\omega_1-\omega_2)T_0}$ might be resonant if $\Omega=2\omega_1$ or $\Omega=\omega_1+\omega_2$ or $\Omega=\omega_2-\omega_1$. Likewise for the equation (29). The conditions $\Omega=2\omega_2$ and $\Omega=\omega_1+\omega_2$ and $\Omega=\omega_2-\omega_1$ will also generate further secular terms. $\Omega=2\omega_1$ and $\Omega=2\omega_2$ are regarded as primary parametric resonances, while $\Omega=\omega_1+\omega_2$ and $\Omega=\omega_2-\omega_1$ are termed combination resonances.

3.5.1 Non-resonant Case

The non-resonance case is the case when Ω is away from $2\omega_1$, $2\omega_2$, $\omega_1+\omega_2$ and $\omega_2-\omega_1$. In this case, the secular terms in equation (28) are only $-i2\omega_1 D_1 A_1$ and $-i2\zeta_1\omega_1^2 A_1$. The sum of this two terms should be zero, expressed as follows,

$$-i2\omega_1 D_1 A_1 - i2\zeta_1\omega_1^2 A_1 = 0 \tag{31}$$

Equation (31) is also called the solvability condition because it is used to solve A_1 in general.

Conventionally, one lets $A_1 = \frac{a_1}{2}e^{i\alpha_1}$, so that, $D_1 A_1 = \frac{a_1'}{2}e^{i\alpha_1} + i\frac{a_1}{2}\alpha_1' e^{i\alpha_1}$. Here $a_1 = a_1(T_1, T_2)$, $\alpha_1 = \alpha_1(T_1, T_2)$ and then, after substitution into equation (31), it can be separated into real and imaginary parts in order to obtain the modulation equations for the non-resonant case,

$$a_1' + \zeta_1\omega_1 a_1 = 0 \quad \text{and} \quad a_1\alpha_1' = 0 \tag{32),(33}$$

Here in the section 3.5 of this chapter, the prime denotes differentiation with respect to T_1.

Solving for a_1 and α_1 leads to,

$$a_1 = a_{10}e^{-\zeta_1\omega_1 T_1} \text{ and } \alpha_1 = \alpha_{10} \tag{34),(35}$$

Where a_{10}, α_{10} are arbitrary constants.

With the solvability condition (equation (31)) fulfilled, a particular solution to equation (28) is obtained by adding in turn the responses to each of the remaining harmonic excitation terms. Mathematica™ code (see **Appendix 3**) has been developed to achieve this purpose.

$$\begin{aligned}\bar{u}_{11} = &-\frac{X\Omega^2\cos(\Omega T_0 - \omega_1 T_0 - \alpha_1)\hat{A}_B a_1}{-2\Omega^2 + 4\Omega\omega_1} + \frac{X\Omega^2\cos(\Omega T_0 + \omega_1 T_0 + \alpha_1)\hat{A}_B a_1}{2\Omega^2 + 4\Omega\omega_1} - \frac{\bar{p}^2\cos(\omega_2 T_0 + \alpha_1)a_1}{\omega_1^2 - \omega_2^2} \\ &- \frac{Y\Omega^2\cos(\Omega T_0 + \omega_2 T_0 + \alpha_2)\hat{A}_B a_2}{-2\Omega^2 + 2\omega_1^2 - 4\Omega\omega_2 - 2\omega_2^2} - \frac{Y\Omega^2\cos(\Omega T_0 - \omega_2 T_0 - \alpha_2)\hat{A}_B a_2}{-2\Omega^2 + 2\omega_1^2 + 4\Omega\omega_2 - 2\omega_2^2}\end{aligned} \tag{36}$$

Equation (34) shows that $a_1 \to 0$ as $T_1 \to \infty$, then $A_1 \to 0$, and from equations (15), (25), and (36) the stationary response for $\bar{u}_1$ becomes $\bar{u}_1 = 0$ if we only consider the zeroth and first order perturbation equations.

Likewise for u_2, leading to,

$$\bar{u}_{21} = -\frac{Z\Omega^2 \cos(\Omega T_0 + \omega_2 T_0 + \alpha_2)\hat{A}_B a_2}{2\Omega^2 + 4\Omega\omega_2} + \frac{Z\Omega^2 \cos(\Omega T_0 - \omega_2 T_0 - \alpha_2)\hat{A}_B a_2}{2\Omega^2 - 4\Omega\omega_2} + \frac{\bar{p}^2 \cos(\omega_1 T_0 + \alpha_1)a_1}{\omega_1^2 - \omega_2^2}$$
$$- \frac{Y\Omega^2 \cos(\Omega T_0 + \omega_1 T_0 + \alpha_1)\hat{A}_B a_1}{-2\Omega^2 - 2\omega_1^2 - 4\Omega\omega_1 + 2\omega_2^2} - \frac{Y\Omega^2 \cos(\Omega T_0 - \omega_1 T_0 - \alpha_1)\hat{A}_B a_1}{-2\Omega^2 - 2\omega_1^2 + 4\Omega\omega_1 + 2\omega_2^2} \tag{37}$$

After removing the secular terms and their conjugates from the right hand side of equation (28), the first order perturbation solution is $\bar{\phi}_{11} = 0$.

3.5.2 Transition Curves for the Primary Parametric Resonance Case

In this case $\Omega \approx 2\omega_1 + \varepsilon\sigma$ and its solvability condition is

$$i2\omega_1(D_1 A_1 + \zeta_1 \omega_1^2 A_1) + \frac{\hat{A}_B \Omega^2}{2} X \bar{A}_1 e^{i\sigma T_1} = 0 \tag{38}$$

For determining $A_1(T_1, T_2)$, again like in the non-resonant case, we let $A_1 = \frac{a_1}{2} e^{i\alpha_1}$, where $a_1 = a_1(T_1, T_2)$, $\alpha_1 = \alpha_1(T_1, T_2)$, Substituting of A_1, $\bar{A}_1$ and $D_1 A_1$ into equation (38) and separating the real and imaginary parts gives the modulation equations for the primary parametric resonance case as follows

$$a_1' = -\zeta_1 \omega_1 a_1 - \frac{1}{4\omega_1} X \hat{A}_B \Omega^2 \sin(\sigma T_1 - 2\alpha_1) a_1 \tag{39}$$

$$\alpha_1' = \frac{1}{4\omega_1} X \hat{A}_B \Omega^2 \cos(\sigma T_1 - 2\alpha_1) \tag{40}$$

Since slowly varying parameters (with respect to slow time scale T_1 but not T_0) appear in the above two equations, it is reasonable to assume that the amplitude is almost static in slow time. Therefore

$$a_1' = 0 \tag{41}$$

We also eliminate the explicit presence of time (in whatever time-scale form it is represented) and in so doing obtain an autonomous system by stating

$$\Psi = \sigma T_1 - 2\alpha_1 \tag{42}$$

The phase Ψ is considered as the same way as the above amplitude by setting $\Psi' = 0$. It is then clear that $\sigma = 2\alpha_1'$ from equation (42).

Substituting equation (41) and $\sigma = 2\alpha_1'$ into equations (39) and (40) yields

$$-\zeta_1\omega_1 a_1 - \frac{1}{4\omega_1} X\hat{A}_B\Omega^2 a_1 \sin\Psi = 0 \tag{43}$$

$$\sigma = \frac{1}{2\omega_1} X\hat{A}_B\Omega^2 \cos\Psi \tag{44}$$

According to the identity whereby $\sin^2\Psi + \cos^2\Psi = 1$, where $\sin\Psi$, $\cos\Psi$ are from equations (43) and (44), this leads to

$$(\frac{4\zeta_1\omega_1^2}{X\hat{A}_B\Omega^2})^2 + (\frac{2\sigma\omega_1}{X\hat{A}_B\Omega^2})^2 = 1 \tag{45}$$

And hence,

$$\sigma = \pm\sqrt{(\frac{X}{2\omega_1})^2(\hat{A}_B\Omega^2)^2 - (2\zeta_1\omega_1)^2} \tag{46}$$

Equation (46) can be used to plot a stability chart for the primary resonance $\Omega \approx 2\omega_1 + \varepsilon\sigma$ in such a manner that the detuning parameter σ is the ordinate and an excitation parameter $\hat{A}_B\Omega^2$ is on the abscissa. A stability chart can also be called a transition curve, a curve which divides the chart into areas of stability and instability as shown in Fig 3-3 for a specific system. A (σ, $\hat{A}_B\Omega^2$) coordinate outside the shaded area, when $\zeta_1 = 0.001$, defines a stable response and within the shaded regions defines an unstable response. The coordinates on the curve are boundary stability.

In equation (46), clearly, we require, $(\frac{X}{2\omega_1})^2(\hat{A}_B\Omega^2)^2-(2\zeta_1\omega_1)^2\geq 0$, or, $(\hat{A}_B\Omega^2)\geq\frac{4\zeta_1\omega_1^2}{X}$, when $\hat{A}_B\Omega^2\geq 0$.

In the case of the other primary resonance, in which, $\Omega=2\omega_2+\varepsilon\delta$ it can be shown that,

$$\delta=\pm\sqrt{(\frac{Z}{2\omega_2})^2(\hat{A}_B\Omega^2)^2-(2\zeta_2\omega_2)^2} \tag{47}$$

for which, $(\frac{Z}{2\omega_2})^2(\hat{A}_B\Omega^2)^2-(2\zeta_2\omega_2)^2\geq 0$, or, $(\hat{A}_B\Omega^2)\geq\frac{4\zeta_2\omega_2^2}{Z}$ when $\hat{A}_B\Omega^2\geq 0$. This is the equation for the transition curve for the primary resonance $\Omega=2\omega_2+\varepsilon\delta$.

3.5.3 Transition Curve for the Sum-type Combination Resonance

In this case we have, $\Omega=\omega_1+\omega_2+\varepsilon\alpha$

The solvability conditions are,

$$-i2\omega_1D_1A_1-i2\zeta_1\omega_1^2A_1-\frac{\hat{A}_B\Omega^2}{2}Y\bar{A}_2e^{i\alpha T_1}=0 \tag{48}$$

$$-i2\omega_2D_1A_2-i2\zeta_2\omega_2^2A_2-\frac{\hat{A}_B\Omega^2}{2}Y\bar{A}_1e^{i\alpha T_1}=0 \tag{49}$$

Substituting $A_1=\frac{a_1}{2}e^{i\alpha_1}$, $A_2=\frac{a_2}{2}e^{i\alpha_2}$, $D_1A_1=\frac{a_1'}{2}e^{i\alpha_1}+i\frac{a_1}{2}\alpha_1'e^{i\alpha_1}$ $D_1A_2=\frac{a_2'}{2}e^{i\alpha_2}+i\frac{a_2}{2}\alpha_2'e^{i\alpha_2}$ in to the solvability conditions one obtains, upon separating real and imaginary parts, the following set of modulation equations:

$$\omega_1a_1\alpha_1'-\frac{\hat{A}_B\Omega^2a_2}{4}YCos\Psi=0 \tag{50}$$

$$-\omega_1a_1'-\zeta_1\omega_1^2a_1+\frac{\hat{A}_B\Omega^2a_2}{4}YSin\Psi=0 \tag{51}$$

$$\omega_2a_2\alpha_2'-\frac{\hat{A}_B\Omega^2a_1}{4}YCos\Psi=0 \tag{52}$$

$$-\omega_2 a_2{}' - \zeta_2 \omega_2^2 a_2 + \frac{\hat{A}_B \Omega^2 a_1}{4} Y Sin\Psi = 0 \tag{53}$$

here $\Psi = \alpha_1 + \alpha_2 - \alpha T_1$ and $e^{\pm i\Psi} = Cos\Psi \pm iSin\Psi$ (54)

Equations $Cos\Psi = \frac{4\omega_1 a_1 \alpha_1{}'}{\hat{A}_B \Omega^2 a_2 Y}$, $Cos\Psi = \frac{4\omega_2 a_2 \alpha_2{}'}{\hat{A}_B \Omega^2 a_1 Y}$ can be obtained from equations (50) and (52) separately. Equating these two equations leads to

$$\frac{4\omega_1 a_1 \alpha_1{}'}{\hat{A}_B \Omega^2 a_2 Y} = \frac{4\omega_2 a_2 \alpha_2{}'}{\hat{A}_B \Omega^2 a_1 Y} \rightarrow \omega_1 a_1^2 \alpha_1{}' = \omega_2 a_2^2 \alpha_2{}' \tag{55}$$

Equations (51) and (53) are treated in the same manner and the following is given

$$\zeta_1 \omega_1^2 a_1^2 = \zeta_2 \omega_2^2 a_2^2 \tag{56}$$

To achieve a steady state, the conditions are imposed that $a_1{}' = a_2{}' = \Psi' = 0$, and hence $\Psi' = \alpha_1{}' + \alpha_2{}' - \alpha = 0$ according to equation (54), and finally

$$\alpha_1{}' + \alpha_2{}' = \alpha \tag{57}$$

Equations (55) and (56) are now used in conjunction with equation (57) to find

$$\alpha_1{}' = \frac{\zeta_1 \omega_1 \theta}{\zeta_2 \omega_2 + \zeta_1 \omega_1} \qquad \alpha_2{}' = \frac{\zeta_2 \omega_2 \theta}{\zeta_2 \omega_2 + \zeta_1 \omega_1} \tag{58}$$

$Cos\Psi$ and $Sin\Psi$ are obtained from equations (51) and (52), and by using $Cos^2\Psi + Sin^2\Psi = 1$ we find

$$\left(\frac{4\omega_1 a_1 \alpha_1{}'}{\hat{A}_B \Omega^2 a_2 Y}\right)^2 + \left(\frac{4\zeta_1 \omega_1^2 a_1}{\hat{A}_B \Omega^2 a_2 Y}\right)^2 = 1 \tag{59}$$

Finally the equation for the transition curve is obtained by using equations (58) and (59)

$$\alpha = \pm \sqrt{\frac{(\zeta_1 \omega_1 + \zeta_2 \omega_2)^2 \left(\frac{Y^2 \Omega^4 \hat{A}_B^2}{\zeta_2 \omega_2^2} - 16\zeta_1 \omega_1^2\right)}{16\zeta_1 \omega_1^2}} \tag{60}$$

For which we require $\frac{(\zeta_1\omega_1+\zeta_2\omega_2)^2(\frac{Y^2\Omega^4\hat{A}_B^2}{\zeta_2\omega_2^2}-16\zeta_1\omega_1^2)}{16\zeta_1\omega_1^2}\geq 0$ or $\hat{A}_B\Omega^2\geq\frac{4\omega_1\omega_2}{|Y|}\sqrt{\zeta_1\zeta_2}$

3.5.4 Difference-type Combination Resonance Case

The difference-type instability is given by, $\Omega=\omega_2-\omega_1+\varepsilon\beta$

Its solvability condition is:

$$-i2\omega_1D_1A_1-i2\zeta_1\omega_1^2A_1-\frac{\hat{A}_B\Omega^2}{2}YA_2e^{-i\beta T_1}=0 \tag{61}$$

$$-i2\omega_2D_1A_2-i2\zeta_2\omega_2^2A_2-\frac{\hat{A}_B\Omega^2}{2}YA_1e^{i\beta T_1}=0 \tag{62}$$

The procedure for solving equations (61) and (62) is like that in the sum-type combination resonance case. However, it can only be shown in this case that, $\frac{a_1^2}{a_2^2}=-\frac{\zeta_2\omega_2^2}{\zeta_1\omega_1^2}$, and this has no physical significance because damping and natural frequencies are necessarily positive. Therefore in the case of $\Omega=\omega_2-\omega_1+\varepsilon\beta$ only trivial zero solutions are admitted.

3.6 Theoretical Analysis of the Second-order Perturbation Equations

The procedure for solving the second-order perturbation equations is explained as follows. First, the zeroth-order perturbation solutions (equations (25) to (27)) and first-order perturbation solutions (equations (36) and (37)) are substituted into the second-order perturbation equations (equations (22) to (24)), and they are re-organized in the same forms as in equations (28) to (30); Second, the secular terms that contain the term $e^{i\omega_1t}$ and the conjugates $e^{-i\omega_1t}$ are removed. Finally the solutions are obtained by adding in turn the responses to each of the remaining harmonic terms. The resonances from the second-order perturbation equations are obtained when the coefficients to $e^{i\omega_1t}$ equate to zero and so are the coefficients to $e^{-i\omega_1t}$. The results are listed in **Appendix 4**. A detailed and complete treatment for analyzing the second-order perturbation equations is available in Cartmell (1990).

3.7 Effects of Non-linearities

The non-linearities which appear in equations (9) to (11) arise because we consider the small displacement in the Oyz plane, v. This displacement v results from combined bending u and torsion ϕ and it is expressed as $v = B_1\phi_1 u_1 + B_2\phi_1 u_2$. These non-linearities are referred as geometrical non-linearities. To see their effects on the problem, the linear part of these equations are written separately as follows

$$\ddot{\bar{u}}_1 + 2\varepsilon\zeta_1\omega_1\dot{\bar{u}}_1 + \omega_1^2\bar{u}_1 + \varepsilon\bar{p}^2\bar{u}_2 + \varepsilon\hat{A}_B\Omega^2\cos(\Omega t)(X\bar{u}_1 + Y\bar{u}_2) = 0$$

$$\ddot{\bar{u}}_2 + 2\varepsilon\zeta_2\omega_2\dot{\bar{u}}_2 + \omega_2^2\bar{u}_2 + \varepsilon\bar{p}^2\bar{u}_1 + \varepsilon\hat{A}_B\Omega^2\cos(\Omega t)(Y\bar{u}_1 + Z\bar{u}_2) = 0$$

$$\ddot{\bar{\phi}}_1 + 2\varepsilon\zeta_t\omega_t\dot{\bar{\phi}}_1 + \omega_t^2\bar{\phi}_1 = 0 \qquad \text{(63) to (65)}$$

Re-solving the three degree of freedom equations (63) to (65), which include the linear parametric and coupling terms, will yield the three parametric resonances $\Omega = 2\omega_1$ and $\Omega = \omega_1 + \omega_2$ and $\Omega = 2\omega_2$. Solving the second-order perturbation equations (22) to (24) provides more resonances as explained in section 3.6. Most of them are generated by the non-linearities. These types of non-linearity are commonly neglected in practise because they are considered to be relatively weak when compared with linear terms. However such neglect cannot always provide a complete answer to all problems.

3.8 Discussion of Theoretical and Experimental Results

3.8.1 Theoretical Results

A beam is taken as an example, with parameters as listed in Table 3-2. The following theoretical and experimental results are based on this case. According to equations (46), (47) and (60), transition curves for the above three resonances are plotted in Figures 3-3, 3-4 and 3-5. Figures 3-3, 3-4 and 3-5 show the theoretical transition values for resonances $\Omega \approx 2\omega_1 + \varepsilon\sigma$, $\Omega = \omega_1 + \omega_2 + \varepsilon\alpha$ and $\Omega = 2\omega_2 + \varepsilon\delta$. The horizontal axes are the detuning parameters $\varepsilon\sigma$, $\varepsilon\alpha$ and $\varepsilon\delta$ respectively. The vertical axis is the excitation acceleration. Stable (or zero response) behaviour occurs outside the boundary of the curve whilst points within the curve define unstable, theoretically unbounded, modal responses. Points

occurring on the curve are known as transition values. In the three cases, the greater the degree of detuning the greater the level of excitation that is required to promote the instability; The effects of damping on the shape of the curves are highlighted. With increasing daming ratios, the unstable regions tend to move away from the frequency axis. That means that when the damping ratio is increased, it is more difficult to get into the untable zone. It is also noticed that the greater the damping ratio the narrower of the unstable zone.

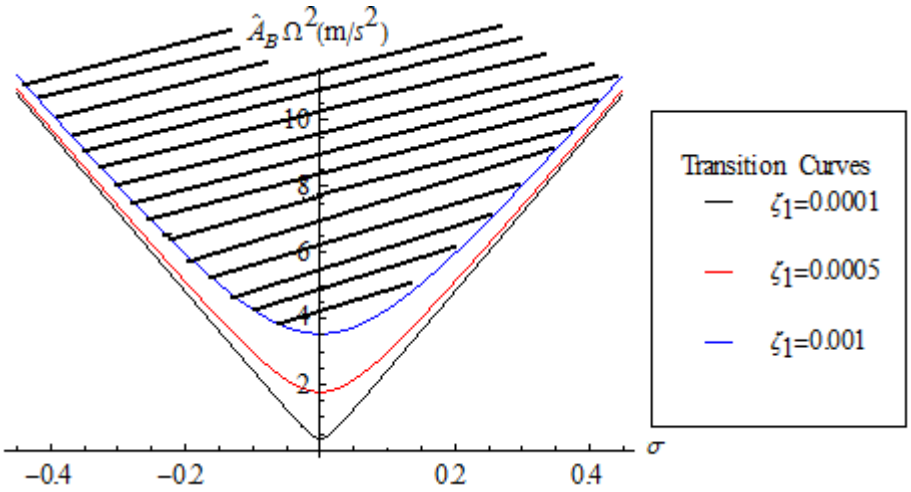

Fig 3-3 Stability chart showing the zoning for the principal parametric resonance $\Omega \approx 2\omega_1 + \varepsilon\sigma$

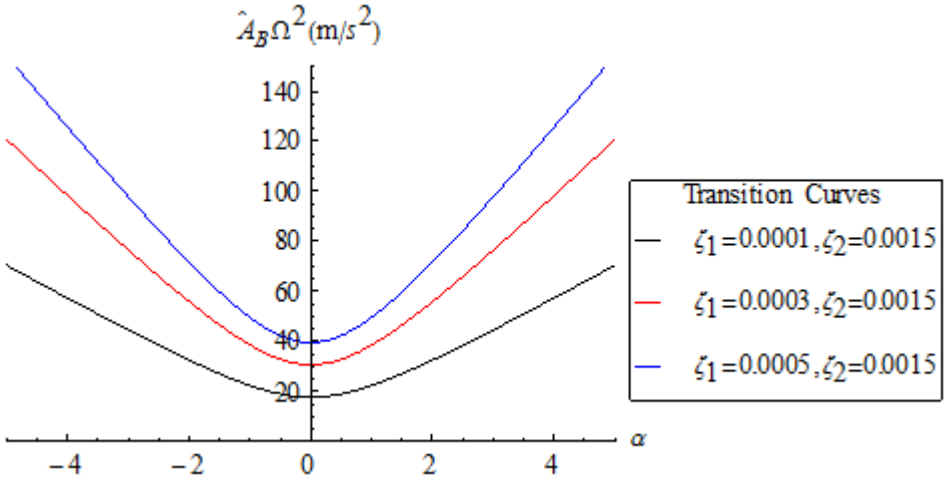

Fig 3-4 Stability chart showing the zoning for the combination resonance $\Omega = \omega_1 + \omega_2 + \varepsilon\alpha$

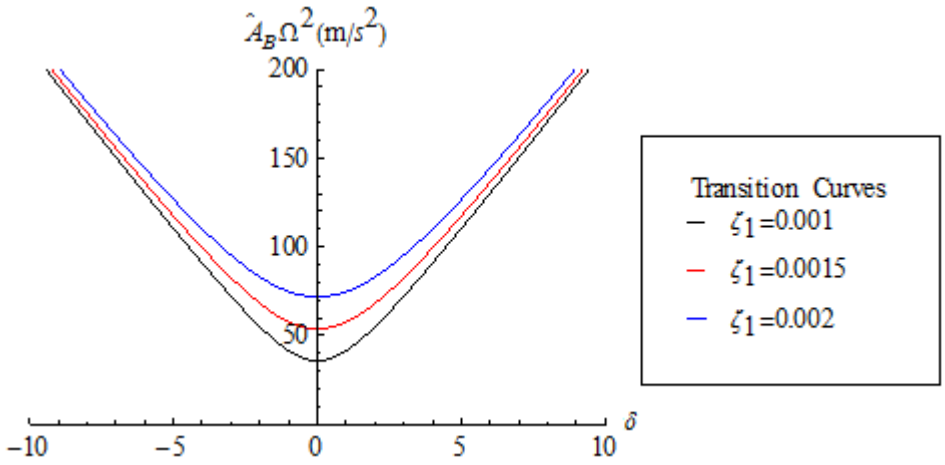

Fig 3-5 Stability chart showing the zoning for the principal parametric resonance $\Omega = 2\omega_2 + \varepsilon\delta$

3.8.2 Experimental Work

Tests were carried out on a laboratory model to corroborate the theoretical results. The details of the model are given in Figure 3-6, with properties listed in Table 3-1. The rig consisted of a short flexible spring steel beam, which was driven by an electromagnetic shaker from a function generator and current drive amplifier. A rectangular lumped end mass of length 45 mm, thickness 16 mm and depth 15 mm, made of aluminium, was attached at the free end of the beam. A spectrum analyzer connected to a vibrometer control unit enables the identification of the beam responses through the signals which come from a laser vibrometer. The excitation of the shaker was monitored by means of an accelerometer tightly mounted on the clamping fixture. The list of the instruments used in the experimental investigations has been included in **Appendix 6**. The excitation accelerations displayed on the oscilloscope (in terms of volts) could be directly related to physical accelerations by a calibrated charge amplifier. Please see the flowchart in Figure 3-6. The first and second natural frequencies of bending motions were obtained by directly exciting the bending modes. To this end the beam was linearly excited in the x-axis shown in Figure 3-1 at the two natural frequencies of interest. Two peaks, with frequencies of 11 Hz and 137 Hz, were read from the screen of the spectrum analyzer. These frequencies were the first and second natural frequencies of bending motions respectively. The two frequencies are close to the frequencies from theoretical work, which are 11.3 Hz and 132.8 Hz. The corresponding critical damping ratios ζ_i for each bending mode were found from captured transient decays when the shaker was abruptly stopped following a resonance

build-up. For when $\Omega \approx 2\omega_1$, the laser vibrometer picked up the first bending mode, while when $\Omega \approx 2\omega_2$, the laser vibrometer picked up the second bending mode. The decays were stored in the oscilloscope and the slopes were measured at different amplitudes. The results are $\zeta_1 = 0.001$ and $\zeta_2 = 0.0042$. Experimental points for the transition curves as shown in Figures 3-8, 3-9, 3-10, were found by selecting a range of frequencies on the function generator, and at each point the excitation level was increased very slowly until nonplanar motion commenced. To observe the nonplanar motion, the laser vibrometer was used again to catch the response signal and it was connected with the spetrum analyzer to display the reponse in frequency domain. The gain of the excitation was gradually increased until the peak of the natural frequency of the first bending mode appeared on the spectrum analyzer screen, which means the instability of the $\Omega \approx 2\omega_1$ roughly starts. Likewise, the appearance of the natural frequency of the second bending mode, of both the frequencies are for $\Omega \approx 2\omega_2$ and $\Omega \approx \omega_1 + \omega_2$ separetely. The excitation acceleration and frequency values were recorded for the above three resonances. The beam showed no nonplanar motion when the excitation frequencies are in the range of $\Omega \approx \omega_2 - \omega_1$. It is shown from Figures 3-8, 3-9 and 3-10 that close agreement is obtained between theoretical and experimental results. It is also noticed in Figure 3-8, the experimental results fall outwith the theoretical curve. The possible explaination is that the damping ratio obtained in the laboratory is less than its real value. As dicussed above, transition curves tend to move upwards when damping is increased. However this only affects the middle part of the curve because the curve meanwhile becomes narrower when the level of damping is increased, which results in the experimental results will fall above the transition curve at the greater detuning points. The disagreement between the theoretical and experimental results needs further investigation.

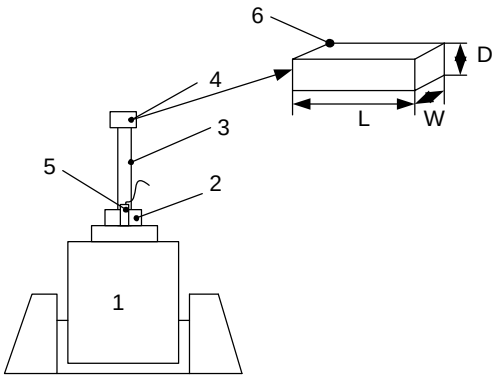

Fig 3-6 Experimental rig. (1) shaker, (2) clamps, (3) beam,(4) end mass, (5) accelerometer, (6) enlarged end mass

Symbol	l (m)	l_0 (m)	ρ (kg/ m^3)	W_b (m)	T_b (m)
Value	0.128	0.1355	7800	0.025	$7.2*10^{-4}$
Symbol	A (m^2)	m (kg/m)	m_0 (kg)	W_m (m)	D_m (m)
Value	$1.8*10^{-5}$	0.1404	0.031	0.015	0.016

Table 3-1 Properties of the experimental rig

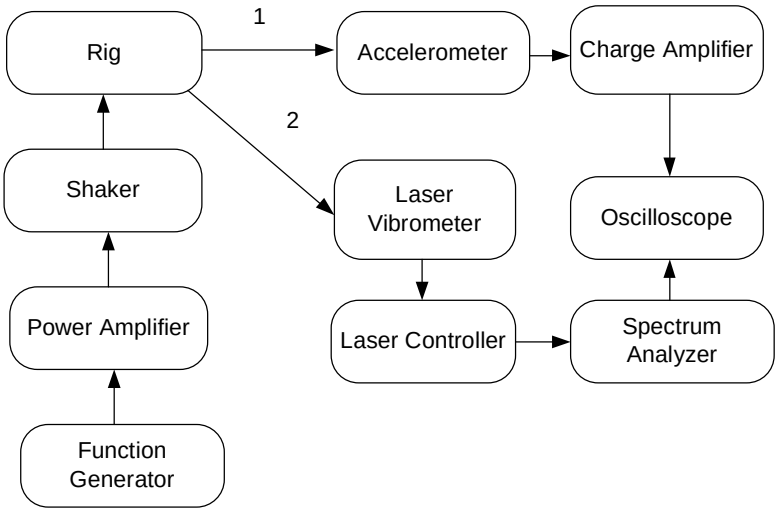

Fig 3-7 Flowchart of the response signal marked by 2 and excitation signal by 1 of the experiments

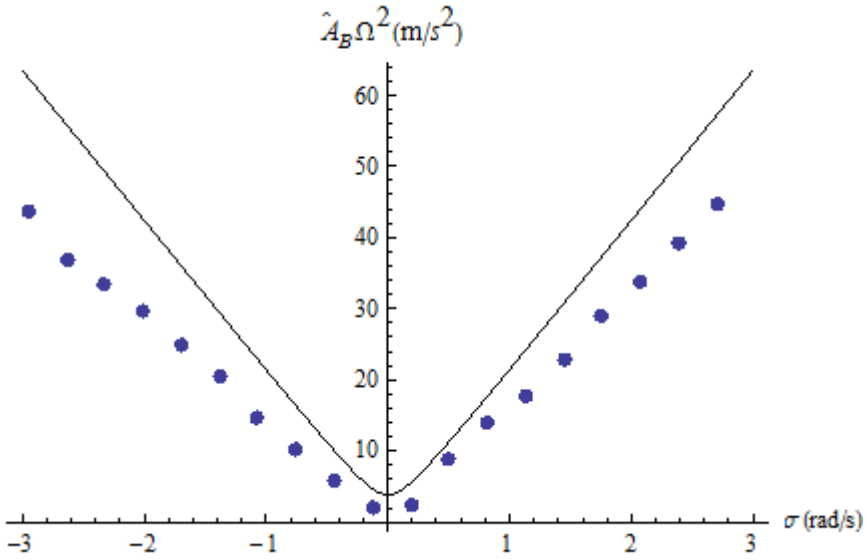

Fig 3-8 Theoretical and experimental transition curves for $\Omega \approx 2\omega_1 + \varepsilon\sigma$ (experimental points dotted)

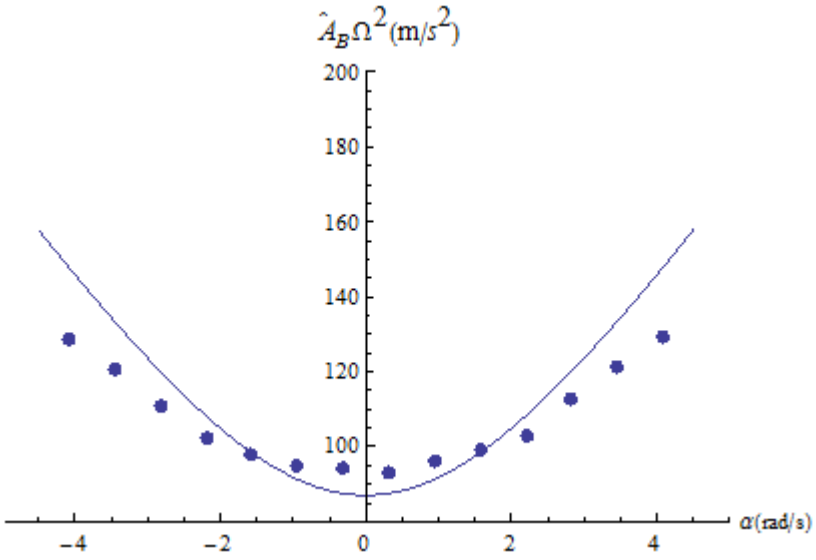

Fig 3-9 Theoretical and experimental transition curves for $\Omega = \omega_1 + \omega_2 + \varepsilon\alpha$ (experimental points dotted)

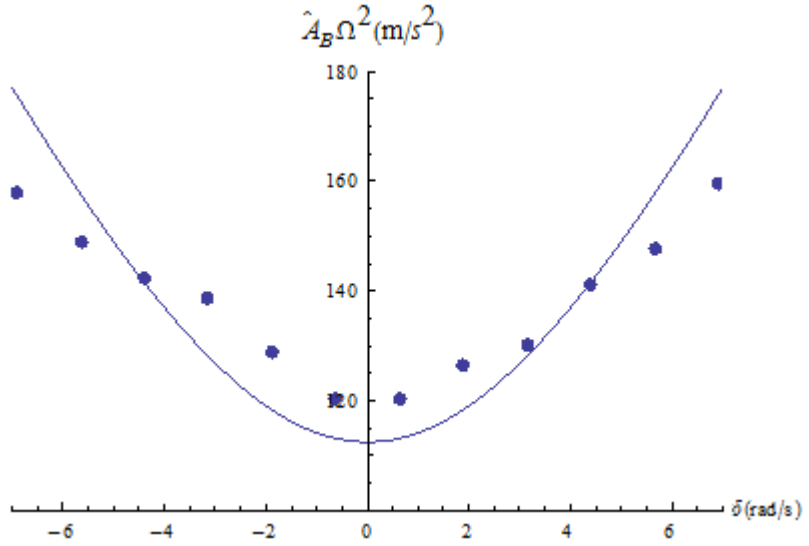

Fig 3-10 Theoretical and experimental transition curves for $\Omega = 2\omega_2 + \varepsilon\delta$ (experimental points dotted)

Chapter 4

Experiments on Glass-epoxy Beams

4.1 Introduction

The mechanical properties of composite materials are conveniently studied from two points of view: micromechancis and macromechanics. In his book, Jones (1998) gave the definition of these two terms regarding the composite material study. "*Micromechanics* is the study of composite material behaviour wherein the interaction of the constituent materials is examined on a *microscopic* scale to determine their effect on the properties of the composite material. *Macromechanics* is the study of composite material behaviour wherein the material is presumed homogeneous and the effects of the constituent materials are detected only as averaged apparent macroscopic properties of the composite material. " The procedures of micromechanics are used to predict the properties. Based on micromechanics analysis, a generally accepted expression for the tensile modulus of the composite materials in the longitudinal direction is one of the Halpin-Tsai equations (1969).

$$\bar{E}_{11} = (E_{11})_f \phi + (E_{11})_m (1-\phi) \tag{1}$$

where the subscripts " f " and " m " denote the fibre (embedded) phase and matrix phase respectively. The volume fractions are ϕ and $(1-\phi)$, respectively. E_{11} is the tensile modulus along the longitudinal direction. The beams in the present study are produced by the COMPOSITE INNOVATIONS Ltd. The material details are provided by this manufacturer as follows

- Layup -- [0/90/45/-45/45/90/0] Ply area weight 466 g/m^2
- Fibre – EGlass
- Resin -- Sicomin 8100 epoxy with 8824 standard hardener
- Production volume fraction -- 50%±2%
- Cure – Ambient for 10 hours and followed by 3 hours at 90^{0}C

Table 4-1 reports some of the engineering properties of the beams also provided by the manufacturer. According to equation (1), the elastic modulus is calculated as 36.25 GPa, which is close to 36 GPa that the manufacturer supplied. However, micromechanical

analysis has its inherent limitations because the analysis requires a perfect bond between fibres and matrix. This will not happen in reality. Thus, micromechanical theories must be validated by careful experimental work. There are a few ways to obtain the tensile modulus for a rectangular cross-sectional glass epoxy (g-e) beam through experiments. This work considers two of them: the three point bending test, and the bending tests for a cantilever and a cantilever with an end mass. Torsional tests are also introduced in this chapter to obtain the shear modulus for the beams.

	Fibre volume fraction	Elasticity modulus (GPa)	Density (g/cc)	Poissons ratio
Composite	50% ± 2%	36	1.85	0.26
EGlass		69	2.56	0.2
Epoxy Prime 20		3.5	1.2	0.37

Table 4-1 Some of the properties of the manufactured glass epoxy beams

Note: The elasticity modulus and Poisons ratio for the composite are measured in the longitudinal direction.

4.2 Experimental Investigations

4.2.1 Tensile Modulus

4.2.1.1 Three Point Bending Test

A rectangular cross-section beam denoted as beam 1, of width 13 mm, thickness 2.2 mm and length 150 mm, was tested using the three point bending test, shown in Figure 4-1. The test was performed on a Lloyds 1000 R tensile testing machine. In this test, the support span length was set to 100 mm and then adjusted to 50 mm and the tests were repeated. The beam was supported towards either end and loaded in the middle. The load F was applied slowly so that the speed was 2mm/min. An AD converter and computer were used to obtain the load-deflection curves and the results are indicated in Figure 4-1. The equation requesting for calculating the tensile modulus E is:

$$E = \frac{L^3}{4bh^3} \cdot \frac{\Delta F}{\Delta d} \tag{2}$$

where E is the bending modulus of elasticity in MPa. L is the support span; b, the width of the test beam; h, the thickness of the test beam. All these three are in mm. ΔF is the change in force in the initial linear portion of the force/deflection curve in Newtons. Δd is the change in deflection corresponding to the change in force ΔF and is in mm. To get the bending modulus E, the linear relationship of the load and the deflection is guaranteed during the whole process.

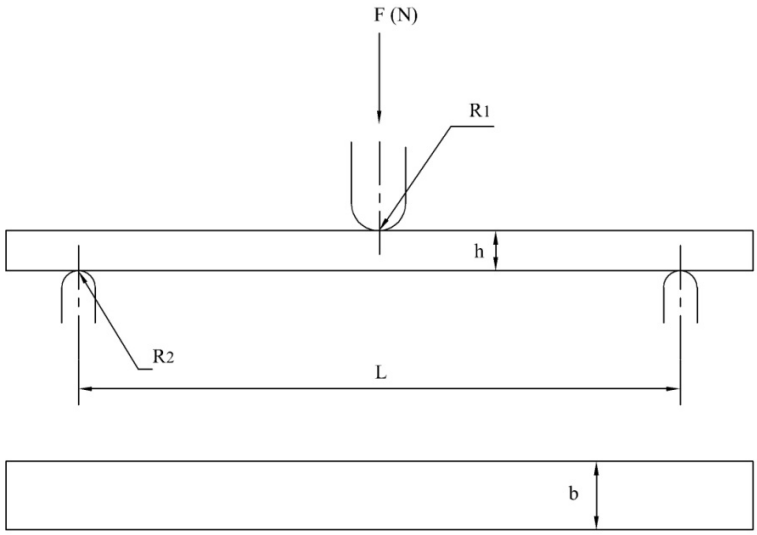

Fig 4-1 Beam geometry for three point bending test

4.2.1.2 Bending Tests of Cantilever

Two beams were tested as cantilever beams, beam 1, and beam 2. Beam 2 has the same width and thickness as beam 1, but with a greater length of 300 mm. One end of the beams was clamped in the vice grips. The set-up is shown in Figure 4-2. The beams were slightly perturbed at the free end in the most flexible plane, i.e. oxz plane in Figure 4-3 (z is the axis pointing into the paper), in order to excite the first bending mode. A laser vibrometer, its control unit and a spectrum analyzer were used to measure and record the natural frequency of this mode. The Young's modulus was calculated by using equation (3). The two beams were tested in two ways depicted in Figure 4-2 a and Figure 4-2 b individually. One way was that end 1 was fixed and end 2 was free, while the other way was the opposite, end 1 was free and end 2 was fixed.

$$\omega = (\beta l)^2 \sqrt{\frac{EI}{\rho A l^4}}$$

$$E = \frac{\omega^2 \rho A l^4}{(\beta l)^4 I} \tag{3}$$

where E is the Young's modulus, in MPa. ω is the first natural frequency of the bending modes of the beam (rad/s) ; ρ the density of the beam (dimensionless); A the cross-sectional area of the beam (mm^2); I moment of inertia of the beam cross section about the z axis (mm^4); l the initial gauge length of the beam, (mm) ; βl , from which the value is obtained from knowledge of the boundary conditions. In this case, a standard Bernulli-Euler cantilever beam, $\beta l = 1.875104$ for the first bending mode of vibration (Rao, 2003).

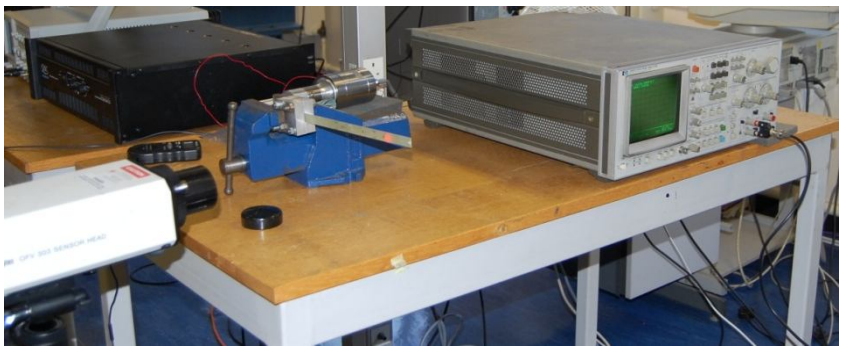

Fig 4-2 Cantilever test

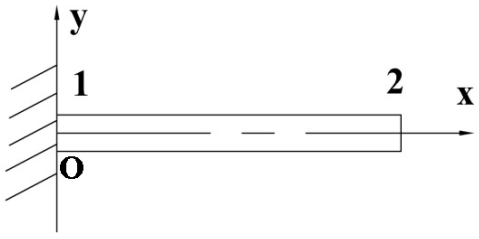

Fig 4-3 a Schematic of the cantilever beam

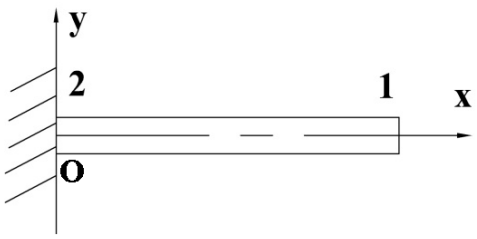

Fig 4-3 b Schematic of the cantilever beam the other way around

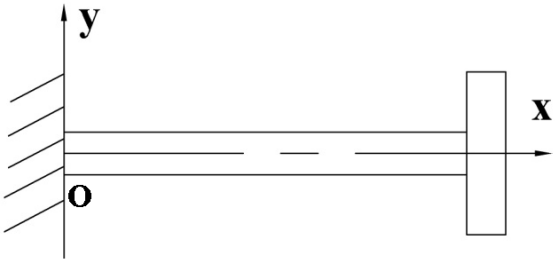

Fig 4-3 c Schematic of the cantilever beam with an end mass

4.2.1.3 Hammer Impact Test

Beam 1 was also tested as a cantilever with an end mass using the hammer impact test. The experiment was to find out the natural frequency of the first bending mode of the system. The experimental set-up and procedure are explained in Chapter 7 section 7.1. After the natural frequency was obtained, equation (3) was applied to get the Young's modulus but β was obtained through use of different boundary conditions; more details are given in **Appendix 1.**

4.2.2 Results and Discussions

1. The results from the three point bending tests are listed in Tables 4-2 and 4-3. This shows that the Young's modulus for beam 1, using the three point bending test, was found to be 22.51GPa when the support span was 100mm, 9.32% bigger than 20.59 GPa when the span was 50mm.
2. The results from the bending tests on the cantilever and the hammer impact tests are listed in Tables 4-4, 4-5 and 4-6. Table 4-4 shows that as for beam 2, when end 1 was fixed and end 2 was free the arithmetic average value of the Young's modulus was 18.26 GPa, while the other value was 16.16 GPa when end 2 was fixed and end 1 was free, 11.5% smaller than 18.26 GPa. For beam 1, as seen from Table 4-5, the Young's modulus for one configuration was 15.06 GPa and for the other was 13.19 GPa, which is 12.4% smaller than 15.06 GPa. The Young's modulus from the hammer impact test confirms that beam 1 has the smaller value of the Young's modulus, 13.19 GPa, as shown in Table 4-6.
3. There are a number of properties which could have affected the experimental results.
    - Random orientation of reinforcing fibres can give rise to off-axis loadings. These internal load paths can differ according to the experimental testing configuration.
    - The reinforcing fibres can be of different lengths, which can also affect the internal load paths and be configuration-dependent.
    - The compliance of the adhesive in multi-layered composite elements can also affect the values.

- Cracks, voids, impurities and misalignments, if there are some, can also contribute to the results.
- The testing gauge length can have influence on the results as well. The influence of the testing gauge length on the mechanical properties of composite materials has been widely discussed. (Jones 1999, Pardini *et al* 2002, Chivavibul and Enoki 2003) They all found that the Young's modulus had a dependency on the gauge length. One possible explanation is that the cracks, voids, impurities and fibrillar misalignments could give rise to a scatter in properties. Hence, the gauge region might not be uniformly stressed as it is supposed to be.

4. In the later experimental investigations into the effect of SMA strips on the above mentioned beams, the bending tests of cantilever will be utilized for the same orientation of the beam, with and without SMA strips bonded to it.

No.	F_{max} (N)	Δd @ F_{max}(mm)	E (GPa)	E_{aver}(GPa)
1	4.44	0.6	21.76	
2	5	0.65	23.1	
3	6.88	0.8	23.92	22.51
4	9.61	1.0	22.23	
5	12.96	1.25	21.53	

Table 4-2 Three points bending test on beam 1 when the support span is 100mm.

No.	F_{max} (N)	Δd @ F_{max}(mm)	E (GPa)	E_{aver}(GPa)
1	60	0.8838	20.25	
2	70	0.9714	20.3	
3	80	1.059	21.2	20.59
4	90	1.146	21.05	
5	100	1.239	20.16	

Table 4-3 Three points bending test on beam 1 when the support span is 50mm

l (mm)	f_{1a} (Hz)	f_{1b} (Hz)	E_a (GPa)	E_b (GPa)
150	47.5	46.6	16.87	16.23
180	33.0	32.4	16.88	16.27
200	27.6	26.4	18.00	16.47
220	23.4	21.2	18.94	15.55
250	18.9	16.8	20.60	16.28
E_{aver}(GPa)			18.26	16.16

Table 4-4 Cantilever beam bending test on beam 2

l (mm)	f_{1a} (Hz)	f_{1b} (Hz)	E_a (GPa)	E_b (GPa)
150	101	94.5	15.06	13.19

Table 4-5 Cantilever beam bending test on beam 1

Note: f_{1a}, f_{1b} are the first natural frequency of bending for the two systems shown in Table 4-2 a and Table 4-2 b respectively. E_a, E_b are the Young's modulus of the beam calculated from f_{1a} and f_{1b}.

l (mm)	End mass	f_1 (Hz)	E (GPa)
112	Made of steel, with width15mm, thickness 15mm and length 70mm	7.44	13.19

Table 4-6 Cantilever beam bending test with an end mass on beam 1

4.3 Shear Modulus

4.3.1 Introduction

The following experiment was designed to determine the modulus of rigidity. Utilising the test specimen with known geometry, this specimen could be twisted, with the values for torque simultaneously measured. To perform this task, a torsion testing machine was used. With the beam secured and clamped within the machine, one end of the specimen was twisted to certain angles, while the opposing end was kept straight by attaching it to the centre of an arm structure. This arm was held fixed throughout the procedure.

The ultimate goal, the determination of the modulus of rigidity, G, can be expressed by [Popov, 1978]

$$G = \frac{T\,L}{\varphi\,\beta\,wt^3} \tag{4}$$

Where T is the torque applied in N·m, L is the gauge length of the specimen in meter, φ is the total angle of twist in radians, β is the numerical factor for the twist of a shaft of rectangular cross-section. w and t are the width and thickness of the cross-sectional area of the beam respective in meter. T/φ is the slope of the linear portion of the curve when the torque is plotted against the angle of twist.

4.3.2 Equipment and Procedure

The MTS, 858 Mini Bionix®II material test system was used for this experiment. The system consisted of a loading unit with cross-head mounted actuator, a hydraulic power unit and a test controller channels (force and displacement). Two g-e beams made of the same width 13mm and thickness 2.2mm, but with different lengths of 300mm and 150mm, were used respectively. The specimen was secured in the torsion testing machine and set up vertically within two grips. The testing package, designed by MTS, was used to record, store and analyse the data. The apparatus was set to read zero degrees of twist and zero torque before the start of the test.

Fig 4-4 Specimen set-up

The twist rate was induced at 0.1 degree/second. The time between two adjacent recording points was 0.01s. The recording was done by continuous sampling. The twist started at zero degrees and ended at 15 degrees for the long beam of length 300mm, whilst for the short beam, the twist started at zero degrees and ended at 7 degrees. The selection of 15 and 7 degrees was from the engineering experience to avoid damage of the bond between the glass and the epoxy. After the twisting angle reached 15 or 7 degrees respectively, the beam was twisted back to zero degrees to see if any hysteresis effects had taken place.

4.3.3 Data Analysis and Calculations

A torque and twisting angle chart is given as shown in Figure 4-6, and based on the data for angles and torques at each increment for the long beam. The black dots are the data when the beam was twisted from zero degrees to 15 degrees whilst the pink dots are those when the beam was twisted back from 15 degrees to zero degrees. From the graph, the relationship between the torque and the twisting angle are linear for both cases, and therefore the twisting was entirely in the elastic deformation region. Two trend lines were plotted in Microsoft Excel for both cases. The slopes are approximately 0.7115 and 0.6993 respectively. The shear moduli were calculated by using equation (1) to give 4.11 GPa and 4.04 GPa. The average of these two values, 4.075 GPa is considered to be the shear modulus of the long beam.

	Long beam	Short beam
Width (mm)	13	13
Thickness (mm)	2.2	2.2
Length (mm)	300	150
Gauge length (mm)	240	100
β	0.3	0.3

Table 4-7 Lists measured and calculated dimensional data

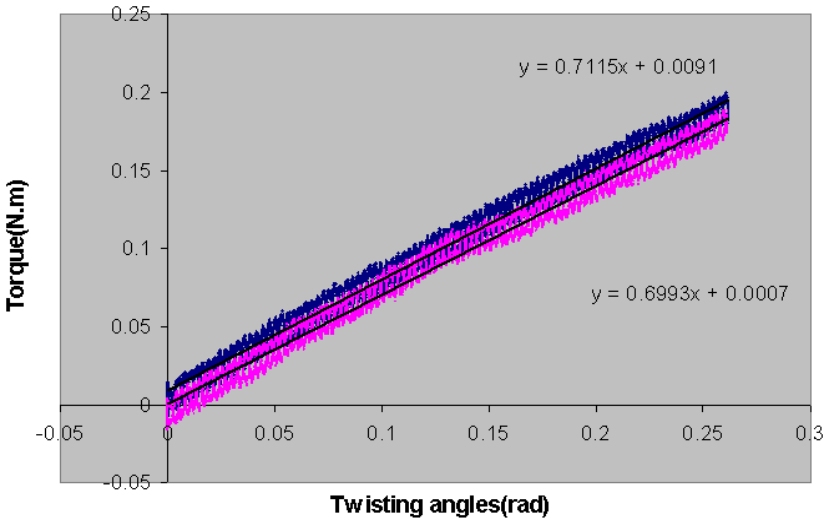

Fig 4-5 Torque against twisting angles for the long beam

The same analysis was undertaken for the short beam. The torque and twisting angle chart is shown in Figure 4-7. The black dots are the data when the beam was twisted from zero degrees to 7 degrees while the pink dots are those for the reverse twist. The shear moduli were calculated in this case as 2.79 GPa and 3.78 GPa. The average value, 3.285 GPa, is considered to be the shear modulus of the short beam.

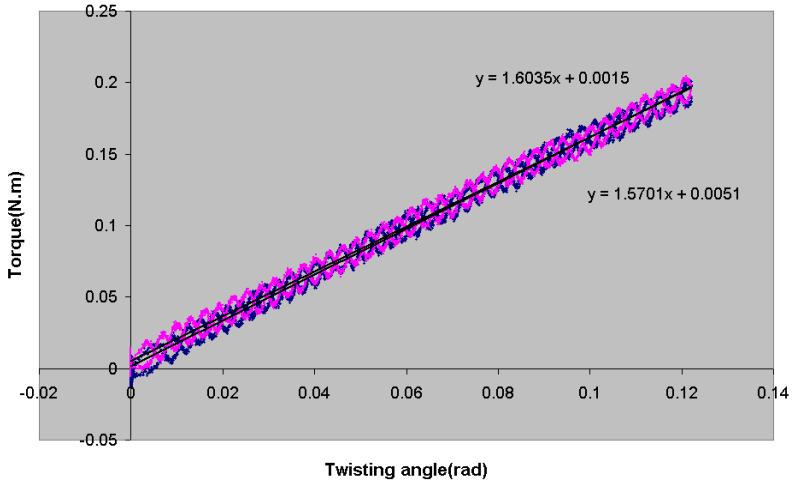

Fig 4-6 Torque against twisting angles for the short beam

4.3.4 Results and Discussions

The results found for the long and short beam from this experiment are different. The shear modulus for the short beam is 3.285 GPa, 19.39% smaller than that for the long beam, at 4.075 GPa. The reasons for this might come from three aspects: one is within the testing

apparatus. As noted in the experiment, even with the bottom and top grips tightened on the specimen, there was inevitably still some relative movement between the grips and specimen. The effect of the clamps on the short beam was bigger than that on the long beam, as a bigger torque occured on the short beam for the same total twisting angle. Another possible one is that it is more difficult to set the long beam completely straight compared to the short one. The properties of the beams themselves, like impurities, misalignment and bondage between the fibres and the matrix, could also contribute to the difference.

Chapter 5

Effects of SMA on the Properties of a Composite Cantilever Beam System with Two Centrally-bonded SMA Strips

5.1 Introduction

SMA components, in the form of wires, strips, etc. can be used to improve, or control, various dynamic characteristics of structural elements. For example, natural frequencies, modes of vibrations, damping ratios. SMA components are mostly utilised in two different ways (Baz *et al* 1995, Zak *et al* 2004). One way is the use of the Active Property Tuning (APT) technique. This technique is based on the changes in the Young's modulus, or the stiffness of SMA over the phase transformation. Another is a technique called Active Strain Energy Tuning (ASET) method. In this case, the SMA components are placed in a residual strain state, which can generate large internal forces during their activation as well as changes in their stiffness. In this chapter, the dynamic responses of a centrally-bonded composite beam with an end mass, presented in Figure 5-1, are studied in theory with application of the APT and ASET methods. The composite beam structure was composed of two thin SMA strips, attached to a flexible g-e beam on both sides centrally and symmetrically from one end through to the other end, and a lumped end-mass, which was fixed on the free end of the beam and the other end was clamped. In the case of the APT method, the properties of the composite beam structure and the results for the natural frequencies are summarised. The influences of such factors like: the width and thickness of the SMA strips, the Young's modulus of the strips are considered. When the ASET method is investigated, a simple theoretical model is introduced to estimate the natural frequencies and vibration modes when the SMA are activated and unactivated. In the model, the recovery force is modelled as an axial force acting on the beam, and the equation of motion of the free lateral vibration of the beam system is derived. Combining the boundary conditions of the composite beam system and its free vibration equation results in the natural frequency expressions of the bending modes of the system. The standard Euler mode shapes in conjunction with the orthogonality equation gives the mode shape functions for the composite beam system. Both the natural frequencies and modes are functions of the recovery force and the

stiffness of the composite beams. The variation of the recovery force and stiffness of the composite beam on the variation of the natural frequencies and the mode shape functions are described. The composite beam system is assumed to satisfy the following conditions: (1) The beam is a Euler-Bernoulli beam; (2) The beam has a constant mass per unit length m; (3) The beam has a constant flexural rigidity about y-axis, EI_y, when the SMA strips are at certain temperatures; (4) The large recovery forces generated in the pre-strained SMA wires are considered as fixed value when the SMA strips are at certain temperatures; (5) The forces, generated by thermal expansion of the SMA strips and the g-e beam, are neglected.

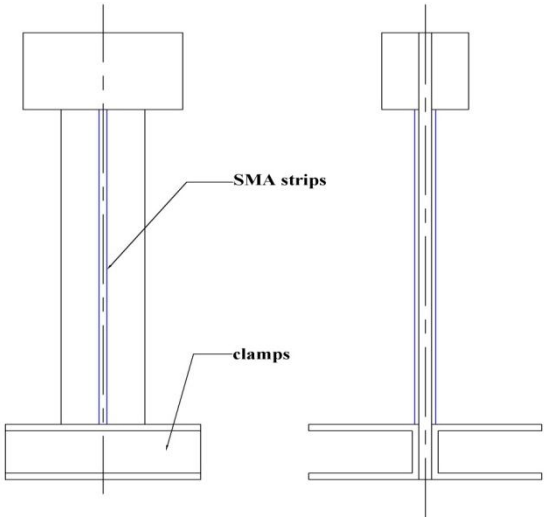

Fig 5-1 A flexible beam system with two externally attached SMA strips

5.2 Application of APT Method

5.2.1 Theoretical Approach to Determination of the Natural Frequency

To get the frequencies of the bending modes, the flexural rigidity EI_y, the cross-sectional area and the density of the composite beam need to be obtained. The system shown in Figure 5-1 can be modelled as a sandwich beam, in which two SMA strips enclose a glass epoxy core, as shown in Figure 5-2.

To determine the flexural rigidity of the composite beam, the following approach is adopted. It begins with the calculation of the moment of inertia of the cross-sectional area of the strip 1 about the y-axis, denoted as I_{y1}. By applying the parallel-axis theorem, I_{y1} is derived as

$$I_{y1} = \frac{w_{s1} t_{s1}^{\ 3}}{12} + w_{s1} t_{s1} (\frac{t_b + t_{s1}}{2})^2 \tag{1}$$

The moment of inertia of the cross-sectional area of the strip 2 about the y-axis I_{y2} :

$$I_{y2} = \frac{w_{s2} t_{s2}^{\ 3}}{12} + w_{s2} t_{s2} (\frac{t_b + t_{s2}}{2})^2 \tag{2}$$

The moment of inertia I_{yb} of the glass epoxy core about the y-axis is

$$I_{yb} = \frac{w_b}{12} t_b^{\ 3} \tag{3}$$

The flexural rigidity of the composite beam is given by

$$EI_y = E_{s1} I_{y1} + E_{s2} I_{y2} + E_b I_{yb} \tag{4}$$

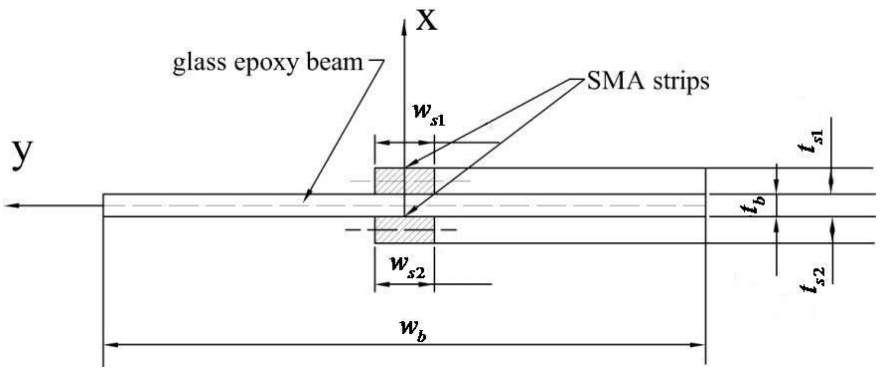

Fig 5-2 Cross-section of the composite beam

Then, in order to determine the density of the composite beam, the following is used

$$\rho = \frac{m}{V} = \frac{(\rho_{s1} V_{s1} + \rho_{s2} V_{s2} + \rho V_b)}{V_{s1} + V_{s2} + V_b} \tag{5}$$

Then, to determine the cross-section area of the composite beam, the area calculation is required

$$A = A_{s1} + A_{s2} + A_b = w_{s1} t_{s1} + w_{s2} t_{s2} + w_b t_b \tag{6}$$

where the subscrips $s1$, $s2$ and b refer to strips 1, 2, and the g-e beam respectively. t, w, V, E and ρ denote the thickness, width, volume, Young's modulus and density of the strips and the beam.

Finally, to determine the natural frequencies of the bending modes of the composite beam, the following theory is used

$$\omega = (\frac{\beta}{l})^2 * \sqrt{\frac{EI_y}{\rho A}}) \tag{7}$$

The value of β can be determined from the boundary conditions of the beam, see **Appendix 1** for details.

5.2.2 Results and Discussions

It is assumed that the composite beam system under consideration has certain mechanical properties, presented in Table 5-1.

		Young's modulus (GPa)	Density (kg/m^3)	Width (mm)	Thickness (mm)	Length (mm)
SMA	Martensite	26.3	6448.1	2	0.5	300
	Austenite	67				
End mass			2700	15	15	45
Beam		25	1865	13	2.2	300

Table 5-1 Properties of the composite beam system

Results of the natural frequencies under consideration are presented in Figures 5-3 and 4, 5 and 6 and Tables 5-2 to 5-7. In Figures 5-3 to 5-8, it is clearly shown that with certain width and thickness of the SMA strips, the natural frequencies of the composite beam increase when the SMA strips are activated. The increase is caused by the increase of the stiffness of the SMA strips, thus increasing the stiffness of the composite beam. These figures also show that the natural frequencies increase with increase of the thickness, with increase of the width of the SMA strips. This happening is due to the increase of the flexural rigidity of the composite beam when the thickness and width are increased. In Tables 5-4 to 5-7, when the

width is kept constant as 2 mm, the thickness of the SMA strips is increased by 40% from 0.5 mm to 0.7 mm, then from 0.7 mm to 0.98 mm, then to 1.372 mm finally as shown in the first and second columns in each table. Consequently the increments of the natural frequencies are listed in the fourth column. The last four columns contain the results of the case when the thickness is kept constant as 0.5 mm, the width is increased one after other. The increments of the natural frequencies are listed in the eighth column. It is found that changes of the natural frequencies are more sensitive to the changes of the thickness than width. For example, in Table 5-4, f_1 is increased from 5.636 Hz to 6.033 Hz by 7.04% when the thickness is increased from 0.5 mm to 0.7 mm by 40%, whilst f_1 is only increased by 4.36% from 5.636 Hz to 5.882 Hz when the width is increased by 40% from 2 mm to 2.8 mm. This phenomena is understandable because the thickness cubically changes the moment of inertia of the cross-sectional area of the strips about the y-axis, whilst the width does it linearly, seen from equations (1) and (2).

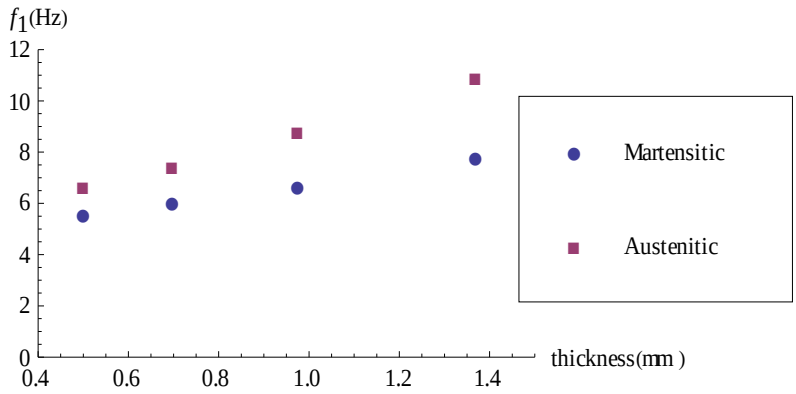

Fig 5-3 Influence of the thickness of SMA strips on natural frequencies of the 1st bending mode (width=2mm)

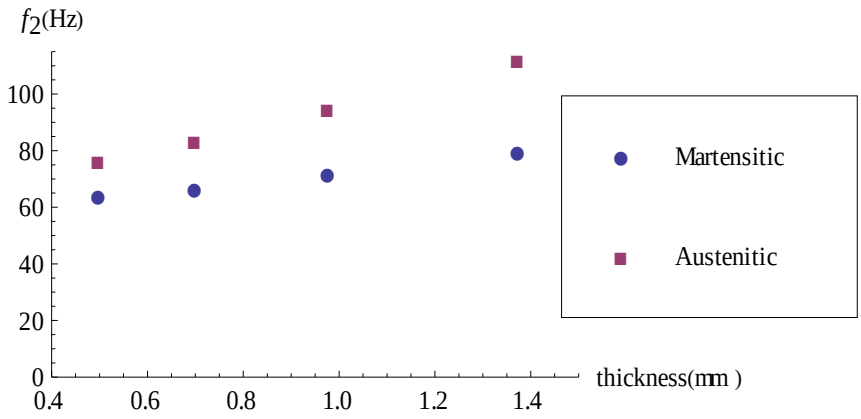

Fig 5-4 Influence of the thickness of SMA strips on natural frequencies of the 2nd bending mode (width=2mm)

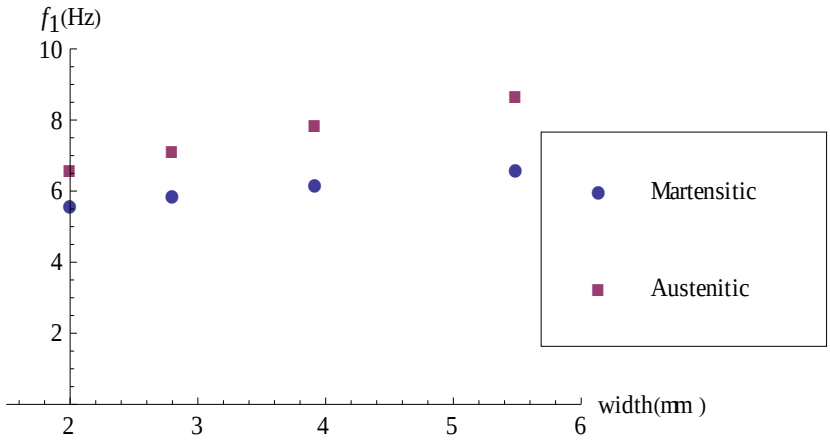

Fig 5-5 Influence of the width of SMA strips on natural frequencies of the 1st bending mode (thickness=0.5mm)

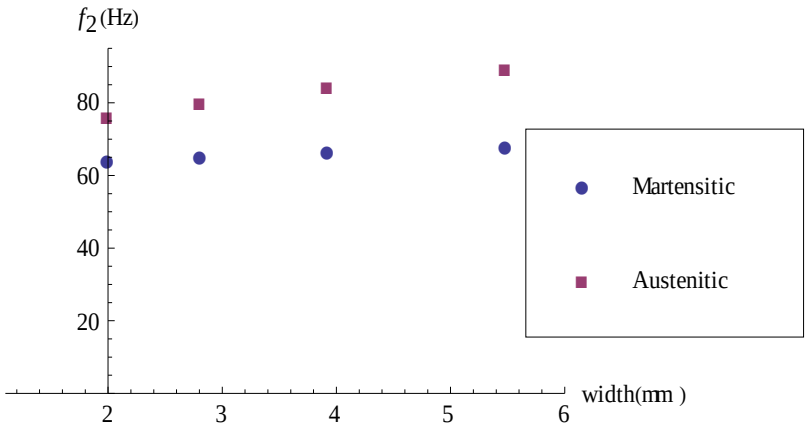

Fig 5-6 Influence of the width of SMA strips on natural frequencies of the 2nd bending mode (thickness=0.5mm)

$t_{s1} = t_{s2}$ (mm)	f_1 (Hz)		f_2 (Hz)	
	Unactivated SMA	Activated SMA	Unactivated SMA	Activated SMA
0.5	5.636	6.643	64.551	76.088
0.7	6.033	7.504	67.140	83.518
0.98	6.692	8.845	71.836	94.941
1.372	7.794	10.937	80.053	112.332

Table 5-2 Influence of the thickness of SMA strips and the SMA activation on natural frequencies of the 1st and 2nd bending mode (width=2mm)

$w_{s1} = w_{s2}$ (mm)	f_1 (Hz)		f_2 (Hz)	
	Unactivated SMA	Activated SMA	Unactivated SMA	Activated SMA
2	5.636	6.643	64.551	76.088
2.8	5.882	7.192	65.457	80.042
3.92	6.201	7.879	66.561	84.579
5.488	6.608	8.723	67.867	89.590

Table 5-3 Influence of the width of SMA strips and the SMA activation on natural frequencies of the 1st and 2nd bending mode (thickness=0.5mm)

$t_{s1} = t_{s2}$ (mm)	Thickness increased by (%)	f_1 (Hz)	f_1 increased by (%)	$w_{s1} = w_{s2}$ (mm)	Width increased by (%)	f_1 (Hz)	f_1 increased by (%)
0.5		5.636		2		5.636	
0.7	40	6.033	7.04	2.8	40	5.882	4.36
0.98	40	6.692	10.92	3.92	40	6.201	5.42
1.372	40	7.794	16.47	5.488	40	6.608	6.56

Table 5-4 Comparison of the influence of the thickness and the width of SMA strips on natural frequencies of the 1st bending mode when the strips are not activated

$t_{s1} = t_{s2}$ (mm)	Thickness increased by (%)	f_1 (Hz)	f_1 increased by (%)	$w_{s1} = w_{s2}$ (mm)	Width increased by (%)	f_1 (Hz)	f_1 increased by (%)
0.5		6.643		2		6.643	
0.7	40	7.504	12.96	2.8	40	7.192	8.26
0.98	40	8.845	17.87	3.92	40	7.879	9.55
1.372	40	10.937	23.65	5.488	40	8.723	10.71

Table 5-5 Comparison of the influence of the thickness and the width of SMA strips on natural frequencies of the 1st bending mode when the strips are activated

$t_{s1} = t_{s2}$ (mm)	Thickness increased by (%)	f_2 (Hz)	f_2 increased by (%)	$w_{s1} = w_{s2}$ (mm)	Width increased by (%)	f_2 (Hz)	f_2 increased by (%)
0.5		64.551		2		64.551	
0.7	40	67.140	4.01	2.8	40	65.457	1.40
0.98	40	71.836	6.99	3.92	40	66.561	1.69
1.372	40	80.053	11.44	5.488	40	67.867	1.96

Table 5-6 Comparison of the influence of the thickness and the width of SMA strips on natural frequencies of the 2nd bending mode when the strips are not activated

$t_{s1} = t_{s2}$ (mm)	Thickness increased by (%)	f_2 (Hz)	f_2 increased by (%)	$w_{s1} = w_{s2}$ (mm)	Width increased by (%)	f_2 (Hz)	f_2 increased by (%)
0.5		76.088		2		76.088	
0.7	40	83.518	9.77	2.8	40	80.042	5.20
0.98	40	94.941	13.68	3.92	40	84.579	5.67
1.372	40	112.332	18.32	5.488	40	89.590	5.92

Table 5-7 Comparison of the influence of the thickness and the width of SMA strips on natural frequencies of the 2nd bending mode when the strips are activated

5.3 Application of ASET Method

5.3.1 Natural Frequencies of the Bending Modes

5.3.1.1 Expressions of the Natural Frequencies of the Bending Modes

The beam is subjected to an axial compressive force of $2F_a$. By considering the free-body of an element dz of the beam in lateral vibration shown in Figure 5-7, then if $V =$ shear force, $M =$ bending moment, then $\theta = \partial u / \partial z =$ slope and the deflection is $u = u(z,t)$. From Newton's second law, the dynamic force equation for vertical motion is,

$$m\frac{\partial^2 u}{\partial t^2}dz = -(V+dV)+V-(2F_a+\frac{\partial(2F_a)}{\partial z})dz\sin(\theta+\frac{\partial\theta}{\partial z})+2F_a\sin\theta \tag{8}$$

Algebraically manipulating the above equation, neglecting the term $\frac{\partial(2F_a)}{\partial z})dz\sin(\theta+\frac{\partial\theta}{\partial z})$, and cancelling the term dz on both sides leads to,

$$m\frac{\partial^2 u}{\partial t^2} = -\frac{\partial V}{\partial z} - 2F_a\frac{\partial^2 u}{\partial z^2} \tag{9}$$

and for rotational motion about the point O, the left end of the element shown in Figure 5-7,

$$M-(M+dM)+(V+dV)dz = 0 \tag{10}$$

or $$V = \frac{\partial M}{\partial z} \tag{11}$$

From elementary strength of materials the beam curvature and the moment M are related by,

$$M = EI_y\frac{\partial^2 u}{\partial z^2} \tag{12}$$

where EI_y is the flexural stiffness of the beam. Combining equations (9), (11) and (12) gives the beam equation for lateral vibration subjected to the compressive force $2F_a$.

$$EI_y\frac{\partial^4 u}{\partial z^4} + m\frac{\partial^2 u}{\partial t^2} + 2F_a\frac{\partial^2 u}{\partial z^2} = 0 \tag{13}$$

The solution of equation (13) can be obtained using the method of separation of variables as

$$u(z,t) = f(z)(A\cos\omega t + B\sin\omega t) \tag{14}$$

where ω is the natural frequency, A and B are constants, and $f(z)$ is an eigenfunction, which describes the mode shape of the beam at the frequency ω.

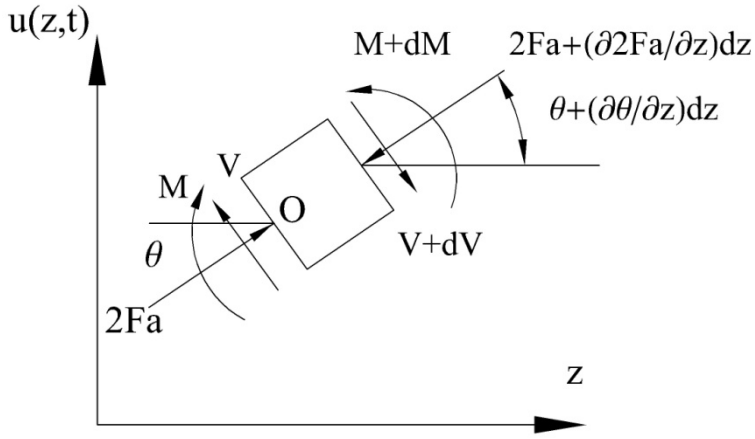

Fig 5-7 Lateral vibration of beam with axial compression

Substitution of equation (14) into equation (13) gives

$$EI_y f'''' - m\omega^2 f + 2F_a f'' = 0 \tag{15}$$

The prime denotes differentiation with respect to z.

By assuming the solution $f(z)$ to be

$$f(z) = Ce^{sz} \tag{16}$$

where C and s are constants then substitution of equation (16) into equation (15) shows the corresponding characteristic equation, which is,

$$s^4 + \frac{2F_a}{EI_y}s^2 - \frac{m\omega^2}{EI_y} = 0 \tag{17}$$

The quadratic roots of equation (17) are

$$s_1^2, s_2^2 = -\frac{F_a}{EI_y} \pm \left(\frac{F_a^{\,2}}{E^2 I_y^2} + \frac{m\omega^2}{EI_y}\right)^{1/2} \tag{18}$$

which must be real.

Letting $\lambda_1^2 = s_1^2 = (\frac{F_a^{\ 2}}{E^2 I_y^2} + \frac{m\omega^2}{EI_y})^{1/2} - \frac{F_a}{EI_y}$, and $\lambda_2^2 = -s_2^2 = (\frac{F_a^{\ 2}}{E^2 I_y^2} + \frac{m\omega^2}{EI_y})^{1/2} + \frac{F_a}{EI_y}$, or $s_2 = \pm i\sqrt{(\frac{F_a^{\ 2}}{E^2 I_y^2} + \frac{m\omega^2}{EI_y})^{1/2} + \frac{F_a}{EI_y}}$, where $i = \sqrt{-1}$. Hence the solution of equation (15) can be expressed as

$$f(z) = C_1 \cosh \lambda_1 z + C_2 \sinh \lambda_1 z + C_3 \cos \lambda_2 z + C_4 \sin \lambda_2 z \tag{19}$$

The boundary conditions at the fixed end are $f(0) = f'(0) = 0$, so substitution of these conditions into equation (19) leads to,

$$f(z) = C_1(\cosh \lambda_1 z - \cos \lambda_2 z) + C_2(\sinh \lambda_1 z - \frac{\lambda_1}{\lambda_2} \sin \lambda_2 z) \tag{20}$$

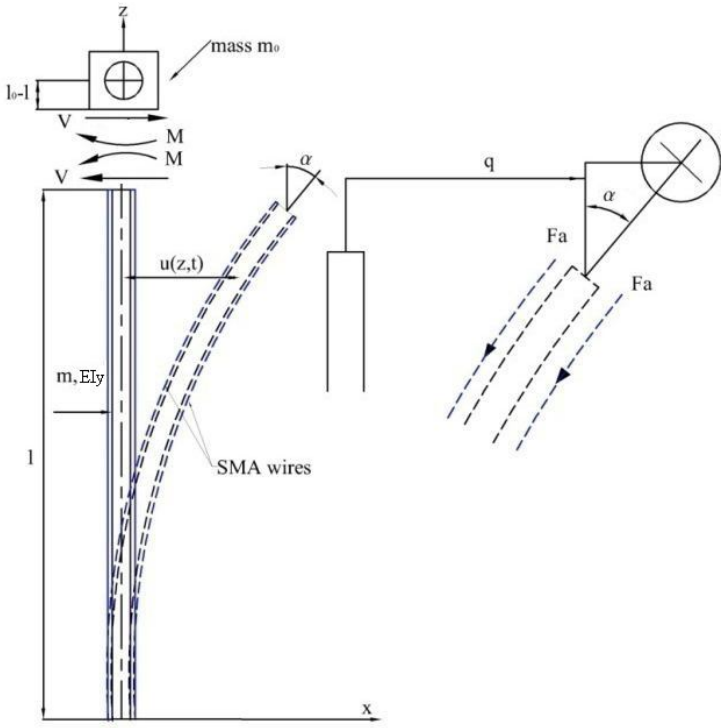

Fig 5-8 Force analysis on the end mass (adapted from Forehand and Cartmell (2001))

5.3.1.2 Boundary Conditions at the Free End

The sum of forces along the x direction being zero leads to

$$V_N = m_0(\ddot{u}(l,t) + (l_0 - l)\ddot{\alpha}) \tag{21}$$

where V_N is the force that the beam end transfers to the end mass and it is given by

$$V_N = V\cos\alpha + 2F_a\sin\alpha = V + 2F_a\alpha \tag{22}$$

where V is the shear force at the top of the beam, α is the angle between the tangent line to the beam at the top of the beam and positive z-axis. It's worthwhile to mention the assumption again that a small displacement u is considered in this case. That means α is very small, therefore

$$\frac{\partial u(z,t)}{\partial z}\Big|_{z=l} = \tan\alpha = \alpha \quad \sin\alpha = \alpha \text{ and } \cos\alpha = 1 \tag{23}$$

Substituting equation (22) and (23) into equation (21) and rewriting it gives

$$V + 2F_a\alpha = m_0(\ddot{u}(l,t) + (l_0 - l)\ddot{\alpha}) \tag{24}$$

The rotation movement of the end mass is represented as

$$I_G\ddot{\alpha} = M - V(l_0 - l) \tag{25}$$

where I_G is the moment of inertia of the end mass about an axis through its centre, parallel to the y-axis. M is the bending moment at the free-end point of the beam.

The shear force V and bending moment M can be expressed as normal in terms of the spatial derivatives of u, as follows:

$$V = EI_y\frac{\partial^3 u(z,t)}{\partial z^3}\Big|_{z=l} \qquad M = -EI_y\frac{\partial^2 u(z,t)}{\partial z^2}\Big|_{z=l} \tag{26}$$

Substituting equation (26) into equations (24) and (25) yields

$$EI_y u''' + 2F_a u' = m_0(\ddot{u}(l,t) + (l_0 - l)\ddot{u}') \text{ at } z = l \tag{27}$$

$$I_G\ddot{u}' = -EI_y(u'' + u'''(l_0 - l)) \text{ at } z = l \tag{28}$$

By using equation (14), equations (27) and (28) become, respectively,

$$EI_y f'''(l) + 2F_a f'(l) + \omega^2 m_0(f(l) + (l_0 - l)f'(l)) = 0 \tag{29}$$

$$-\omega^2 I_G f'(l) + EI_y (f''(l) + (l_0 - l) f'''(l)) = 0 \tag{30}$$

By substituting equation (20) and its spatial derivatives into equations (29) and (30) two new equations are obtained which can be used to find the ratio of C_2 to C_1 and to find the frequency equations. The natural frequencies of the beam system can be numerically solved for different values of the force F_a . The process is explained in **Appendix 5** by using a specific example.

It is now to be determined whether or not the mode shape functions obtained from the above procedure are orthogonal.

5.3.1.3 Orthogonality of the Bending Modes

As derived above, the eigenvalue equation corresponding to this beam for free vibration is equation (15). For clarification, it is rewritten here as

$$EI_y f'''' - m\omega^2 f + 2F_a f'' = 0 \tag{15}$$

To derive the orthogonality relations for the beam, consider two eigenvalues ω_i^2 and ω_j^2 and the corresponding normal functions $f_i(z)$ and $f_j(z)$, respectively, so that

$$EI_y f_i'''' - m\omega_i^2 f_i + 2F_a f_i'' = 0 \tag{31}$$

and

$$EI_y f_j'''' - m\omega_j^2 f_j + 2F_a f_j'' = 0 \tag{32}$$

Multiplying equation (31) by $f_j(z)$ and equation (32) by $f_i(z)$, integrating them both by parts twice over the length of the beam and using the boundary conditions at the fixed end of the beam ($f_i(0) = f_i'(0) = f_j(0) = f_j'(0) = 0$), and finally subtracting them gives,

$$\begin{aligned}(\omega_j^2 - \omega_i^2)\int_0^l m f_i(z) f_j(z) dz = {} & f_i(l) EI_y f_j'''(l) - f_i'(l) EI_y f_j''(l) \\ & - f_j(l) EI_y f_i'''(l) + f_j'(l) EI_y f_i''(l) \\ & + 2F_a f_j'(l) f_i(l) - 2F_a f_i'(l) f_j(l)\end{aligned} \tag{33}$$

From equations (29) and (30) the term $f''(l)$ can be expressed in terms of $f(l)$ and $f'(l)$ as follows

$$EI_y f''(l) = \omega^2 (m_0 (l_0 - l)(f(l) + (l_0 - l) f'(l)) + I_G f'(l)) + 2F_a (l_0 - l) f'(l) \tag{34}$$

Then, rearranging equations (30) and (34) and substituting them into equation (33) and further manipulation yields,

$$(\omega_j^2 - \omega_i^2) \left\{ \int_0^l m f_i(z) f_j(z) dz + \begin{bmatrix} m_0 (f_i(l) + (l_0 - l) f_i'(l))(f_j(l) \\ + (l_0 - l) f_j'(l)) + I_G f_i'(l) f_j'(l) \end{bmatrix} \right\} = 0 \tag{35}$$

Finally, using the fact $\omega_i \neq \omega_j$ gives

$$\left\{ \int_0^l m f_i(z) f_j(z) dz + \begin{bmatrix} m_0 (f_i(l) + (l_0 - l) f_i'(l))(f_j(l) \\ + (l_0 - l) f_j'(l)) + I_G f_i'(l) f_j'(l) \end{bmatrix} \right\} = 0 \tag{36}$$

Therefore, the mode shapes are orthogonal in the sense expressed as equation (36) though it does not look exactly like the usual solution for orthogonality because of the explicit presence of mass m_0 and I_G.

Furthermore, these mode shapes can be normalized so that

$$\int_0^l m f_i^2(z) dz + \left[m_0 (f_i(l) + (l_0 - l) f_i'(l))^2 + I_G (f_i'(l))^2 \right] = m_0 \quad i = 1, 2, \cdots \tag{37}$$

With this normalization the mode shapes are non-dimensional.

5.3.1.4 Mode Shape Functions of the Bending Modes

Substituting the boundary conditions at the fixed end, ie. $f(0) = f'(0) = 0$ and at the free end, expressed as equations (26) and (27), into the standard Euler-Bernulli beam mode shape function, expressed as equation (20), yields the ratio of C_2 to C_1 for certain magnitude of force F_a. Finally, using the orthogonality property of the mode shapes, in the form of equation (37) , gives the mode shape functions. One example is taken to describe the details in **Appendix 5** and the results are shown in the last part of this section.

5.3.1.5 Results and Discussions

The SMA strips have two effects on the beam system during their activation. They generate recovery force and also increase the beam's stiffness. In order to see the effect of the recovery force only, the stiffness is theoretically kept constant. Based on this assumption, a specific beam system is taken as an example. Its properties are listed in Table 5-1. Table 5-8 shows the effect of force F_a on the different parameters of the beam system.

F_a (N)	f_1 (Hz)	λ_1 (m^{-1})	λ_2 (m^{-1})	$\lvert C_1 \rvert$	C_2/C_1	f_2 (Hz)	λ_1 (m^{-1})	λ_2 (m^{-1})	$\lvert C_1 \rvert$	C_2/C_1
0	5.636	3.832	3.832	1.028	-0.902	64.551	12.967	12.967	1.139	-1.006
1	5.054	3.290	4.002	1.084	-0.876	63.742	12.786	12.987	1.147	-1.006
2	4.391	2.715	4.213	1.113	-0.833	62.923	12.602	13.007	1.154	-1.007
3	3.601	2.099	4.469	1.099	-0.755	62.092	12.416	13.028	1.162	-1.007
4	2.569	1.404	4.768	1.036	-0.601	61.250	12.228	13.049	1.170	-1.008
4.5	1.843	0.974	4.930	0.989	-0.457	60.825	12.133	13.060	1.173	-1.008
5.028	0.0135	0.004	5.108	0.932	-0.002	60.372	12.032	13.071	1.178	-1.008

Table 5-8 Influence of F_a on the natural frequencies and mode shape coefficients

Figures 5-9 and 5-10 show the variation in the natural frequencies of the first and second bending modes with variation in the magnitude of force F_a. This indicates the decreasing nature of the natural frequencies as F_a increased, and shows the end load at which the beam buckles is 5.028 N when the length of the beam is 0.3 m. This is compared by the static critical load for the lateral buckling.

The critical Euler buckling load for a cantilever beam is given by

$$P_{cr} = \frac{\pi^2 EI_y}{4l^2} \tag{38}$$

To avoid static buckling, the following condition must be satisfied

$$(2F_a \cos\alpha + m_0 g) \approx (2F_a + m_0 g) \leq \frac{\pi^2 EI_y}{4l^2} \tag{39}$$

Therefore, in this example depicted in Table 5-1,

$$F_a \le \frac{\pi^2 EI_y}{8l^2} - \frac{m_0 g}{2} \le 5.282 - 0.134 = 5.148\ N$$

This shows that the beam will buckle slightly more readily under dynamic loading than under static loading, as noted, the critical load under dynamic loading is a little less than that for static loading.

The mode shapes under the effect of the force F_a are depicted in Figures 5-11 and 5-12. In order to see the to see the effect clearly, some parts of the two figures are zoomed in. It can seen that force F_a reduces the excursion of the first and second bending modes.

The force F_a can only affect the natural frequencies and the mode shapes up to the beam's dynamic buckling.

In practice, during the activation, the SMA strips not just generate internal forces as discussed above, they increase the stiffness of the composite beam too. This is because the Young's modulus of the SMA strips increases, and therefore increases the Young's modulus of the composite beam too. The increase of the stiffness increase the natural frequencies of the bending modes as well. These two effects both need to be analyzed carefully.

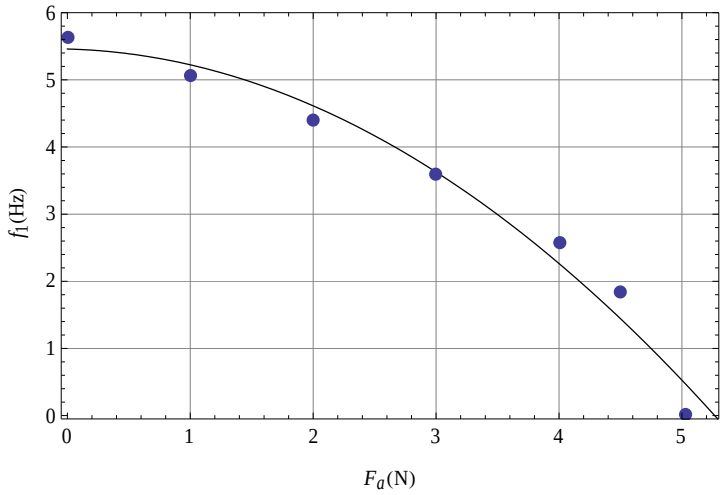

Fig 5-9 Natural frequency of the 1st bending mode against the recovery force

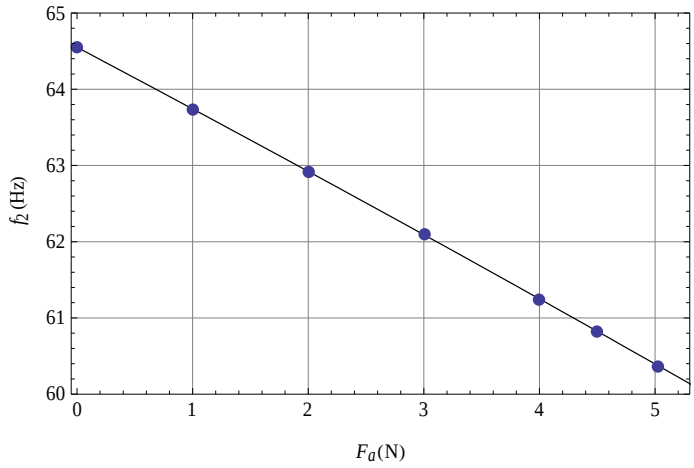

Fig 5-10 Natural frequency of the 2nd bending mode against the recovery force

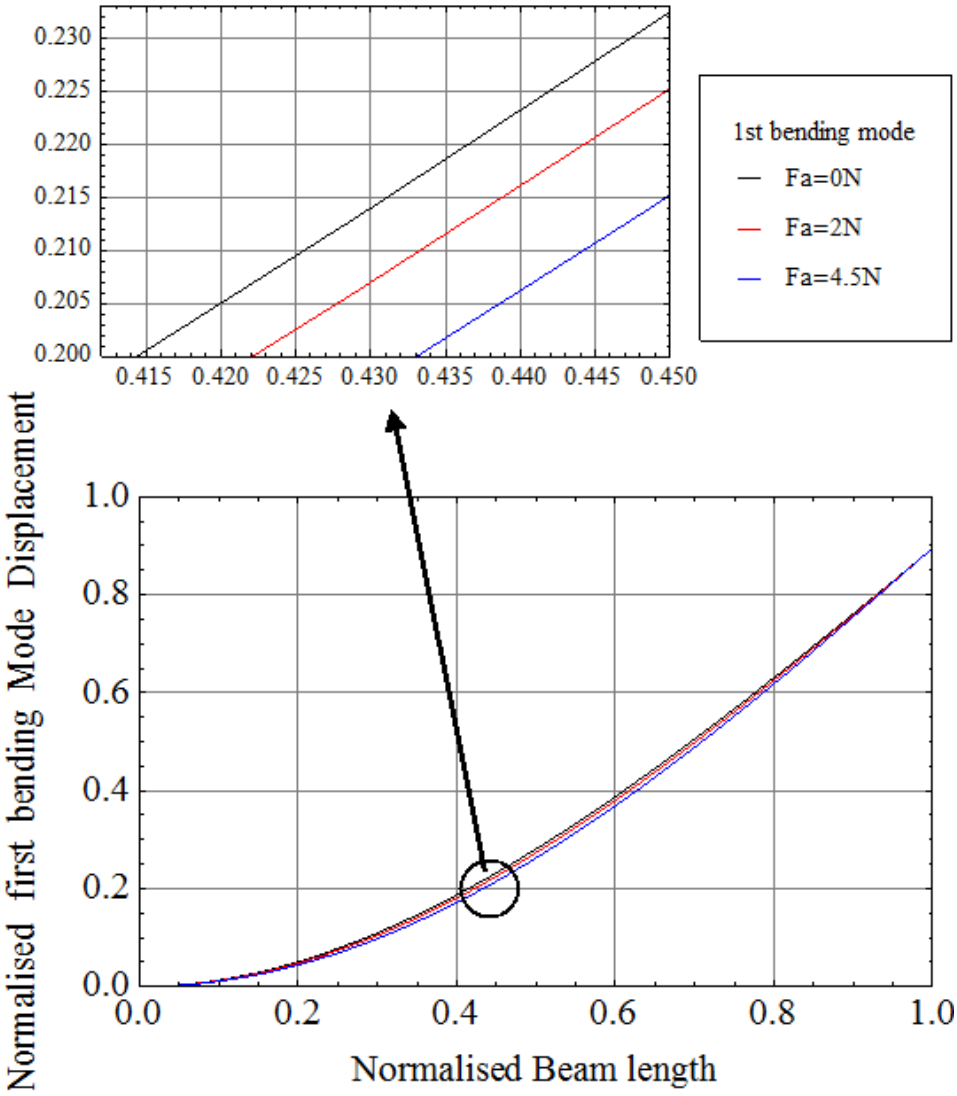

Fig 5-11 Shape of the normalised first bending mode against the recovery force F_a, over normalised beam length l

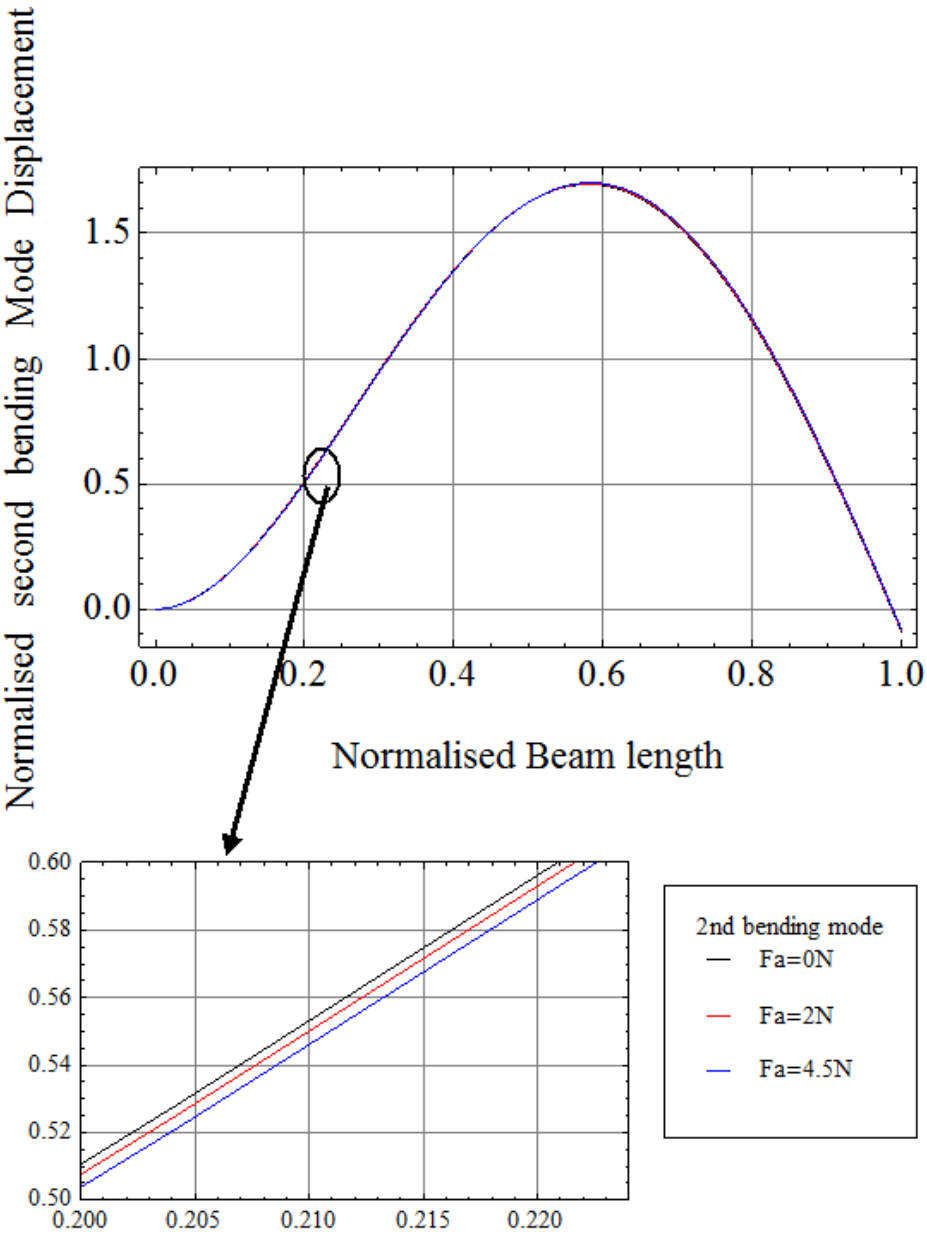

Fig 5-12 Shape of the normalised second bending mode against the recovery force F_a, over normalised beam length l

Chapter 6

A Composite Cantilever Beam Structure with Two Centrally-Bonded SMA Strips under Parametric Vibration

This chapter investigates the effect of pre-strained SMA strips on the instability zones of the system discussed in Chapter 5 when it undergoes a parametric excitation, as shown in Figure 6-1. As the SMA strips are very thin and narrow and do not change the geometry of the beam significantly, it is therefore assumed that the structure is such that the kinematic relationships for combined bending and torsional motions derived by Cartmell (1990) and Forehand and Cartmell (2001), and also, from these kinematic relationship, the three non-linear modal equations of motions, equations (9) to (11) in Chapter 3 by recourse to the Lagrangian formulation, can be applicable to this problem. To incorporate the two strips into the model, the generalised forces corresponding to the generalised coordinates u_1, u_2 and ϕ_1 need to be derived in terms of the SMA recovery force, these being introduced into the model by SMA phase transformation. Modal coordinates u_1, u_2 and ϕ_1 correspond to the fundamental and second bending modes and the fundamental torsion mode. An analysis for the derivation of expressions for the recovery force as a function of generalised coordinates u_1, u_2 and ϕ_1 is presented in this chapter. Further study shows that the increase of the magnitude of the recovery force results in the increase of the instability region.

6.1 Generalised Forces

The recovery forces are considered as fixed values and act at the end of the cantilever beam. When the beam is subjected to combined bending and torsion, the force directions are changed in three-dimensional space. This change is a function of the displacements $u(l)$, $v(l)$ and $w(l)$ of the end point of the beam along the three axes x, y and z. The physical displacements u, v and w can be expressed by the generalised coordinates u_1, u_2 and ϕ_1 with the help of the kinematic analysis within the system. Finally a generalised force is obtained in such a manner that the work done by this generalised force equals the work

done by all forces when its corresponding generalised coordinate varies infinitesimally and the other generalised coordinates are kept constant.

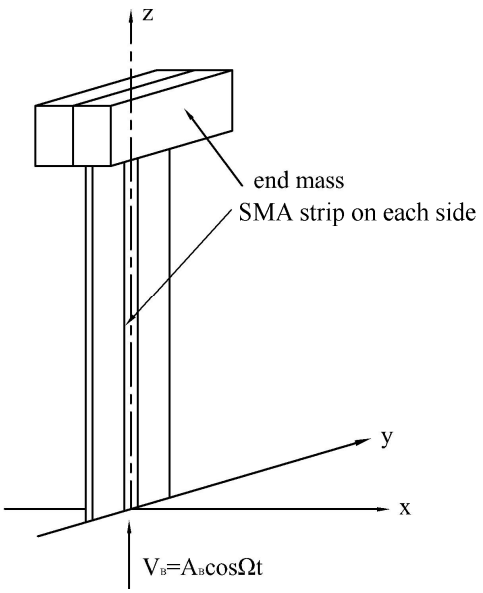

Fig 6-1 A composite beam system under a vertical excitation

6.1.1 Components of the Recovery Force

In order to get the expressions of the generalised forces, the kinematic relationships derived by Cartmell (1990) are recalled here. Cartmell started with an element of a rectangular section beam. In its undeformed state, the element is referred to a three-dimensional frame, Oxyz, which is completely fixed in space, as shown in Figure 6-2. In a similar manner the deformed element, after combined bending and torsion, is defined in another frame, OXYZ. Unit vectors $\bar{i}\ \bar{j}\ \bar{k}$ are associated with the frame Oxyz and $\bar{I}\ \bar{J}\ \bar{K}$ are associated with OXYZ. The transformation matrix from Oxyz to OXYZ is

$$M=\begin{bmatrix}(\cos\phi\cos\alpha-\sin\phi\sin\beta\sin\alpha) & (-\cos\phi\cos\alpha-\cos\phi\sin\beta\sin\alpha) & (\cos\beta\sin\alpha)\\ \sin\phi\cos\beta & \cos\phi\cos\beta & \sin\beta\\ (-\cos\phi\sin\alpha-\sin\phi\sin\beta\cos\alpha) & (\sin\phi\sin\alpha-\cos\phi\sin\beta\cos\alpha) & \cos\beta\cos\alpha\end{bmatrix}$$

where α, β and ϕ are Euler angles. ϕ is also the rotation angle about the deformed Z-axis. The recovery force is denoted by F_a. Its vector in the Oxyz frame is F_a $[0\bar{i},0\bar{j},F_a\bar{k}]$ when the beam is in its equilibrium state. The force acts on point E, which is where the beam enters the end mass. Once the beam starts to move, the force vector

becomes F_a $[F_x\bar{i}, F_y\bar{j}, F_z\bar{k}]$, where F_x, F_y and F_z are component forces of F_a along the undeformed x-, y- and z-axis directions. In the OXYZ frame, the same force vector is F_a $[0\bar{I}, 0\bar{J}, F_a\bar{K}]$ because the force is acting along the deformed Z-axis. Now the problem becomes a coordinate transformation problem. Obviously with the transformation matrix M, one can get the following

$$\begin{bmatrix} F_x \\ F_y \\ F_z \end{bmatrix} = M \times \begin{bmatrix} 0 \\ 0 \\ F_a \end{bmatrix}$$

Substituting the expression for M into the above equation gives

$$F_x = (\cos\beta \sin\alpha) F_a \tag{1}$$

$$F_y = (\sin\beta) F_a \tag{2}$$

$$F_z = (\cos\beta \cos\alpha) F_a \tag{3}$$

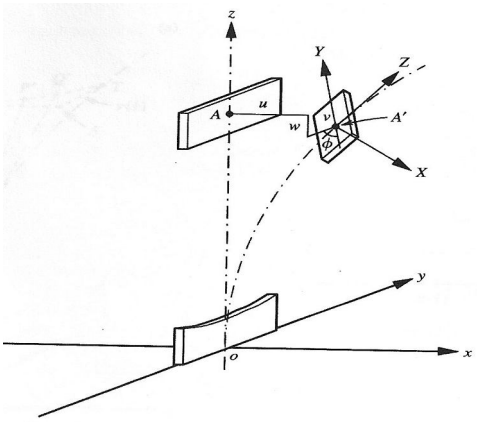

Fig 6-2 An element of the beam in both its undeformed and deformed states (Fig 2 in Forehand and Cartmell's paper (2001))

In order to determine the relationship between the three successive rotations and the actual physical displacements, Cartmell (1990) introduced a diagram which contained all the angles and the displacements. It is re-drawn as Figure 6-3 and only a few small changes to the symbols are made to relate them to Figure 6-2. First of all, he assumed ds was short enough to be regarded as a straight line. The prime ' denoted differentiation with respect

to s (linear displacement along the deformed Oz direction). He then examined the trigonometrical and geometrical relationships in the two triangles OCD and ODG and derived the following expressions.

$$\cos\alpha = \left[\frac{1-(u')^2-(v')^2}{1-(v')^2}\right]^{1/2} \quad \sin\alpha = \frac{u'}{[1-(v')^2]^{1/2}} \quad \cos\beta = [1-(v')^2]^{1/2} \quad \sin\beta = v' \qquad (4)$$

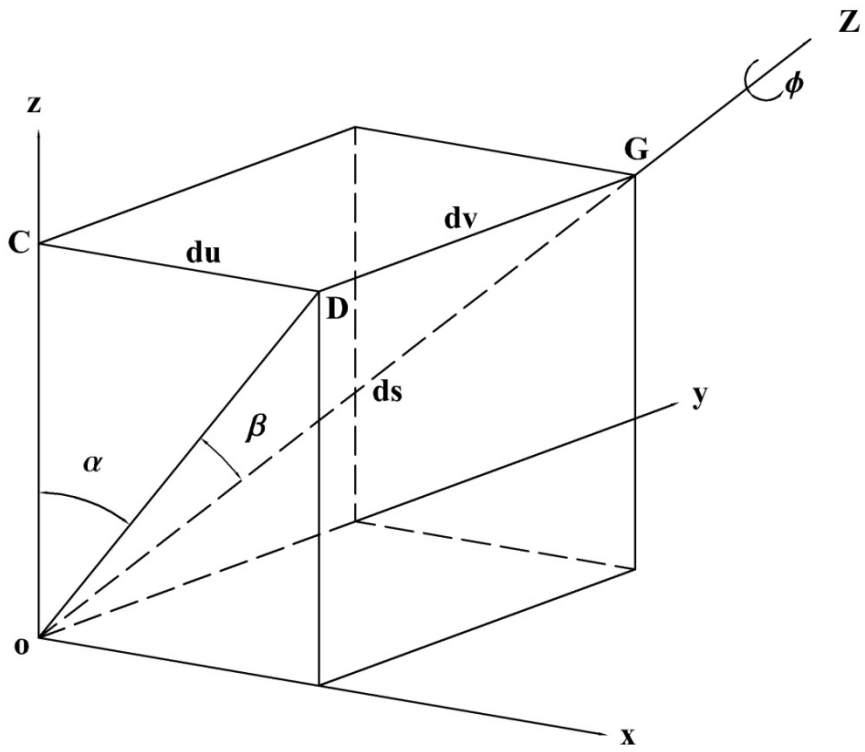

Fig 6-3 Diagram presentation of the relationship between the angles and actual displacements at an arbitrary point G.

If the above equations (4) are substituted into equations (1) to (3), the equations for F_x, F_y and F_z will be cumbersome though highly accurate. For the sake of practicality, it is necessary to compromise the degree of accuracy by neglecting certain "small" terms on the grounds that they are of less significance than other "large" terms. The concept of smallness is discussed by Cartmell (1990) and Cartmell *et al* (2003). In equation (4), for example, $(u')^2$ and $(v')^2$ are "small" compared with u' and v', which are assumed to be small themselves, so they are approximated as follows

$$\cos\alpha = 1 \quad \sin\alpha = u' \quad \cos\beta = 1 \quad \sin\beta = v' \qquad (5)$$

In reference (Cartmell 1990), the curvature about X-axis, denoted by k_1, was derived with the application of Euler-Kirchhoff-Love theory for rods (Love, 1944) and under the assumptions of small bending u and v. k_1 is given by

$$k_1 = u''\phi - v''$$

It is also justifiable to say that the beam is extremely stiff in the Oyz-plane in this case, which leads to another assumption that k_1 is virtually zero. That gives us this equation

$$u''\phi = v'' \tag{6}$$

To satisfy equation (6), ϕ needs to be small as well, given that u'' and v'' are small from the previous assumptions. Therefore it is possible to write

$$\cos\phi = 1 \qquad \sin\phi = \phi \tag{7}$$

Substituting equations (6) and (7) into equations (1) to (3) and neglecting weak terms, i.e. quadratic terms in this case, and rearranging them gives

$$F_x = u'F_a \tag{8}$$

$$F_y = v'F_a \tag{9}$$

$$F_z = F_a \tag{10}$$

Because the displacement u is small and the displacement v is even smaller, the distance z up the z-axis and arc length s up the deformed Z-axis are approximately equal and can be used interchangeably. So u' and v' in equations (8) and (9) are also the differentiations of u and v with respect to z. On this basis, as shown in Figure 6-3, two equations can be obtained as

$$\sin\alpha = u' = \frac{du}{dz} \qquad \sin\beta = v' = \frac{dv}{dz} \tag{11}$$

It is then possible to obtain the expressions for u' and v' at the point of action of the force F_a acting point, i.e. the end point of the beam, point E as shown in Figure 6-4. It is clearly

seen that ΔOCD and ΔOAB, ΔODG and ΔOBE are similar triangles, which leads to the following expressions, on the basis of equation (11)

$$u' = \frac{u(l)}{l} \ , \ v' = \frac{v(l)}{l} \tag{12}$$

Substituting equations (12) into equations (8) and (9)gives

$$F_x = \frac{u(l)}{l} F_a \tag{13}$$

$$F_y = \frac{v(l)}{l} F_a \tag{14}$$

where $u(l)$ and $v(l)$ are the displacements of point E in the Oxz and Oyz planes respectively, and where l is the length of the beam.

The recovery force, F_a, acts tangentially to the curvature of the beam and is defined at $z = l$, therefore the assumption that it points to the origin is entirely acceptable for small displacements of the beam. This assumption does lose some of its validity as the displacements of the beam increase significantly.

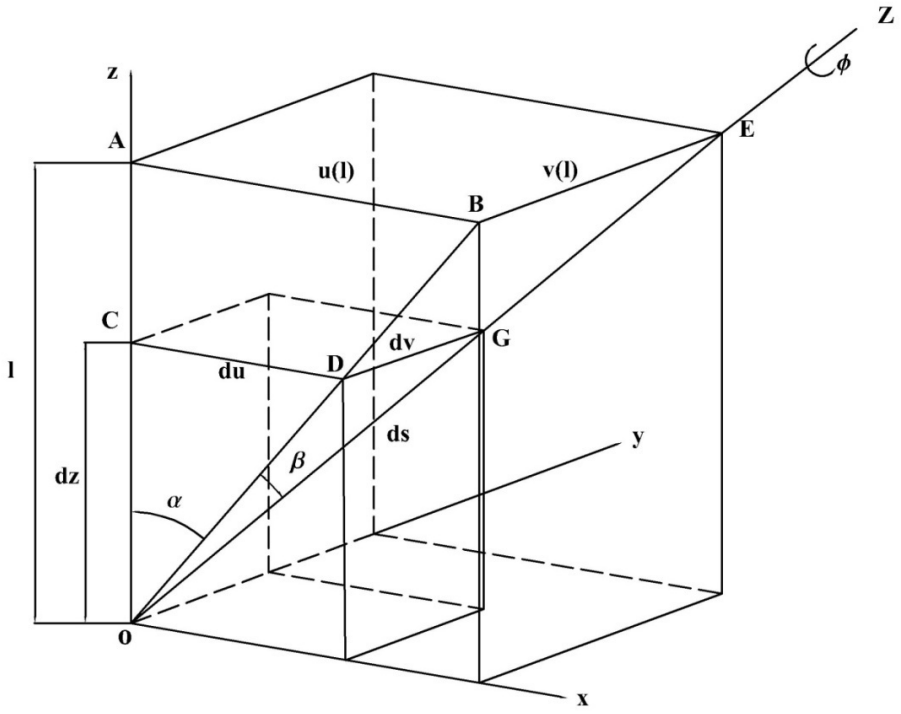

Fig 6-4 Schematic presentation of the relationship between the angles and actual displacements at point E, the end point of the beam

6.1.2 Expressions for $u(l)$, $v(l)$ and $w(l)$

First, the coordinate of the acting point of F_a, point E when the beam deforms, needs to be clarified. As shown in Figure 6-2, the coordinates are $[u(l), v(l), l - w(l)]$ because at point E z equals l. Distance l is the portion of the beam from the top of the base-clamp to point E. Deflection $u(l)$ is easily obtained if z is replaced by l in the equation $u(z) = f_1(z)u_1 + f_2(z)u_2$. $f_1(z)$ and $f_2(z)$ only depend on the spatial coordinate z, while functions u_1 and u_2 depends only on t. Hence

$$u(l) = f_1(l)u_1 + f_2(l)u_2 \tag{15}$$

To get the expression for $v(l)$ is more complicated. The origin of the displacement v in the Oyz plane is due to combined bending and torsion. That suggests that the expression for v is supposed to be a function of u and ϕ. Forehand and Cartmell (2001) considered two points P and Q, along the deformed Z-axis, at distance z and $z + \delta z$ respectively. Tangents to these two points intersect the plane $z = l$ at points P' and Q'. Figure 6-5 shows the details.

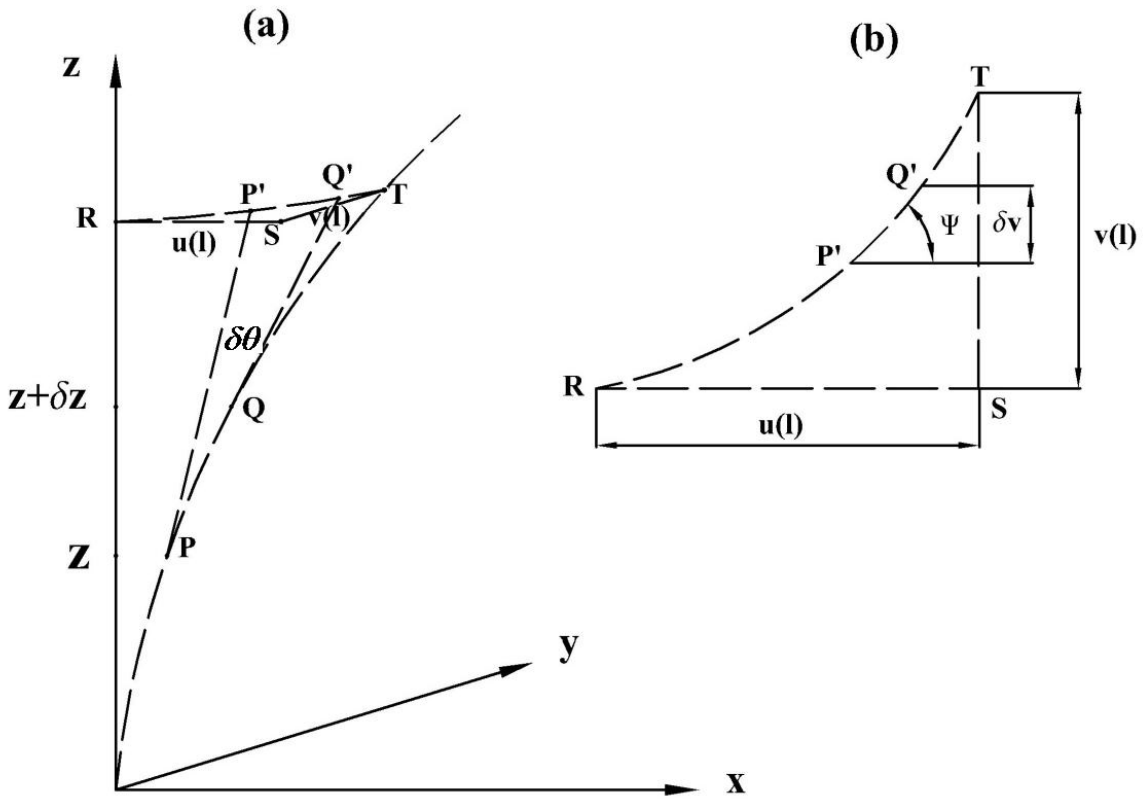

Fig 6-5 Geometrical relationships (Fig 3 in Forehand and Cartmell's paper (2001))

An approximate expression can be proposed for δv as shown in Figure 6-5 (b) when the arc $P'Q'$ is treated as a straight line for small δv and ψ .

$$\delta v = \left|P'Q'\right|\psi \qquad \left|P'Q'\right| \text{ defines the length of the arc } P'Q' . \tag{16}$$

Figure 6-5 (b) shows that

$$\left|P'Q'\right| = (l - z)\delta\theta \tag{17}$$

if the length of the both tangents is approximately $l - z$.

Appendix A in reference (Forehand and Cartmell, 2001) gives the proof for stating that

$$\psi = \phi \tag{18}$$

Combining equations (16)(17)(18) and the equation for the curvature about the y-axis $k_2 = d\theta / dz$ gives

$$\frac{dv}{dz} = (l - z)\phi k_2 \tag{19}$$

Substituting the curvature equation $k_2 = u''(1+\phi^2)$ into equation (19), and neglecting the $u''\phi^3$ term, and then integrating from $z = 0$ to $z = l$ gives

$$v(l) = \int_0^l (l - z)u''\phi dz \tag{20}$$

Finally with $u'' = f_1''u_1 + f_2''u_2$ and $\phi = g_1\phi_1$, $v(l)$ is expressed by the functions of the chosen mode shapes and the modal coordinates as

$$v(l) = \int_0^l (l - z)g_1\phi_1(f_1''u_1 + f_2''u_2)dz \tag{21}$$

This can be re-written in a simpler form

$$v(l) = B_1\phi_1u_1 + B_2\phi_1u_2 \tag{22}$$

where g_1 is the mode shape for the fundamental torsion mode, and

$$B_1 = \int_0^l (l-z) g_1 f_1'' dz \quad \text{and} \quad B_2 = \int_0^l (l-z) g_1 f_2'' dz \tag{23}$$

Under the assumption $l_0 - l \le l$,The displacement w relates to u is given by the expression

$$w = \frac{1}{2}\int_0^l (\frac{du}{dz})^2 dz = \frac{1}{2}\int_0^l (u')^2 dz \tag{24}$$

Using $u = f_1 u_1 + f_2 u_2$ again in equation (24) gives

$$w(l) = \frac{1}{2}(\int_0^l (f_1')^2))u_1^2 + (\int_0^l f_1' f_2'))u_1 u_2 + \frac{1}{2}(\int_0^l (f_2')^2))u_2^2 \tag{25}$$

6.1.3 Expressions for the Generalized Forces

The elemental work done by the force F_a is expressed as

$$\delta W = -F_x \delta u(l) - F_y \delta v(l) + F_z \delta w(l) \tag{26}$$

$\delta u(l), \delta v(l), \delta w(l)$ are the displacements of the component forces F_x F_y F_z along the x-,y- and z-axis directions. If u_1 has a virtual displacement of δu_1 and u_2 and ϕ_1 are held constant, we then have the following

$$\delta u(l) = \frac{\partial u(l)}{\partial u_1}\delta u_1 \qquad \delta v(l) = \frac{\partial v(l)}{\partial u_1}\delta u_1 \qquad \delta w(l) = \frac{\partial w(l)}{\partial u_1}\delta u_1 \tag{27}$$

Substituting equations (27) into equation (26) gives

$$\delta W = (-F_x \frac{\partial u(l)}{\partial u_1} - F_y \frac{\partial v(l)}{\partial u_1} + F_z \frac{\partial w(l)}{\partial u_1})\delta u_1 \tag{28}$$

The right hand side part in equation (28) is clearly just $F_{u1}\delta u_1$. F_{u1} is the generalised force corresponding to the coordinate u_1.

The next problem is to get expressions for $\frac{\partial u(l)}{\partial u_1}$, $\frac{\partial v(l)}{\partial u_1}$ and $\frac{\partial w(l)}{\partial u_1}$ from equations (22) and (25). The results are listed as

$$\frac{\partial u(l)}{\partial u_1} = f_1(l) \qquad \frac{\partial v(l)}{\partial u_1} = B_1\phi_1 \qquad \frac{\partial w(l)}{\partial u_1} = (\int_0^l (f_1')^2 dz)u_1 + (\int_0^l f_1' f_2' dz)u_2 \qquad \text{(29) to (31)}$$

Therefore, the expression for F_{u1}, after equations (13)(14)(10) and equations (29) to (31) are substituted into equation (28), and taking the two strips, thus $2F_a$, into account, is,

$$F_{u1} = 2\left\{ Xu_1 + Yu_2 - \frac{\left[f_1(l)u_1 + f_2(l)u_2 \right] f_1(l)}{l} - \frac{\left[B_1\phi_1 u_1 + B_2\phi_1 u_2 \right] B_1\phi_1}{l} \right\} F_a \qquad (32)$$

where $X = \int_0^l (f_1')^2 dz \quad Y = \int_0^l (f_1' f_2') dz$

In the same manner, the expressions for the generalised forces F_{u2} and $F_{\phi 1}$ are

$$F_{u2} = 2\left\{ Zu_2 + Yu_1 - \frac{\left[f_1(l)u_1 + f_2(l)u_2 \right] f_2(l)}{l} - \frac{\left[B_1\phi_1 u_1 + B_2\phi_1 u_2 \right] B_2\phi_1}{l} \right\} F_a \qquad (33)$$

$$F_{\phi 1} = -2\frac{\left[B_1\phi_1 u_1 + B_2\phi_1 u_2 \right](B_1 u_1 + B_2 u_2)}{l} F_a \qquad (34)$$

where $Z = \int_0^l (f_2')^2 dz$

6.2 Equations of Motion

The equations of motion are derived by using Lagrange's equations. Due to the small dimensions of the SMA strips, the expressions for the kinetic and potential energies, described as equations (3) and (7) in Chapter 3, are still applicable in this system. Hence,

$$\frac{d}{dt}\frac{\partial T}{\partial \dot{u}_1} - \frac{\partial T}{\partial u_1} + \frac{\partial U}{\partial u_1} = F_{u1}$$

$$\frac{d}{dt}\frac{\partial T}{\partial \dot{u}_2} - \frac{\partial T}{\partial u_2} + \frac{\partial U}{\partial u_2} = F_{u2}$$

$$\frac{d}{dt}\frac{\partial T}{\partial \dot{\phi}_1} - \frac{\partial T}{\partial \phi_1} + \frac{\partial U}{\partial \phi_1} = F_{\phi 1}$$

where $T = \frac{1}{2} m_0 (\dot{u}_1^2 + \dot{u}_2^2 + (\dot{W}_B - \dot{w}_0)^2 + \dot{v}_0^2) + \frac{1}{2} I_0 \dot{\phi}_0^2$

$$U = \frac{1}{2}\left[EI_y N - m_0 g X \right] u_1^2 + \left[EI_y S - m_0 g Y \right] u_1 u_2 + \frac{1}{2}\left[EI_y P - m_0 g Z \right] u_2^2 + \frac{1}{2} cGJQ\phi_1^2 + m_0 g W_B$$

Implementing the above formulas leads to the following three equations of motion,

$$\begin{aligned}
&\ddot{u}_1[1 + B_1^2\phi_1^2 + (Xu_1 + Yu_2)^2] + 2\dot{u}_1\dot{u}_2 Y(Xu_1 + Yu_2) + \dot{u}_1^2 X(Xu_1 + Yu_2) \\
&+\dot{u}_2^2 Z(Xu_1 + Yu_2) + \ddot{u}_2(Xu_1 + Yu_2)(Yu_1 + Zu_2) + B_1^2\phi_1\ddot{\phi}_1 u_1 + 2B_1^2\phi_1\dot{\phi}_1\dot{u}_1 \\
&+2B_1B_2\phi_1\dot{\phi}_1\dot{u}_2 + B_1B_2\phi_1\ddot{\phi}_1 u_2 + B_1B_2\phi_1^2\ddot{u}_2 + (RN - gX - AX + \frac{Af_1^{\,2}(l)}{l})u_1 \\
&+(RS - gY - AY + \frac{Af_1(l)\,f_2(l)}{l})u_2 + \hat{A}_B\Omega^2\cos(\Omega t)(Xu_1 + Yu_2) \\
&-\frac{AB_1^2}{l}\phi_1^2 u_1 - \frac{AB_1B_2}{l}\phi_1^2 u_2 = 0
\end{aligned}$$

$$\begin{aligned}
&\ddot{u}_2[1 + B_2^2\phi_1^2 + (Yu_1 + Zu_2)^2] + 2\dot{u}_1\dot{u}_2 Y(Yu_1 + Zu_2) + \dot{u}_1^2 Z(Yu_1 + Zu_2) \\
&+\dot{u}_1^2 X(Yu_1 + Zu_2) + \ddot{u}_1(Xu_1 + Yu_2)(Yu_1 + Zu_2) + B_2^2\phi_1\ddot{\phi}_1 u_2 + 2B_2^2\phi_1\dot{\phi}_1\dot{u}_2 \\
&+2B_1B_2\phi_1\dot{\phi}_1\dot{u}_1 + B_1B_2\phi_1\ddot{\phi}_1 u_1 + B_1B_2\phi_1^2\ddot{u}_1 + (RP - gZ - AZ + \frac{Af_2^{\,2}(l)}{l})u_2 \\
&+(RS - gY - AY + \frac{Af_1(l)\,f_2(l)}{l})u_1 + \hat{A}_B\Omega^2\cos(\Omega t)(Yu_1 + Zu_2) \\
&-\frac{AB_2^2}{l}\phi_1^2 u_2 - \frac{AB_1B_2}{l}\phi_1^2 u_1 = 0
\end{aligned}$$

$$\begin{aligned}
&\ddot{\phi}_1[1 + m_I(B_1u_1 + B_2u_2)^2] + \dot{\phi}_1[2m_I(B_1\dot{u}_1 + B_2\dot{u}_2)(B_1u_1 + B_2u_2)] \\
&+\phi_1[m_I(B_1\ddot{u}_1 + B_2\ddot{u}_2)(B_1u_1 + B_2u_2)] + \phi_1(\frac{cGJQ}{I_0}) - \frac{BB_1^2}{l}u_1^2\phi_1 \\
&-\frac{2BB_1B_2}{l}u_1u_2\phi_1 - \frac{BB_2^2}{l}u_2^2\phi_1 = 0
\end{aligned} \qquad \text{(35) to (37)}$$

where $R = \frac{EI_y}{m_0}$, $m_I = \frac{m_0}{I_0}$, $A = \frac{2F_a}{m_0}$, $B = \frac{2F_a}{I_0}$, and $W_B = \hat{A}_B\cos(\Omega t)$ noting that Ω is the frequency of the excitation.

6.3 Analysis of the Instability Zones

Following the ordering schemes described in Chapter 3 and application of the multiple scale method again yields the zeroth and first-order perturbation equations:

(Note: in this case, the term $\left(RS - gY + AY - Af_1(l)\, f_2(l)/l\right)$ in equations (35) and (36) is set to $\left(RS - gY - AY + Af_1(l)\, f_2(l)/l\right)$ because it is found numerically that $\left(RS - gY - AY + Af_1(l)\, f_2(l)/l\right) << \left(RN - gX - AX + Af_1^{\,2}(l)/l\right)$ $\left(RS - gY - AY + Af_1(l)\, f_2(l)/l\right) << \left(RP - gZ - AZ + Af_2^{\,2}(l)/l\right)$ under certain conditions. More details can be seen in section 6.5 in this chapter.)

ε^0:

$$D_0^2\bar{u}_{10} + (RN - gX - AX + \frac{Af_1^{\,2}(l)}{l})\bar{u}_{10} = 0$$

$$D_0^2\bar{u}_{20} + (RP - gZ - AZ + \frac{Af_2^{\,2}(l)}{l})\bar{u}_{20} = 0$$

$$D_0^2\bar{\phi}_{10} + \frac{cGJQ}{I_0}\bar{\phi}_{10} = 0 \qquad \text{(38) to (40)}$$

ε^1:

$$D_0^2\bar{u}_{11} + (RN - gX - AX + \frac{Af_1^{\,2}(l)}{l})\bar{u}_{11} = -2D_0D_1\bar{u}_{10} - 2\zeta_1\omega_1 D_0\bar{u}_{10} - \hat{A}_B\Omega^2\cos(\Omega t)(X\bar{u}_{10} + Y\bar{u}_{20})$$
$$-(RS - gY - AY + \frac{Af_1(l)\, f_2(l)}{l})\bar{u}_{20}$$

$$D_0^2\bar{u}_{21} + (RP - gZ - AZ + \frac{Af_2^{\,2}(l)}{l})\bar{u}_{21} = -2D_0D_1\bar{u}_{20} - 2\zeta_2\omega_2 D_0\bar{u}_{20} - \hat{A}_B\Omega^2\cos(\Omega t)(Z\bar{u}_{20} + Y\bar{u}_{10})$$
$$-(RS - gY - AY + \frac{Af_1(l)\, f_2(l)}{l})\bar{u}_{10}$$

$$D_0^2\bar{\phi}_{11} + \frac{cGJQ}{I_0}\bar{\phi}_{11} = -2D_0D_1\bar{\phi}_{10} - 2\zeta_t\omega_t D_0\bar{\phi}_{10} \qquad \text{(41) to (43)}$$

Solutions to the zero-th order perturbation equations (38) to (40) are:

$$\bar{u}_{10} = A_1e^{i\omega_1T_0} + \bar{A}_1e^{-i\omega_1T_0} \qquad \bar{u}_{20} = A_2e^{i\omega_2T_0} + \bar{A}_2e^{-i\omega_2T_0} \qquad \bar{\phi}_{10} = C_1e^{i\omega_tT_0} + \bar{C}_1e^{-i\omega_tT_0} \qquad \text{(44) to (46)}$$

where $A_1 = A_1(T_1, T_2)$, $A_2 = A_2(T_1, T_2)$, $C_1 = C_1(T_1, T_2)$, with $\omega_1^2 = RN - gX - AX + \dfrac{Af_1^2(l)}{l}$,

$\omega_2^2 = RP - gZ - AZ + \dfrac{Af_2^2(l)}{l}$ and $\omega_t^2 = \dfrac{cGJQ}{I_0}$.

Substituting the solutions of zeroth order equations into the first order equations (41) to (43) leads to

$$D_0^2\overline{u}_{11} + \omega_1^2\overline{u}_{11} = e^{i\omega_1 T_0}\left(\begin{array}{l} -i2\omega_1 D_1 A_1 - i2\zeta_1\omega_1^2 A_1 - \dfrac{\hat{A}_B\Omega^2}{2}XA_1 e^{-i\Omega T_0} - \dfrac{\hat{A}_B\Omega^2}{2}YA_2 e^{-i(\Omega+\omega_1-\omega_2)T_0} \\ -\dfrac{\hat{A}_B\Omega^2}{2}Y\overline{A}_2 e^{-i(\Omega+\omega_1+\omega_2)T_0} - \dfrac{\hat{A}_B\Omega^2}{2}X\overline{A}_1 e^{-i(\Omega+2\omega_1)T_0} - \dfrac{\hat{A}_B\Omega^2}{2}XA_1 e^{i\Omega T_0} \\ -\dfrac{\hat{A}_B\Omega^2}{2}YA_2 e^{i(\Omega-\omega_1+\omega_2)T_0} - \dfrac{\hat{A}_B\Omega^2}{2}X\overline{A}_1 e^{i(\Omega-2\omega_1)T_0} - \dfrac{\hat{A}_B\Omega^2}{2}Y\overline{A}_2 e^{i(\Omega-\omega_1-\omega_2)T_0} \\ +(i2\zeta_1\omega_1^2\overline{A}_1 + 2i\omega_1 D_1\overline{A}_1)e^{-i2\omega_1 T_0} - \overline{p}^2 A_2 e^{i(\omega_2-\omega_1)T_0} - \overline{p}^2\overline{A}_2 e^{-i(\omega_1+\omega_2)T_0} \end{array}\right) \quad (47)$$

$$D_0^2\overline{u}_{21} + \omega_2^2\overline{u}_{21} = e^{i\omega_2 T_0}\left\{\begin{array}{l} -i2\omega_2 D_1 A_2 - i2\zeta_2\omega_2^2 A_2 - \dfrac{\hat{A}_B\Omega^2}{2}ZA_2 e^{-i\Omega T_0} - \dfrac{\hat{A}_B\Omega^2}{2}YA_1 e^{-i(\Omega-\omega_1+\omega_2)T_0} \\ -\dfrac{\hat{A}_B\Omega^2}{2}Y\overline{A}_1 e^{-i(\Omega+\omega_1+\omega_2)T_0} - \dfrac{\hat{A}_B\Omega^2}{2}Z\overline{A}_2 e^{-i(\Omega+2\omega_2)T_0} - \dfrac{\hat{A}_B\Omega^2}{2}ZA_2 e^{i\Omega T_0} \\ -\dfrac{\hat{A}_B\Omega^2}{2}YA_1 e^{i(\Omega+\omega_1-\omega_2)T_0} - \dfrac{\hat{A}_B\Omega^2}{2}Y\overline{A}_1 e^{i(\Omega-\omega_1-\omega_2)T_0} - \dfrac{\hat{A}_B\Omega^2}{2}Z\overline{A}_2 e^{i(\Omega-2\omega_2)T_0} \\ +(i2\zeta_2\omega_2^2\overline{A}_2 + 2i\omega_2 D_1\overline{A}_2)e^{-i2\omega_2 T_0} - \overline{p}^2 A_1 e^{i(\omega_1-\omega_2)T_0} - \overline{p}^2\overline{A}_1 e^{-i(\omega_1+\omega_2)T_0} \end{array}\right\} \quad (48)$$

$$D_0^2\overline{\phi}_{11} + \omega_t^2\overline{\phi}_{11} = e^{i\omega_t T_0}\left\{-i2\omega_t D_1 C_1 - i2\zeta_t\omega_t^2 C_1 + (i2\zeta_t\omega_t^2\overline{C}_1 + 2i\omega_t D_1\overline{C}_1)e^{-i2\omega_t T_0}\right\} \quad (49)$$

where $\overline{p}^2 = RS - gY - AY + \dfrac{Af_1(l)\,f_2(l)}{l}$

When the same procedure of obtaining the expressions of the transition curves descreibed in Chapter 3 is followed, the transition curves for primary parametric resonances and sum-type resonance are expressed as follows

$$\sigma = \pm\sqrt{(\frac{X}{2\omega_1})^2(\hat{A}_B\Omega^2)^2 - (2\zeta_1\omega_1)^2} \quad (50)$$

$$\delta = \pm\sqrt{(\frac{Z}{2\omega_2})^2(\hat{A}_B\Omega^2)^2 - (2\zeta_2\omega_2)^2} \tag{51}$$

$$\alpha = \pm\sqrt{\frac{(\zeta_1\omega_1 + \zeta_2\omega_2)^2(Y^2\Omega^4\hat{A}_B^2 - 16\zeta_1\zeta_2\omega_1^2\omega_2^2)}{16\zeta_1\zeta_2\omega_1^2\omega_2^2}} \tag{52}$$

The difference-type resonance is not possible in practise again because it requires either negative damping or negative natural frequencies.

6.4 Results and Discussions

The theoretical results are based on the values given in the Table 5-1 in Chapter 5. Table 6-1 gives the different parameters of the beam system against the variations of the force F_a. According to equations (50) (51) and (52), the transition curves for the primary and combination parametric resonances are plotted as Figures 6-6, 6-7 and 6-8. In these three cases, the damping ratios for the first and second bending modes are assumed to be $\zeta_1 = 0.001$ and $\zeta_2 = 0.003$. As expected, these curves show that the instability regions are increased as the force F_a increases, because the natural frequencies decrease, if the effect of the force on the damping ratios is ignored for this analysis. The force F_a affects the transition curves up to the beam's dynamic buckling.

The above analysis is about the effect of the recovery force alone. If the changes in the stiffness of the SMA strips are included, and take place at the time of generating recovery forces, the beam becomes stiffer when the SMA strips stay fully in their austenitic phase, thus further increasing the instability zones. If both the recovery force and stiffness changes are involved, then which one plays the main role needs to be discovered.

F_a (N)	X	Y	Z	ω_1^2	ω_2^2	$\lvert\bar{p}^2\rvert$
0	3.196	-4.172	51.851	1222.72	163998	40.723
2	3.237	-4.387	51.884	1319.77	156405	112.419
4.5	3.297	-4.689	51.921	1297.61	146918	306.478

Table 6-1 Influence of the force F_a on the parameters of the system

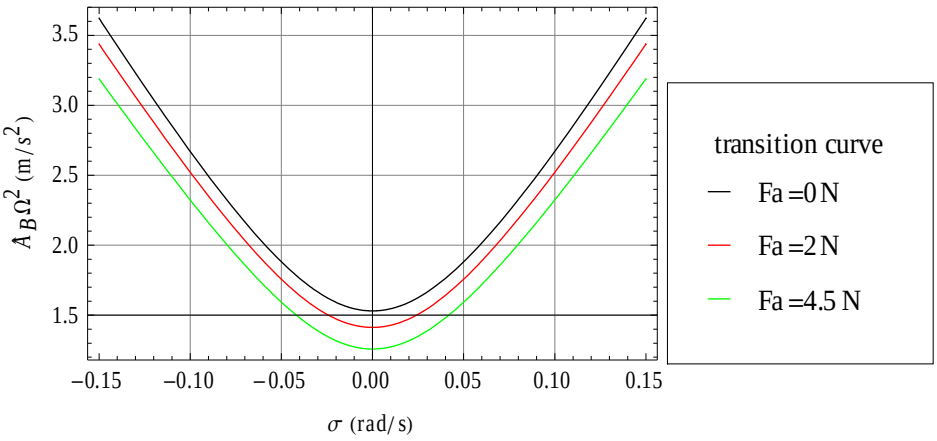

Fig 6-6 Stability chart showing the zoning for the principal parametric resonance $\Omega = 2\omega_1 + \varepsilon\sigma$

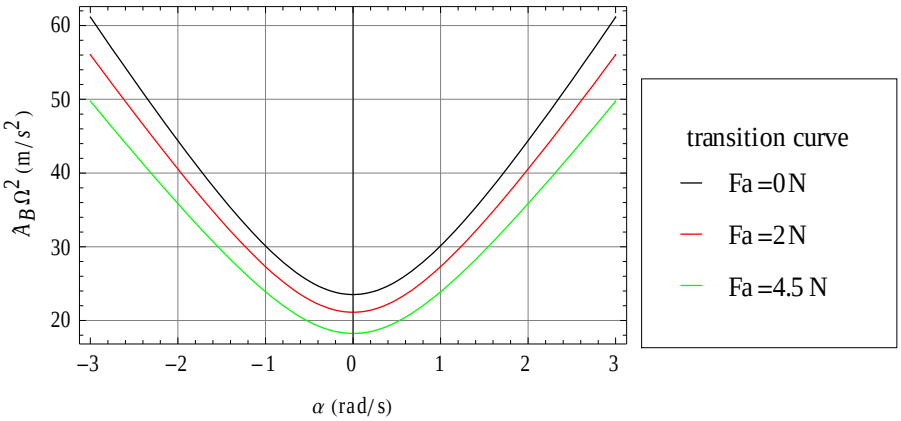

Fig 6-7 Stability chart for the combination parametric resonance $\Omega = \omega_1 + \omega_2 + \varepsilon\alpha$

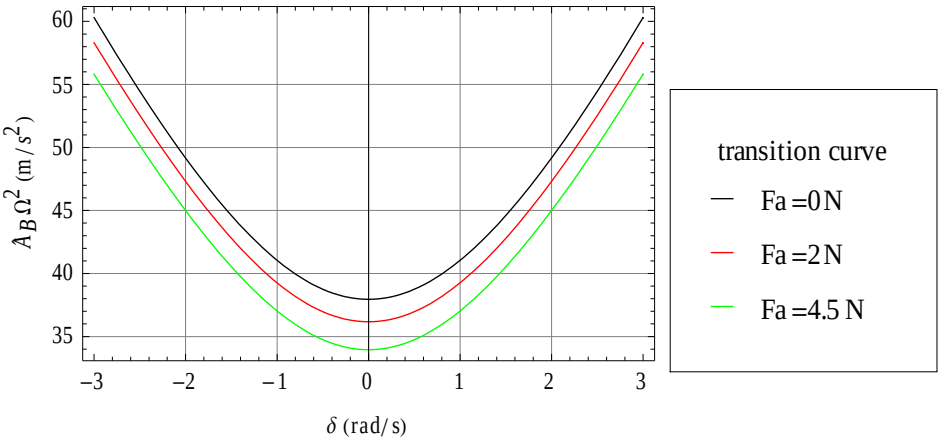

Fig 6-8 Stability chart for the principal parametric resonance $\Omega = 2\omega_2 + \varepsilon\delta$

Chapter 7

Experimental Investigation of two Composite Beams with Integrated SMA Strips

This chapter explores the influence of SMA strips by means of experiments on the properties, such as natural frequencies, damping ratio, instability zones, of two systems, system 1 and system 2. The two systems, a cantilever beam with two bonded SMA strips and an attached lumped end mass, are depicted in Figure 7-1 and 7-2. In system 1, two vertical strips are bonded to a g-e beam along the centre line on both sides symmetrically along its length, whilst in system 2, two oppositely orientated diagonal strips are bonded to the beam, one on each side. This chapter consists of two parts. The first part describes a hammer impact test conducted on both systems 1 and 2. In this test, the two strips were 2 mm thick and the g-e beam was 132 mm long. The characteristic transformation temperature of the SMA strips, A_f was 75°C. The lumped end mass was made of steel. In the second part, the dynamic mechanical properties of system 1 and 2 were investigated by measuring the first vibration mode. In this part, two thinner strips, with a thickness of only 0.5 mm and a longer g-e beam, with a length of 270mm, were used instead. A_f was 30°C in this case. In both parts, the effectiveness of the control ability of the SMA strips on the systems were determined by comparing the properties of the systems with and without SMAs, by comparing the properties of systems when the strips were activated and unactivated. Discussions are followed by the comparisons.

7.1 Hammer Impact Test

7.1.1 Descriptions of the Systems

The SMA strips in this test are Nickel-Titanium (Ni-Ti) alloy manufactured by Memry GmBH in Germany. The engineering properties are listed in Table 7-1. The strips were bonded to the beam by using an epoxy resin adhesive. The properties of the system are described in Table 7-2. The adhesive consisted of a resin called “epidian” and the hardener was called “z-1”. The resin and hardener were mixed 1:10 by weight. It took about 10 hours for the mixture to become solid. Once the strips were tightly bonded to the beam, one end of this

composite beam was wrapped up with insulating tape and then was clamped. The tape was used to insulate the strips from the clamps when they were heated by passing the electrical current. Two half masses were attached to the free end of the composite beam by means of screws. Finally the whole structure, two clamps, the composite beam and the end mass was fixed in a vice. The set-up for system 1 is shown in Figure 7-3. The same procedure was applied to system 2.

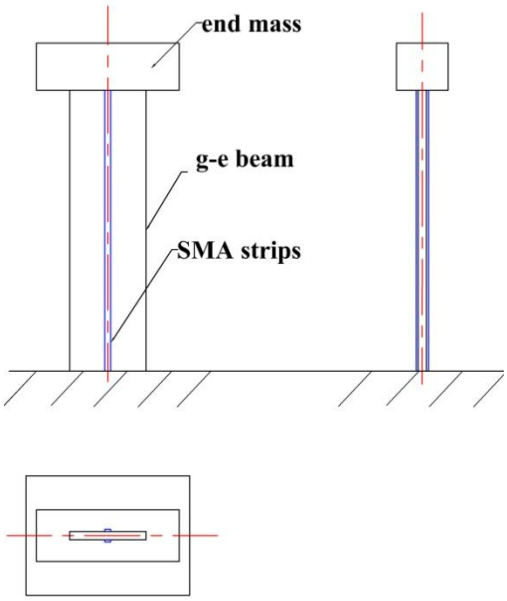

Fig 7-1 System 1, a g-e beam with two central strips and an attached end mass

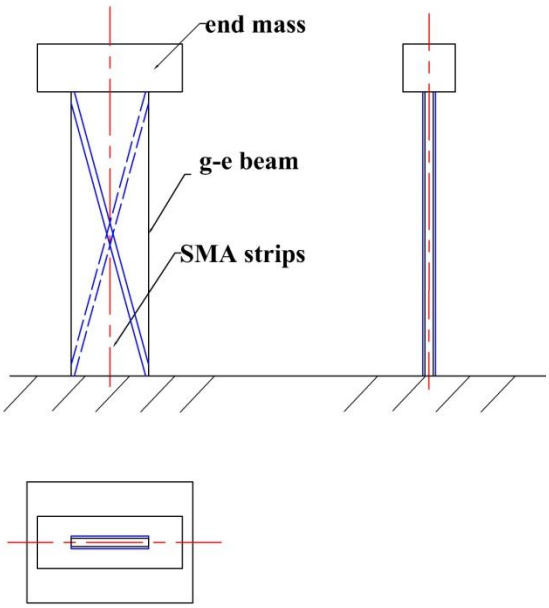

Fig 7-2 System 2, a g-e beam with two diagonal strips and an attached end mass

Chemical composition	Ni 55.49 [wt-%], Ti bal [wt-%], C 310 [ppm], O 185 [ppm]
Trans. temp [°C] A_f	75°C
Density (kg/m^3)	6448.1
Thickness	2.0 mm
Width	2.0 mm

Table 7-1 Properties of the Ti-Ni strips

Note: Bal means the balance to 100%; Ppm parts per million; A_f is the temperature at which the phase transformation from Martensite to Austenite.

Geometric dimensions		
L_b = 132 mm (system 1)	L_b = 132.6 mm (system 2)	W_b = 13 mm
T_b = 2.2 mm	W_m = 15 mm	D_m = 15 mm
Material properties		
ρ_b = 1865 kg/m^3	ρ_m = 7800 kg/m^3	E_b = 13.19 GPa	G_b = 12.24 GPa

Table 7-2 Dimensions and material properties of System 1 and 2

Note: The properties of the beam itself are labelled with subscript b, and the subscript m refers to the end mass properties.

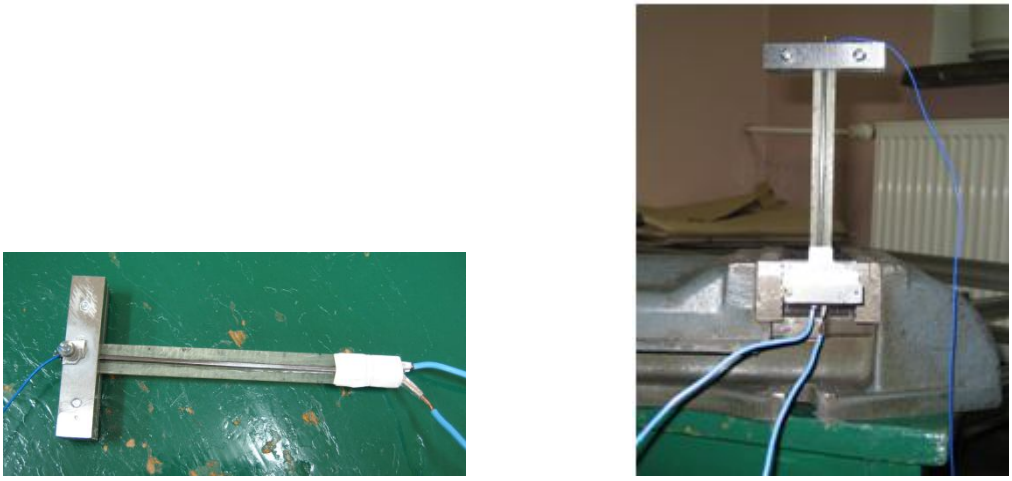

Fig 7-3 Experimental rig for hammer impact tests

7.1.2 Experimental Procedure

The first set of experiments was intended to determine the natural frequencies of the composite beam in bending and torsion for system 1 and 2. The hammer impact test described in Chapter 4 was applied The excitation was provided by a small hammer, and the response signal was measured by a small, low mass, piezo-sensor. A modal analysis system with spectral acquisition software designed by LMS™ was used to analyze the results. The geometry of the system for the hammer impact tests was shown in Figure 7-4. Altogether there were 16 points identified on the beam and two points, P19 and P29, on the end mass. The accelerometer was glued on the top middle surface of the end mass. Each point, apart from the two fixed points, P11 and P12, was impacted along the y-axis. To get better results, each point was excited six times and the average of the results from the six impacts was used for further analysis. The experiments were conducted on system 2 first with various

end masses. There were 5 end masses tested. The lengths of the end masses were 50 mm, 60 mm, 70 mm, 80 mm and 100 mm. The five different end masses were mounted to the beam in turn and all tests were carried out when the temperature of the strips were room temperature, about 20°C, were around 30°C and around 40°C to understand the influence of temperature on the natural frequencies. Table 7-3 tells the actural average temperatures along the strip length on system 2 with the five end masses. The test was then carried out on system 1 when only the end mass was used whose length was 70 mm. The last test in this part was done on the system 1 but without strips and the end mass had a length of 70 mm too. Both tests were implemented under the above three different temperatures as well.

Temp(°C) / L of the EM(mm)	20°C	30°C	40°C
50	20	29	37
60	22	30	40
70	20	29	40
80	22	29	40
100	23	32	42

Table 7-3 Different strip temperatures vs. the end mass length

Note: EM is an abbreviation adopted here for end mass

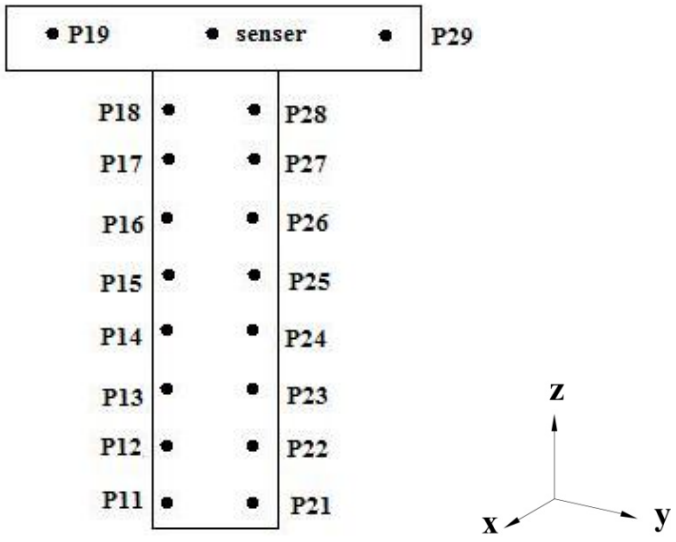

Fig 7-4 Geometry of the system for the hammer impact tests

7.1.3 Results and Discussions

(1) As can be seen from Table 7-4, in the without-strip case, the natural frequency of the 1st bending mode is 7.44 Hz. In theory, the natural frequencies of the bending modes in the without-strip case that a cantilever beam with an end mass are determined by using the equation of $f = (\beta / l)^2 * \sqrt{EI_y / \rho A}) / 2\pi$ .The value of β can be obtained from the boundary conditions, see **Appendix 1** for details. Therefore, based on 7.44 Hz, the Young's modulus of the g-e beam can be calculated as 13.2 GPa, which is much smaller than what the manufacture provided, 25.5 GPa. When the Young's modulus is considered as 13.2 GPa, the above equation is applied again that the theoretical result of the natural frequency of the 2nd bending mode is calculated as 167.22 Hz, close to the experimental result, 177.5 Hz.

(2) The SMA strips have a strong effect on the properties of the system. If one compares the results in the without-strip case to those of the central-strip case, shown in Table 7-4, the natural frequencies of the 1st bending, 1st torsion and 2nd bending modes are increased from 7.44 Hz to 25.35 Hz by 240.7%, from 27.07 Hz to 39.44 Hz, therefore by 45.7%, and from 177.5 Hz to 476.79 Hz, by 168.6%; Compared to the diagonal-strip case, the natural frequencies of the 1st bending, 1st torsion and 2nd bending modes are increased from 7.44 Hz to 22.03 Hz, by 196.1%, from 27.07 Hz to 41.92 Hz, by 54.9%, and from 177.5 Hz to 336.86 Hz by, 89.8%. It shows that the SMA strips make the beam structure very difficult to bend and twist.

(3) The parallel strips make the beam stiffer in bending and the diagonal strips make it stiffer in torsion as shown by the frequencies of the first and second bending modes decreasing from 25.34 Hz in the central-strip case to 22.03 Hz in the diagonal-strip case, 476.79 Hz to 336.86 Hz, whilst the frequency of the torsion mode has increased from 39.44 Hz to 41.92 Hz. This can be explained as follows:

In system 1, when the beam bends to one side, the extension of the outside strip is assumed to be Δl as depicted in Figure 7-5. Therefore the extension per strip length is $\Delta l / l$, where l is the original length of the strip. The inside strip will contract Δl but the change per length is also $\Delta l / l$. In system 2, it is assumed that the system has exactly the same bending deflection as for system 1. That is, the extension of the outside strip along the central line

direction of the beam is Δl. The original length of the outside strip is $\sqrt{l^2+w^2}$, where w is the width of the beam as depicted in Figure 7-5, and the new length after bending is $\sqrt{(l+\Delta l)^2+w^2}$. Therefore the extension per strip length in system 2 is $\frac{l\Delta l}{l^2+w^2}$. This is explained as follows,

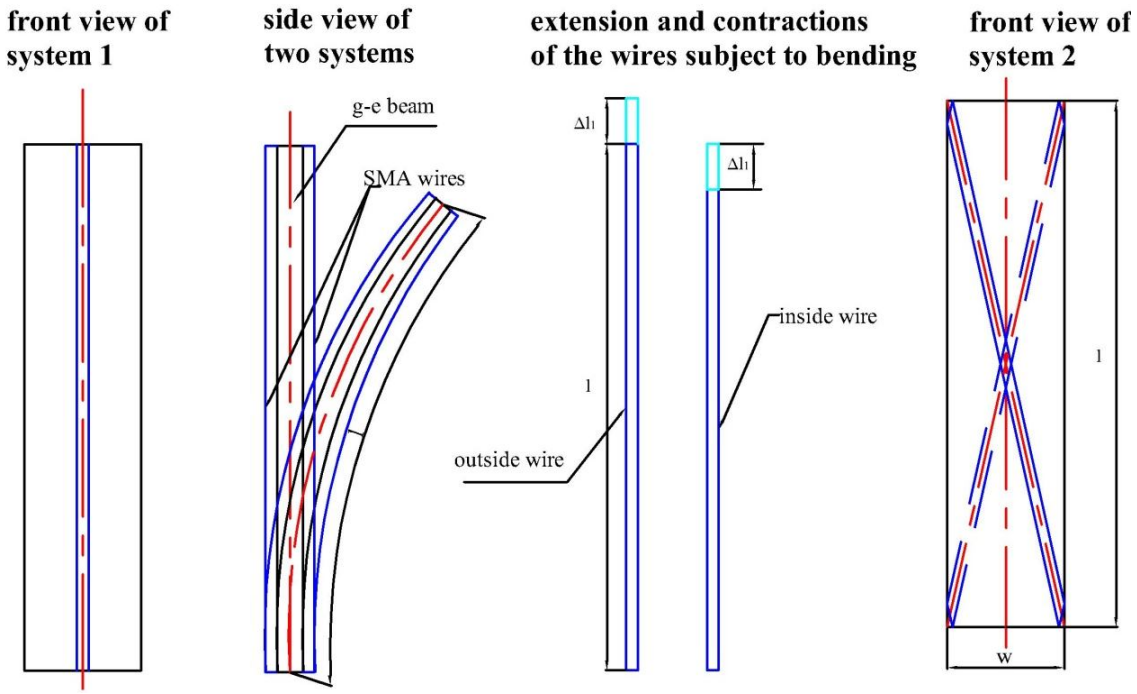

Fig 7-5 Geometrical changes in the SMA strips in system 1 and 2 when the beam bends

The extension per length of the outside strip in system 2 is

$$\frac{\sqrt{(l+\Delta l)^2+w^2}-\sqrt{l^2+w^2}}{\sqrt{l^2+w^2}} \tag{1}$$

Expanding the sum quadratic part and moving out the term $1/\sqrt{l^2+w^2}$ yields

$$\frac{1}{\sqrt{l^2+w^2}}\left(\sqrt{l^2+w^2+2l\Delta l+(\Delta l)^2}-\sqrt{l^2+w^2}\right) \tag{2}$$

Further manipulation gives

$$\frac{1}{\sqrt{l^2+w^2}}\left(\sqrt{l^2+w^2}\sqrt{1+\frac{2l\Delta l}{l^2+w^2}+\frac{(\Delta l)^2}{l^2+w^2}}-\sqrt{l^2+w^2}\right) \tag{3}$$

$(\Delta l)^2 / (l^2 + w^2)$ is very small, so neglecting it and cancelling $\sqrt{l^2 + w^2}$ leads to

$$\sqrt{1 + \frac{2l\Delta l}{l^2 + w^2}} - 1 \tag{4}$$

Because $\frac{2l\Delta l}{l^2 + w^2}$ is also very small, the expression $\sqrt{1 + \frac{2l\Delta l}{l^2 + w^2}}$ can be expanded by using the Binomial Theorem. After some modification, the final result is

$$\frac{l\Delta l}{l^2 + w^2} \tag{5}$$

When $w = 0$, the expression (5) becomes $\frac{\Delta l}{l}$. That is the case of system 2, which gives a good check of the above method.

The contraction of the inside strip per length is also $\frac{l\Delta l}{l^2 + w^2}$. It can be seen that in system 2, i.e. the diagonal-strip case, for the same bending of the beam the extension and compression strains are less than those for the central-strip case of system 1. Consequently, the composite beam in the diagonal-strip case is less stiff and therefore has a lower natural frequency in bending. For the torsional mode, the diagonal-strip case makes the beam difficult to twist and therefore increases the natural frequency in torsion.

(4) For both the central-strip and diagonal-strip cases, as the temperatures increase the frequencies of the first bending, the first torsion, and the second bending modes all decrease**.** The following offers a likely explanation: as seen in the laboratory, the strips broke away from the g-e beam when the temperature was increased over 45°C. Because both 30°C and 40°C were below the transition temperature 75°C, the SMA strips didn't show large variation in Young's modulus due to phase transformation, only a stiffening effect of the two systems. The strips become softer and less stiff when the temperature increases, thus resulting in the decrease of the natural frequencies. The system where the length of the end mass is 70 mm is taken as an example, Figures 7-6, 7 and 8 show how the temperature affects the frequencies.

(5) As the length of the end masses increase, the natural frequencies of the first, second bending and the first torsion modes all decrease. It is because that when the length of the end masses is increased, the corresponding masses and the mass moment of inertia about the y-axis increase, as shown in Figures 7-9 and 10.

(6) As for the 40°C case, when the length of the end mass is 50 mm, 60 mm, 70mm and 80 mm, the frequencies of the 1st torsion mode of their corresponding systems have been missed. It was noticed in the lab that at 40°C, the SMA strips appeared to partially de-bonded from the beam. It may be the reason why the observable torsion mode responses were prevented.

	without-strip	with strips					
		Central-strip			diagonal-strip		
		20°C	30°C	40°C	20°C	30°C	40°C
f_1(Hz)-1st bending	7.44	25.34	23.66	21.35	22.03	21.53	21.18
f_2(Hz)-1st torsion	27.07	39.44	36.25	31.88	41.92	38.97	36.53
f_3(Hz)-2nd bending	177.5	476.79	458.73	421.81	336.86	333.05	330.81

Table 7-4 Experimental results when the length of the end mass is 70mm

Frequency / L of the EM(mm)	f_1(Hz)	f_2(Hz)	f_3(Hz)
50	30.34	68.24	445.29
60	28.29	51.63	381.21
70	22.04	41.28	336.86
80	20.86	32.37	286.52
100	19.33	23.74	221.17

Table 7-5 Effect of the end mass length on the natural frequencies of the first bending, torsion and the second bending modes (20°C case)

Frequency / L of the EM(mm)	f_1(Hz)	f_2(Hz)	f_3(Hz)
50	29.52	64.43	433.16
60	28.12	48.76	377.48
70	21.53	38.97	333.05
80	20.62	30.99	282.92
100	18.89	22.43	216.8

Table 7-6 Effect of the end mass length on the natural frequencies of the first bending, torsion and the second bending modes (30°C case)

Frequency / L of the EM(mm)	f_1(Hz)	f_2(Hz)	f_3(Hz)
50	29.27		429.78
60	27.62		377.49
70	21.18		330.81
80	20.02		279.07
100	18.3	20.46	212.75

Table 7-7 Effect of the end mass length on the natural frequencies of the first bending, torsion and the second bending modes (40°C case)

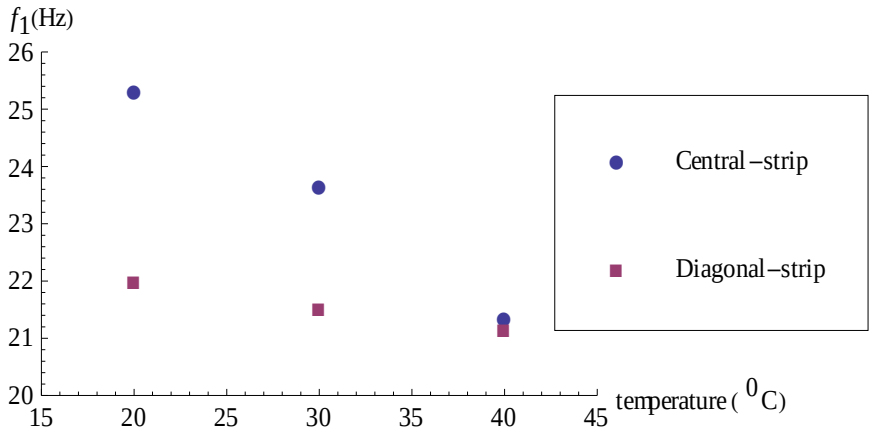

Fig 7-6 Effect of temperature on the natural frequency of the first bending mode

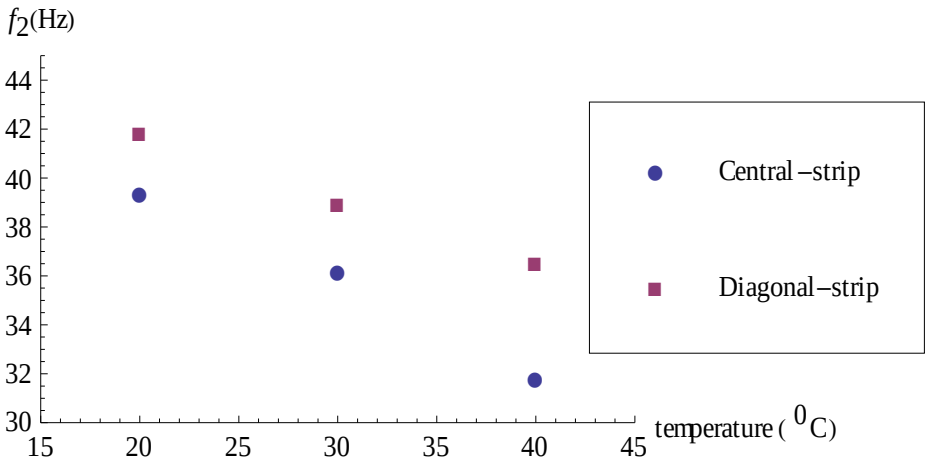

Fig 7-7 Effect of temperature on the natural frequency of the first torsion mode

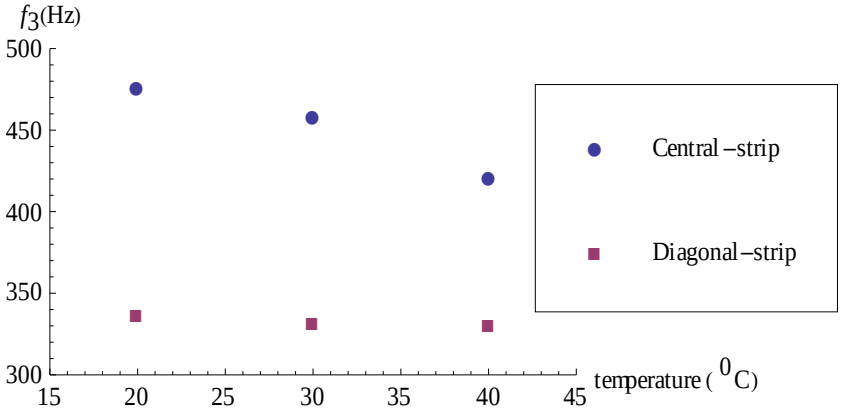

Fig 7-8 Effect of temperature on the natural frequency of the second bending mode

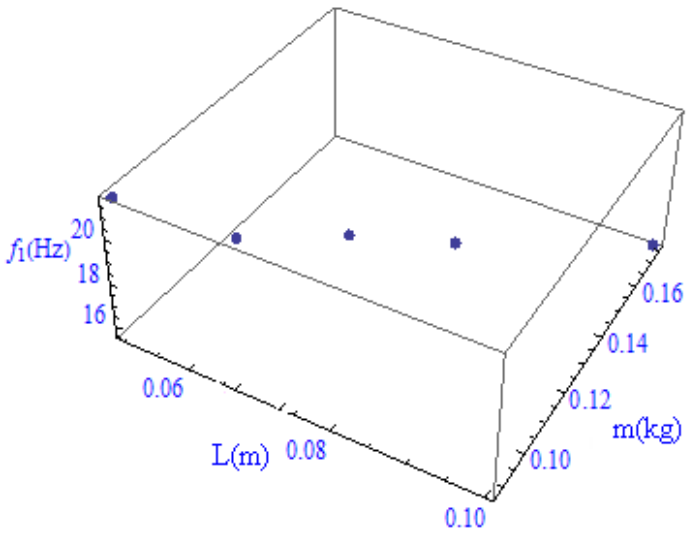

Fig 7-9 Natural frequency of the first bending mode against the length of the end masses and the corresponding masses

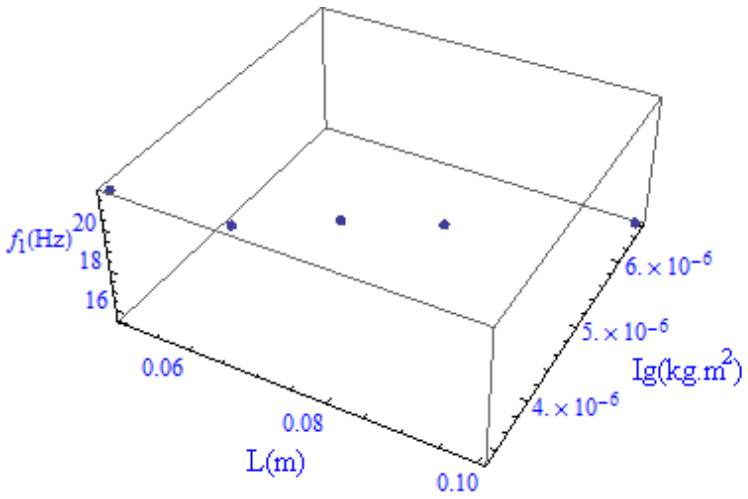

Fig 7-10 Natural frequency of the first bending mode against the length of the end masses and the corresponding mass moment of inertia

As seen from Table 7-4, the natural frequency of the first bending mode being taken as an example, f_1 is increased dramatically from 7.44 Hz in the without-strip case to 25.34 Hz in the central-strip case, which is over three times bigger. This means the SMA strips has dominated the composite beam system, not just acting as a means of changing the properties of the beam as expected. It was also noticed that the strips could not be heated up to A_f in this case, therefore, the strips have not been activated to exhibit either their shape memory effect or pseudo-elasticity. So two new SMA strips were purchased with lower A_f, and dimensionally thinner, to avoid the problem in which the SMA strips dominate the properties of the composite beam structure. The properties of the new SMA strips are listed in Table 7-8.

Chemical composition	Ni 55.49 [wt-%], Ti bal [wt-%], C 310[ppm], O 185[ppm]
Trans. temp[°C]	A_f: 30 °C
Thickness	0.5 mm
Width	2.0 mm

Table 7-8 Properties of the new Ni-Ti strips

7.2 Testing of the SMA Strips

7.2.1 Cycling Test

To make sure of repeatable performance, the two SMA strips were subjected to thermomechanical cycling before any further tests. To cycle them, a material testing machine, Zwick Roell Z250 was used. Each strip was fixed on the grips of the machine and tensile tests were carried out. The force-displacement curves were generated through a textXpert software also provided by the Zwick Roell company as shown in Figure 7-11. The two strips were plastically deformed, seen from Figure 7-12 and then unloaded and electrically heated to its austenite finish temperature to recover the deformation. The temperature was controlled by regulating the electrical current supplied to the strip and monitored using a thermocouple. Extending the strips and then heating them above their A_f constitute one cycle. This test was repeated 10 times and each time the strips could successfully go back to their original length. It showed they had good repeatable performance.

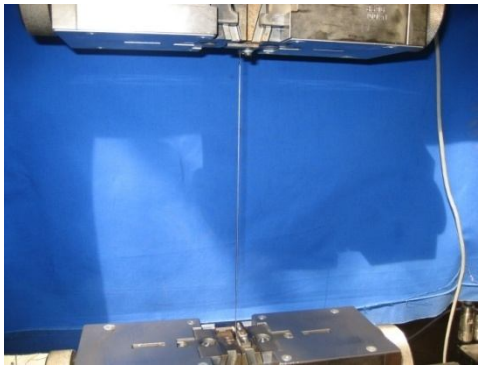

Fig 7-11 Extension set-up of the strips

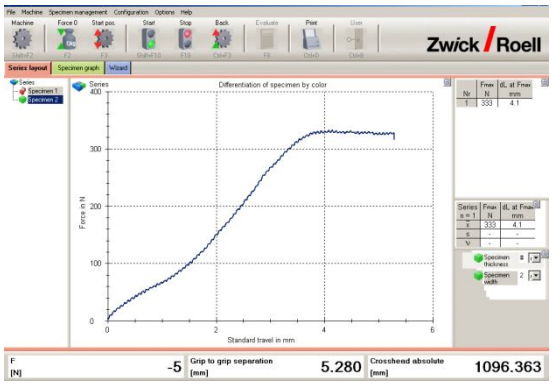

Fig 7-12 Force-displacement curve of the strips

7.2.2 Young's Modulus Test

To compare the Young's moduli of the martensite and austenite phases of the SMA strips at different temperatures, loading and unloading tests needed to be carried out. A simple test set-up was designed and built as Figure 7-13. The strip was clamped at one end and loaded by suspending a weight from the other end thereby deforming it. The displacement was measure by means of a dial gauge. A load-displacement line was drawn when the

suspending weight was varied, and its corresponding extension was recorded. The test was conducted at two temperatures, room temperature, 20°C when the tests were conducted, and the transformation temperature around 30°C in this case. To get the higher temperature of 30°C, the strip was heated by passing a constant electrical current, as shown in Figure 7-14. The two clamps were made from Teflon to insulate the strips from the current. The temperature was measured by a thermocouple. The temperature needed to be a bit higher than 30°C to ensure the whole strip stayed fully in the austenite phase, however not at too high a level in order to avoid thermal expansion. To choose a suitable current to reach 30°C , a few temperature-time history curves were made at different current levels as shown in Table 7-9, and then a current of 1.95 A was chosen. At a constant temperature of 32°C the loading test was performed for the strip staying completely in the austenite phase.

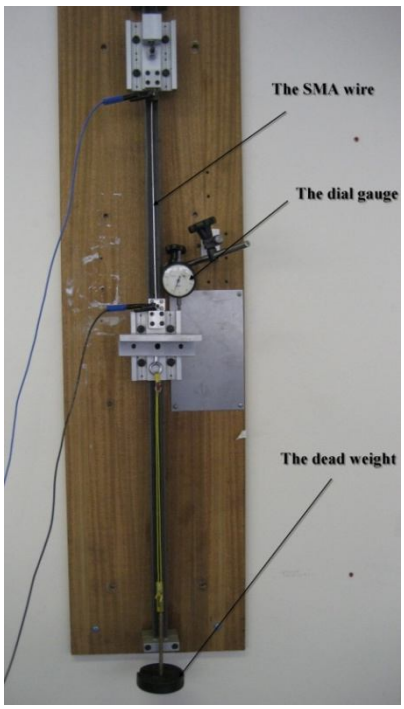

Fig 7-13 Test rig for force-displacement experiments

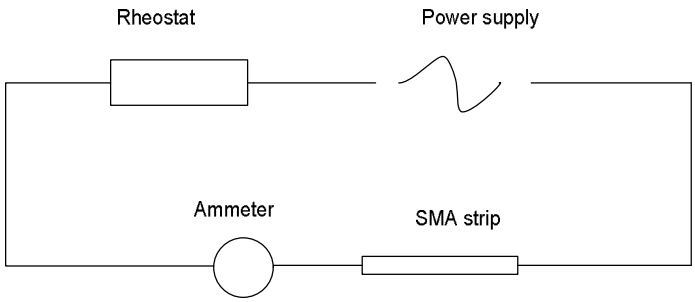

Fig 7-14 Current circuit

Current (A)	Starting temperature(^{0}C)	Starting temperature(^{0}C)	Duration (min)
1.23	19	26	6
1.57	19	30	6
1.95	19	32	6
2.31	20	43	6

Table 7-9 Temperature against electrical current in force-displacement tests when the strips are activated

In this test five different loadings were applied and their corresponding extensions were recorded. The loadings were converted to stress divided by the cross-section area of the strip ($\sigma = F / A$), and extensions to strain divided by the original length ($\varepsilon = l / l_0$). The strain-stress curves for both phases are shown in Figures 7-15 and 7-16. They are almost linear, thus conforming elastic deformations. The Young's moduli were calculated to be 16.68 GPa for the martensite phase, and 51.998 GPa for the austenite phase, which is 3.12 times more than that for the martensite phase. The results might be smaller than the actual values. This is due to the fact that the displacements were measured over the whole strip length. If the fixed end of the strip move downward, the displacements measured would be smaller than the real ones, thus making the Young's moduli smaller.

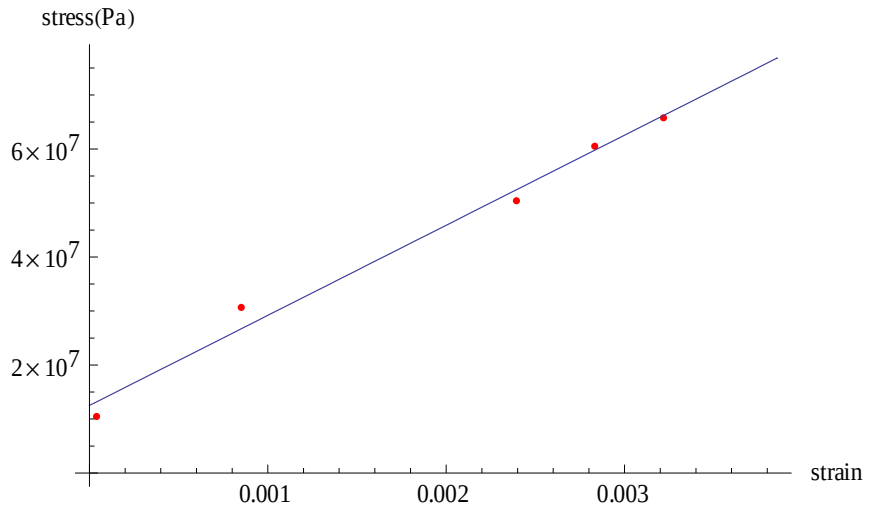

Fig 7-15 Strain-stress curve for the martensite phase

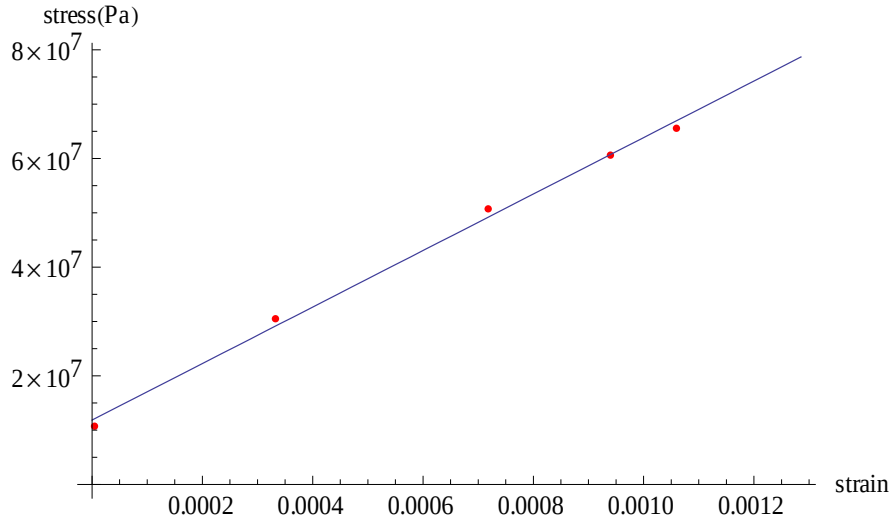

Fig 7-16 Strain-stress curve for the austenite phase

7.3 Experimental Investigations into Parametric Vibration

The bending responses of system 1 and 2 under an initial condition by means of a transient excitation were monitored by a laser vibrometer. A vibrometer control unit connected to the vibrometer passed the response signals to an analogue spectrum analyzer. The natural frequencies were calculated by means of a FFT within this spectrum analyzer, and displayed as a linear frequency response plot, and identified by using a screen cursor. The obtained natural frequency was used to calculate the Young's modulus of the g-e beam. The g-e beam was then marked at both ends to make sure the fixed and free ends always stayed the same in the following tests. Both system 1 and 2 were set up and the strips were heated up by using the simple electrical circuit in Figure 7-17. One end of the SMA strips was fixed by two

clamps made of hard plastic in order to be insulated. The temperatures were measured by a thermocouple at four points along the SMA length. Likewise the natural frequencies were measured when the SMA strips were unactivated and activated. Their corresponding damping ratios were obtained by using the logarithmic decrement method. The procedure to get the experimental points of the transition curve for when $\Omega \approx 2\omega_1$ was the same as that described in Chapter 3. That was, one selected a range of frequencies on the function generator, then gradually increased the excitation level, and recorded each excitation amplitude-frequency point once nonplanar motion was observed. The results are shown in Figure 7-18 and 7-19 when the strips were activated and un-activated for both systems 1 and 2.

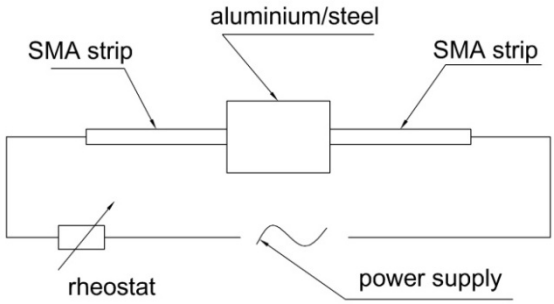

Fig 7-17 Electrical circuit

Table 7-10 lists all the natural frequencies of the fundamental bending mode and the damping ratios for both systems 1 and 2 when the SMA strips were activated and unactivated. The Young's modulus used in the theoretical calculations for martensite was acquired from the experiment shown in Figure 7-12, 32.23 GPa. This is because when this value was used to calculate the natural frequency of the first bending by means of $f = (\beta / l)^2 * \sqrt{EI_y / \rho A}) / 2\pi$ combining the boundary conditions explained in **Appendix 1** , the theoretical value of 6.4 Hz is the same as that from the experiment, seen from Table 7-10. The ratio of Young's modulus of austenite to martensite of 3.12, calculated from the experiments shown in Figure 7-13 is close to the generally accepted value, 3 (Liang and Rogers, 1990). Therefore this ratio was adopted and the Young's modulus for austenite then became 100.56 GPa, which was used for the following analysis in this chapter. The important results from this experiment are below:

1. For both systems, the natural frequencies and the damping ratios are increased when the strips are activated. For system 1, the natural frequency is increased from 7.85 Hz to 8.2 Hz by 4.46%, and the damping ratio from 0.0092 to 0.0189, therefore by 105.4%. For system 2, the natural frequency is increased from 7.64 Hz to 8.03 Hz by 5.1%, which is higher than 4.46% in system 1, however the damping ratio from 0.0208 to 0.0162 is decreased by 22.1%.

2. It is noted that the natural frequencies did not change as significantly with the activation of the SMAs as the theoretical results predicted. As seen in Table 7-10, for system 1, the theoretical value is 10.052 Hz for the activated strips, much bigger than the value 8.2 Hz taken from the spectrum analyzer. This indicates that the Young's moduli in austenite phase is not increased much when the SMA strips are activated. If laboratory results are only considered, the natural frequency of the system 1 with unactivated SMAs is 7.85 Hz. When the SMAs were activated, the frequency becomes 8.2 Hz. In this case, the Young's modulus of the SMAs is increased by 25%. That is to say, the ratio of the Young's modulus of austenite to martensite is only about 1.25, much smaller than the normal ratio 3~4. However the results agrees with Carballo et al's finding in 1995. They conducted experimental investigations and showed that under dynamic conditions, the ratio of Young's modulus of austenite to martensite of NiTi wires could be only 1.1~1.3, much smaller than that in the static case. Tian and Wu (2002) also pointed out the that under different vibration frequencies, the modulus of austenite of some SMAs was just a little higher than that of martensite.

3. The results of the damping ratio changes in system 1 and 2 when the strips were activated and unactivated also show that the changes in system 1 and 2 are very different. The variation of damping ratio under dynamic conditions has been studied by Carballo et al. (1995) and Wu *et al* (1995), Tian and Wu (2002). The both studies showed that the damping had a maximum peak during heating and cooling. The phenomenon that a maximum peak appeared in the damping-temperature curve during both heating and cooling was also discussed by. Moreover, they found that the peak values were in proportion to the ramp rate and in reverse proportion to frequency. None of the above studies show that the peak values had dependency on the transformation temperatures of the SMA.

4. The dynamic Young's modulus and damping behaviour of SMAs need to be further investigated and so do their impacts on the dynamic properties of system 1 and 2.

5. Figure 7-18 and 7-19 show that more input energy is needed to promote the instability for both systems when the strips are activated. The minimum acceleration needed is increased from 23.28 m/s^2 to 78.48 m/s^2 for system 1, and from 19.6 m/s^2 to 35.7 m/s^2 for system 2. It is understandable when the activated strips increase the natural frequency of the fundamental bending mode and its damping ratio.

6. Figure 7-20 and 7-21 show that the offset of the transition curves for system 2 is not as great as that for system 1, when the SMA strips were activated. This shows that the configuration in system 1 affects the beam structure, related to its bending modes, more significantly than system 2.

7. During the process of the experiments to obtain the instability zones, it was observed that the electrical currents dropped rapidly during the beam's nonplane motion. For example, it could decrease from the start current, 2.2 A to around 1.09 A. The reason is likely to be the increase of the electrical resistance with an increase of the strain of the SMAs. (Furuya 1992, Airoldi 1997, Wu and Wang 1999) The variation of electrical resistance is also a function of temperature (Carballo 1995, Wu and Wang 1999). In the series of the transition curve experiments, each experiment normally last 10 minutes. During this span of the time, the temperature changes were noticed. The temperature measuring points along the beam are shown in Fig 7-22. The temperatures before and after the experiments are listed in Table 7-11.

8. There are other factors which might affect the results in some way:

- The alignment of the SMA strip: the two SMA strips might not be symmetrical or shifting away from the central lines of both sides of the beam.
- The adhesive: the adhesive needs about 10 hours to cure, after one experiment and before the next, the adhesive should be removed completely from the beam without damaging the beam. However, it was very difficult to remove all the adhesive. The proper way to remove the adhesive is to use a blunt knife to remove the thick layers of

the glue, carefully, not to peel the beam surface, then to use different grades glass paper to scrape it off thoroughly.

- It is necessary to make sure every part of the SMA strips is tightly attached to the beam.
- How much adhesive is used in the experiments is not clear and the amount of adhesive used along the whole length might be different.

Systems			Natural frequency (Hz)	Damping ratio
System 1	With unactivated SMAs	Theoretical Calculation	7.699	
		Experimental Results	7.85	0.0092
	With activated SMAs	Theoretical Calculation	10.05	
		Experimental Results	8.2	0.0189
	Without SMAs	Theoretical Calculation	6.4	
		Experimental Results	6.4	0.0071
System 2	With unactivated SMAs		7.64	0.0208
	With activated SMAs		8.03	0.0162

Table 7-10 Natural frequencies and damping ratios of the first bending mode of system 1 and 2

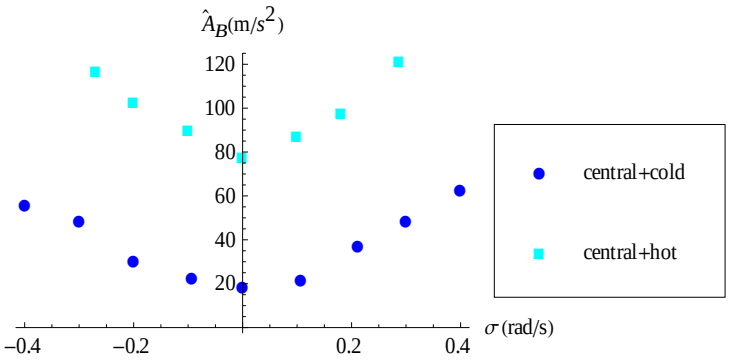

Fig 7-18 Transition curves when $\Omega \approx 2\omega_1$ with activated and unactivated SMA strips of system 1

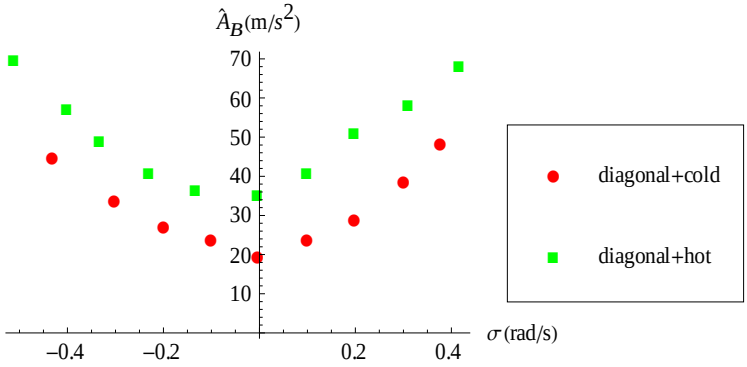

Fig 7-19 Transition curves when $\Omega \approx 2\omega_1$ with activated and unactivated SMA strips of system 2

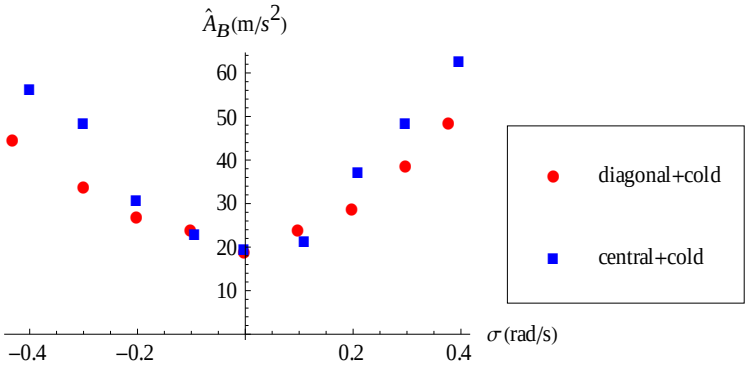

Fig 7-20 Comparisons of transition curves between the two systems when the strips are unactivated.

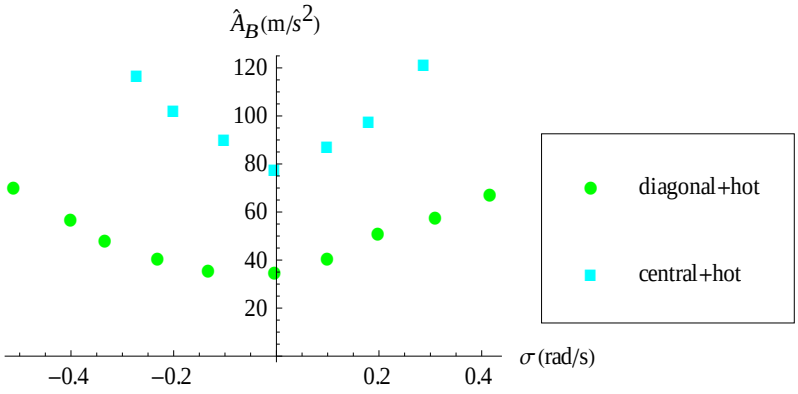

Fig 7-21 Comparisons of transition curves between the two systems when the strips are activated.

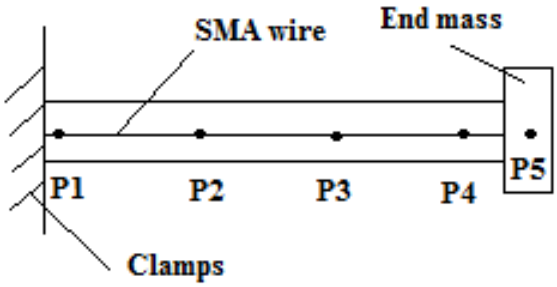

Fig 7-22 Temperature measuring points

Measuring positions	P_1	P_2	P_3	P_4	P_5
Before the experiment	30°C	30°C	30°C	30°C	28°C
After the experiment	30°C	34°C	40°C	43°C	58°C

Table 7-11 Temperatures of the SMA strips when the experiments on the transition curves were carried out.

Chapter 8

Conclusions and Future Recommendations

8.1 General Discussions

The research described within this thesis has been concerned with the effect of two centrally-bonded shape memory alloy strips on the dynamic properties of a glass epoxy beam carrying a lumped end mass under a parametric excitation. As a precursor to this investigation, a flexible steel beam with an end mass under a parametric excitation was studied theoretically and experimentally. The equations of motion for three degrees of freedom have been derived based on the mathematical model developed by Cartmell (1990) and Forehand and Cartmell (2001). The nonlinear, coupled differential equations were then analysed by the Multiple Scales perturbation method up to second order expansion as a means of predicting different parametric resonances and obtaining expressions to describe the corresponding transition curves. Before these analyse, a proposal for perturbation ordering of a linear coupling term was presented. This linear term was placed at higher order on the grounds of appropriate numerical calculations, noting that the ordering scheme strongly depended on the geometry of the beam and the end mass.

The influence of two centrally-bonded SMA strips on a dynamic properties of a flexible g-e beam with an end mass was explored. The SMA was used in both the APT and ASET regimes. With the APT method, theoretical evaluations of the natural frequencies of the bending modes were proposed. The influence of factors such as the width and thickness of the strips and the Young's modulus changes in the strips, on the dynamic properties of the composite beam structure have been studied. With the ASET method, a theoretical model for evaluating the natural frequencies and the bending modes of the composite beam structure was introduced. The model considered the recovery forces, generated in the pre-strained SMA strips when they were activated, as compressive forces. How the force affected the composite beam structure was also investigated.

When the ASET method was used, the dynamic responses of the composite beam system under vertical excitation were investigated. Intending to use the Lagrangian formulation, the author derived three generalised forces of the recovery force, corresponding to the three

modal coordinates of interest, lateral displacements u_1, u_2 and a twist angle ϕ_1. It was proceeded first by examining the force direction vector in terms of u_1, u_2 and ϕ_1 in three-dimension space, then to describe the generalised forces by using the Principal of Virtual Work. The governing equations of motion were solved by means of application of the multiple scales method, and different parametric resonances have been studied, along with the influence of the force on the resonances.

An experimental study was carried out on two composite beam systems, one with two centrally-bonded strips and the other with two diagonally-bonded strips. Hammer impact tests were first conducted for both cases. The natural frequencies of the fundamental, second bending modes and the fundamental torsion mode were measured and the effect of the temperatures and the end mass were observed. By measuring the first vibration mode, the dynamic mechanical properties of both cases were investigated.

8.2 Conclusions

Three parametric resonances of the form $\Omega \approx 2\omega_1, \Omega \approx 2\omega_2$ and $\Omega \approx \omega_1 + \omega_2$ involving the fundamental and second bending modes have been predicted when the equations are expanded to first order by the method of multiple scales. Experimental results agreed well with the theoretical predictions of three possible resonance conditions. Laboratory tests confirmed that these instabilities were bounded in practice by nonlinear effects.

By solving a second order perturbation equations, many other theoretical resonance conditions have been shown to be potentially capable of producing nonzero solutions, and these resonances were seen to be composed of various combinations of modal frequencies.

In theory, with the APT method, the natural frequencies of the flexible g-e beam with an end mass and two centrally-bonded SMA strips were increased when the strips were activated. The natural frequency were also increased by increasing the width and thickness of the strips, and the frequency changes were more sensitive to the thickness changes rather than the width.

With the ASET method, the analytical prediction showed that the natural frequencies decreased when the activation forces were increased. Increasing the forces resulted in the

reducing the excursion of the first and second bending modes. The model predicted that the composite beam buckled more easily under dynamic loading than under static loading. The theoretical results also showed that the instability regions were increased as the magnitude of the recovery forces increased.

Experimentally, with the APT method for both the centrally-bonded and diagonally-bonded cases, the natural frequencies of the bending modes increased when the SMA strips were activated. It was also observed that the instability regions of the $\Omega \approx 2\omega_1$ resonance were decreased when the strips were activated. The increment of the natural frequencies of the bending modes were more in the centrally-bonded case than those in the diagonally-bonded case. However, the diagonal-strip configuration could easily change the natural frequencies of the torsion modes than the central-strip one.

The measured values of the natural frequencies in the centrally-bonded case through the experiments were lower than those predicted by the theoretical calculations. This is likely to be that when the strips were activated, the Young's modulus in austenite phase under dynamic conditions, was not increased as much as that in the static case on which the theoretical results were based (Carballo *et al* 1995, Tian and Wu 2002).

The damping ratio was increased in the centrally-bonded case when the strips were activated, however the trend was reversed in the diagonally-bonded case. This unusual phenomenon could be because the damping properties did not monotonically increase when the temperature of the strips increased under dynamic conditions (Carballo *et al* 1995, Wu *et al* 1995).

The drop in the electrical resistance of the SMA strips was also observed when the composite beam was in its nonplane motion. The reason is likely to be the increase of the electrical resistance with an increase of the strain of the SMAs, explained by Furuya 1992, Airoldi 1997, Wu and Wang 1999.

8.3 Future Recommendations

- There is scope for further investigations into the variation of Young's modulus, damping properties and electrical resistance of the SMA strips corresponding to the

change of temperature and the ramp rate, when the beam structure is under vertical excitation.

- When the Active Strain Energy Tuning (ASET) method is utilised, in the centrally-bonded case, the SMA strips generate high recovery force as well as changes in their stiffness during their activation. However, in this study, the recovery force decreases the stiffness of the composite beam structure at the same time. Therefore it would be interesting to find out an optimum way for controlling the dynamic characteristics of the beam structure with application of ASET technique.
- A study of the underlying mechanisms of tuning the dynamic characteristics of parametric and autoparametric beam structures where the resonance conditions involve torsion modes would be advantageous when the diagonally-bonded SMA strips are used, because the diagonal SMA strips can modify the properties of torsion modes easily and can introduce a torsion moment into the system, when the ASET method is utilised.

Reference

Acheson, D., and Mullin, T. (1993). Upside-down pendulums. *Nature*, 366, 215-216.

Airoldi, G., Pozzi, M., and Riva, G. (1997). The electrical resistance properties of shape memory alloys. *Material Research Society Symp. Proc.* (Materials Research Society), 459-464.

Anderson, G. L. (1975). The method of averaging applied to a damped, non-linear systems under harmonic excitation. *Journal of Sound and Vibration,* 40 (2), 219-225.

Ashton, J. O. E., Halpin, J. C., and Petti, P. H. (1969). Primer on Composite Materials: Analysis, Technomic, Stamford, Conn.

Barr, A. D. S. (1980). Some developments in parametric stability and nonlinear vibration. *Recent Advances in Structural Dynamics,* 2, *545-567.*

Basu, B., and ASCE, M. (2007). Nonlinear oscillations of vehicle tires with Hertzian Contact. *Journal of Aerospace Engineering,* 20(1), 72-74.

Baz, A., Chen, T., and Ro, J. (2000). Shape control of Nitinol-reinforced composite beams, *Composites Part B: Engineering,* 31(8), 631-642.

Baz, A., Iman, K., and McCoy, J. (1990). Active vibration control of flexible beams using shape memory actuators. *Journal of Sound and Vibration,* 143 (3), 437-456.

Baz, A., Poh, S., and Ro, J. (1995). Control of the natural frequencies of Nitinol-reinforced composite beams. *Journal of Sound and Vibration,* 185(1), 171-185.

Benjamin, T. B., and Ursell, F. (1954). The stability of a plane free surface of a liquid in a vertical periodic motion. *Proceedings of the Royal Society of London. Series A, Mathematical and Physical Sciences,* 225(1163), 505-515.

Brinson, L. C. (1993). One-dimensional constitutive behaviour of shape memory alloys: thermomechanical derivation with non-constant material functions. *Journal of Intelligent Material Systems and Structures,* 4, 229-242.

Bolotin, V. V. (1964). *Dynamic stability of elastic systems.* Holden Day, San Francisco.

Bondarev, P. A. (1970). Applicability of the method of averaging for investigations of nonlinear vibrations of rectangular plates. *Ukrainian Mathematical Journal,* 22(5), 575-578.

Boyd, J. G., and Lagoudas, D. C. (1996). A thermodynamical constitutive model for shape memory materials: part 1. The monolithic shape memory alloy. *International Journal of Plasticity,* 12, 805-842.

Buehler, W. J., and Wiley, R. C. (1965). Nickle-based alloys, US Patent 3 174 851.

Cai, Ming, Liu, Ji-ke, and Li, Jun. (2006). Incremental harmonic balance method for airfoil flutter with multiple strong nonlinearities. *Applied mathematics and Mechanics,* 27(7), 953-958.

Carbollo, M., Pu, Z. J., and Wu, K. H. (1995). Variation of Electrical Resistance and the Elastic Modulus of Shape Memory Alloys under Different Loading and Temperature Conditions. *Journal of Intelligent Material Systems and Structures*, 6, 557-565.

Cartmell, M. P. (1990). *Introduction to linear, parametric and nonlinear vibrations.* London: Chapman and Hall.

Cartmell, M. P. (1990). The equations of motion for a parametrically excited cantilever beam. *Journal of Sound and Vibration,* 143 (3), 395-406.

Cartmell, M. P., and Roberts, J. W. (1987). Simultaneous Combination Resonances in a Parametrically Excited Cantilever Beam. *Strain*, 23 (3), 117-126.

Cartmell, M. P., and Roberts, J. W. (1998). Simultaneous combination resonances in an autoparametrically resonant system. *Journal of Sound and Vibration,* 123 (1), 81-101.

Cartmell, M. P., and Wiercigroch, M. (2003). Control of Vibration by Smart SMA-Embedded Composite Structures. Individual Grant Review - GR/N06267/01, EPSRC, August.

Cartmell M. P., Ziegler, S. W., Khanin, R. and Forehand D. I. M., (2003). Multiple Scales Analysis of the Dynamics of Weakly Nonlinear Mechanical Systems. *Applied Mechanics Review*, 56 (5), 455-492.

Champneys, A. R., and Fraser, W. B. (2000). The “Indian rope trick” for a parametrically excited flexible rod: linearized analysis. *Proceedings of Royal Society of London.* A 456, 553-570.

Chaudhry, Z., and Rogers, C. A. (1991). Bending and shape control of beams using SMA actuators. *Journal of Intelligent Material Systems and Structures,* 2(4), 581-602.

Chen, Q., and Levy, C. (1996). Active vibration control of elastic beam by means of shape memory alloy layers. *Smart Materials and Structures,* 5, 400-406.

Cheung, Y. K., Chen, S. H., and Lau, S. L. (1990). Application of the incremental harmonic balance method to cubic non-linearity systems. *Journal of Sound and Vibration,* 140 (2), 273-286.

Chivavibul, P., Enoki, M., and Kagawa, K. (2003). Effect of gage length on tensile strength and failure strain of woven fabric Al2O3 fiber-ZrO2 minicomposite-reinforced Al2O3 matrix composite. *JOURNAL OF MATERIAL SCIENCE LETTERS,* 22, 295-498.

Cicek, I., and Ertas, A. (2002). Experimental investigation of beam-tip mass and pendulum system under random excitation. *Mechanical Systems and Signal Processing,* 16 (6), 1059-1072.

Coppola, V. T. (1997). The method of averaging for Euler’s equations of rigid body motion. *Nonlinear Dynamics,* 14, 295-308.

Dugundji, J., and Mukhopadhyay, V. (1973). Lateral bending-torsion vibrations of a thin beam under parametric excitation. *Journal of Applied Mechanics,* 40, 693-698.

Epps, J. J. and Chandra, R. (1997). Shape memory alloy actuation for active tuning of composite beams. *Smart Materials and Structures,* 6, 251-64.

Evenson, H. A., and Evan-Iwanowski, R. M. (1966). Effect of longitudinal inertia upon the parametric response of elastic columns. *Journal of Applied Mechanics,* 33(1), 141-148.

Faraday, M. (1831). On the forms and states assumed by fluids in contact with vibrating elastic surfaces. *Philosophical Transactions of the Royal Society,* 121, 329-346.

Forehand, D. I. M., and Cartmell, M. P. (2001). On the Derivation of the Equations of Motion for a Parametrically Excited Cantilever Beam. *Journal of Sound and Vibration,* 245 (1), 165-177.

Fuller, C. R., Elliott, S. J., and Nelson, P. A. (1996). *Active Control of Vibration*. London: Academic Press Ltd.

Furuya, Y. (1992). *Mechanical Research*, 10, 1090-1096.

Gandhi, F., and Chapuis, G. (2002). Passive damping augmentation of a vibrating beam using pseudoelastic shape memory alloy wires. *Journal of Sound and Vibration,* 250 (3), 519-539.

Halpin, J. C., and Kardos, J. L. (1976). The Halpin-Tsai Equations: A Review. *Polymer Engineering and Science,* 16(5), 344-352.

Hamdan, M. N. (1990). On the primary frequency response of strongly non-linear oscillators: A linearization approach. *Journal of Sound and Vibration,* 140 (1), 1-12.

Handoo, K. L., and Sundararajan, V. (1971). Parametric instability of a cantilevered columna with end mass. *Journal of Sound and Vibration,* 18(1), 45-53.

Ibrahim, R. A. (1978). Parametric vibration Part III: Current problems (1). *Shock and Vibration,* Digest 10, 3, 41-57.

Ibrahim, R. A., and Barr, A. D. S. (1978). Parametric vibration Part I: Mechanics of linear problems. *Shock and Vibration,* Digest 10, 1, 15-29.

Ibrahim, R. A., and Barr, A. D. S. (1978). Parametric vibration Part II: Mechanics of nonlinear problems. *Shock and Vibration,* Digest 10, 2, 9-24.

Ibrahim, R. A., and Hijawi, M. (1998). Deterministic and Stochastic Response of Nonlinear Coupled Bending-Torsion Modes in a Cantilever Beam. *Nonlinear Dynamics,* 16, 259-292.

Icardi, U. (2001). Large bending actuator made with SMA contractile wires: theory, numerical simulation and experiments. *Composites Part B: Engineering,* 32(3), 259-267.

Jones, R. M. (1998). *MECHANICS OF COMPOSITE MATERIALS.* Second Edition. PA: Taylor and Francis, Inc.

Kang, Ki-Weon, and Kim, Jung-kyu. (2009). Effect of shape memory alloy on impact damage behaviour and residual properties of glass/epoxy laminates under low temperature. *Composite Structures*, 88(3), 455-460.

Kovalenko, K. P. (1958). The effects of internal and external frictions on the dynamic stability of bars. *PMM,* 23, 345-358.

Lagoudas, D. C., and Tadjbakhsh, I. G. (1993). Deformations of active flexible rods with embedded line actuators. *Smart Materials and Structures,* 2, 71-81.

Lau, KT. (2002).Vibration characteristics of SMA composite beams with different boundary conditions. *Materials and Design,* 23, 741-749.

Lee, H. J., and Lee, J. J. (2000). A numerical analysis of the buckling and post-buckling behaviour of laminated composite shells with embedded shape memory alloy wire actuators. *Journal of Smart Material Structures,* 9, 780-787.

Lee, Seung-Chul, Jeong, Seong-Taek, Park, Jong-Nam, Kim, Sun jin, and Cho, Gyu-Jae. (2008). A study on mechanical properties of carbon fibre reinforced plastics by three-point bending testing and transverse static response. *Journal of Materials Processing,* 201, 761-764.

Leven, R. W., and Koch, B. P. (1981). Chaotic behaviour of a parametrically excited damped pendulum. *Physics Letters,* 86A, 71-74.

Liang, C., and Rogers, C. A. (1990). One-dimensional thermomechanical constitutive relations for shape memory material. *Journal of Intelligent Material Systems and Structures,* 1, 207-234.

Lord, Rayleigh (Strutt, J. W.) (1892). On the instability of cylindrical fluid surfaces. Collected papers, Cambridge University Press, 3, 594.

Love, A. E. H. (1944). *A Treatise on the Mathematical Theory of Elasticity.* Fourth Edition. New York: Dover Publications.

Lowery, R. (2007). Glass epoxy composite has the right stuff for vital space mission. *Reinforced Plastics,* 51(3), 52-54.

Lu, T. J., Hutchinson, J. W., and Evans, A. G. (2001). Optimal design of a flexural actuator. *Journal of the Mechanics and Physics of Solids,* 49, 2071-2093.

Magrab, E. B. (1979). Vibrations of Elastic Structural Members. The Netherlands: Sijthoff and Noordhoff International Publicating Co.

Mahmood, M., Shokrieh, M., and Jamal, O. (2009). Tension behaviour of unidirectional glass/epoxy composites under different strain rates. *Composite Structures*, 88, 595-601.

Mallick, P. K. (1993). *Fiber-Reinforced Composites; Materials, Manufacturing, and Design.* Second Edition. New York: Marcel Dekker, Inc.

Maple, R. C. (2002). Adaptive Harmonic Balance Method for Unsteady, Nonlinear, One-dimensional Periodic Flows. Dissertation. Air Force Institute of Technology.

Melde, F. (1859). Uber Erregung Stehender Wellen Eines Fadenformigen Korpers. *Annals of Physics and Chemistry,* 109, 193-215.

Meo, M., Antonucci, E., Duclaux, P., and Giordano, M. (2005). Finite element simulation of low velocity impact on shape memory alloy composite plates. *Composite Structures,* 71, 337-342.

Miles, J. (1985). Parametric excitation of an internally resonant double pendulum. *Journal of Applied Mathematical Physics,* 36, 337-345.

Murdock, J. A. (1991). *Perturbations: Theory and Methods*, John Wiley, New York.

Nayfeh, A. H. (1973). *Perturbation Methods.* New York: Wiley.

Nayfeh, A. H., and Mook, D.T. (1979). *Nonlinear Oscillations.* New York: Wiley.

Ness, D. J. (1971). Resonance classification in a cubic system. *Journal of Applied Mechanics,* 38, 585-590.

Otsuka, K., and Wayman, C. M**.** (1998). *Shape memory materials.* Cambridge: Cambridge University Press.

Pardinia, L. C., and Manhanib, L. G. B. (2002). Influence of the Testing Gage Length on the Strength, Young's Modulus and Weibull Modulus of Carbon Fibres and Glass Fibres. *Materials Research,* 5(4), 411-420.

Popov. E. P. (1978). *Mechanics of Materials*. 2nd edition, SI version. Englewood Cliffs; London: Prentice-Hall.

Raniecki, B., Lexcellent, C., and Tanaka, K. (1992). Thermomechanical models of pseudoelastic behaviour of shape memory alloys. *Archieves of Mechanics,* 44, 262-284.

Rao, S. S. (2003). *Mechanical Vibrations.* Fourth Edition. PEARSON Prentice Hall.

Rogers, C., Liang, C., and Barker, D. (1989). Behaviour of shape memory alloy reinforced composite plates (part I and II). Proc. 30th Structures, Structural Dynamics and Materials Conf.

Rogers, C. A., Liang, C., and Baker. D. K. (1989). Dynamic control concepts using shape memory alloy reinforced plates. Smart Materials, Structures, and Mathematical Issues, Technomic Publishing Company, Inc., 39-62.

Rogers, C. A., Baker, D. K., and Jaeger, C. A. (1989). Introduction to smart materials and structures. Smart materials, structures, and mathematical issues, Technomic Publishing Company, Inc; 17-28.

Shu, S. G., Lagoudas, D. C., Hughes, D., and Wen, J. T. (1997). Modelling of a flexible beam actuated by shape memory alloy wires. *Smart Materials and Structures,* 6, 265-277.

Singh, A., Mukherjee, R., Turner, K., and Shaw, S. (2005). MEMS implementation of axial and follower end mass. *Journal of Sound and Vibration,* 286(3), 637-644.

Tanaka, K. (1986). A thermomechanical sketch for shape memory effect: one-dimensional tensile behaviour. *Res Mechanica,* 18, 251-263.

Thompson, S. P., and Loughlan, J. (1997). Adaptive post-buckling response of carbon fibre composite plates employing SMA actuators. *Composite Structures,* 38(1-4), 667-678.

Thomsen, J. J. (1997). *Vibrations and Stability: Order and Chaos.* McGraw-Hill, Maidenhead.

Thomsen, J. J. (2003). *Vibrations and Stability: Advanced Theory, Analysis, and Tools.* Second Edition. Springer.

Tian, Q. C., and Wu, J. S. (2002). Dynamic properties of $Ti_{51}Pd_{30}Ni_{19}$ high-temperature shape memory alloy under different heat treatment conditions. *Scandinavian Journal of Metallurgy,* 31, 251-255.

Timoshenko, S. P., and Young, D.H. (1968). *Elements of Strength of Materials.* Fifth Edition. New York: Van Nostrand Reinhold.

Timoshenko, S. P., and Goodier, J.N. (1878). *Theory of Elasticity.* 2nd Edition. New York; London: McGraw-Hill.

Tse, F. S., Morse, I. E., and Hinkle, R. T. (1979). *Mechan*ical *Vibrations-Theory & Applications.* Second Edition. Boston, MA: Allyn & Bacon Inc.

University of Alberta smart material and micromachines website by SMA/MEMS Research Group. (2001). *http://www.cs.ualberta.ca/~database/MEMS/sma_mems/sma.html*

Veeramani, A. S., Buckner, G. D., Owen, S. B., Cook, R. C., and Bolotin, G. (2008). Modelling the dynamic behaviour of a shape memory alloy actuated catheter. *Smart Materials and Structures,* 17(1), 1-14.

Watt, D., and Cartmell, M. P. (1994). An externally loaded parametric oscillator. *Journal of Sound and Vibration,* 170(3), 339-364.

Wells, D. A. (1967). *Lagrangian Dynamics, Schuam's Outline Seriers.* New York: McGraw Hill.

Wolfram, S. (2008). Wolfram Mathematica 6.0.

Wu, K., Dalip, S. K., Liu, Y., and Pu, Z. (1995). Damping characteristics of R-phase NiTi shape memory alloys. Proc. Conf. on Smart Structures and Materials SPIE, 2441, 139.

Wu, X. D., Wu, J. S., and Wang, Z. (1999). The variation of electrical resistance of near stoichiometric NiTi during thermo-mechanic procedures. *Smart Materials and Structures,* 8, 574-578.

Zak, A. J., Cartmell, M. P., and Ostachowicz, W. M. (2003). A sensitivity analysis of the dynamic performance of a composite plate with shape memory alloy wires. *Composite structures,* 60(2), 145-157.

Zhang, Run-xin, Ni, Qing-Qing, Masuda, Arata, Yamamura, Takahiko, and Iwamoto, Masuharu. (2006). Vibration characteristics of laminated composite plates with embedded shape memory alloys. *Composite Structures,* 74, 389-398.

Zhang, Run-xin, Ni, Qing-Qing, Natsuki, Toshiaki, and Iwamoto, Masaharu. (2007). Mechanical properties of composites filled with SMA particles and short fibres. *Composite Structures,* 79, 90-96.

Zhang, Run-xin, Ni, Qing-Qing, Natsuki, oshiaki, and Iwamoto, Masaharu. (2007). Stiffness and vibration characteristics of SMA/ER3 composites with shape memory alloy short fibres. *Composite Structures,* 79, 501-507.

Zhang, W. Y., and Huseyin, K. (2001). Complex formulation of the IHB technique and its comparison with other methods. *Applied Mathematical Modelling,* 26(1), 53-75.

Publication

Su, X, and Cartmell, M.P. (2007). “Combination Resonance in a Vertically Orientated and Excited Cantilever Beam with an End Mass” the 2nd International Conference "NONLINEAR DYNAMICS", Kharkov, Ukraine, Sept. 25-28.

List of Figures in Appendices

List of Tables in Appendices

Table of Contents in Appendices

Appendix 1

Calculation of the Mode Shape Coefficients

A.1.1 Boundary Conditions at the Free End

Forehand and Cartemll (2001) have derived the boundary conditions for the free end of a cantilever beam with a lumped end mass. For clarification, the conditions are re-written here, which are also equations (29) and (30) in reference Forehand and Cartmell (2001).

$$EI_Y f'''(l) = -\omega^2 m_0 (f(l) + (l_0 - l) f'(l)) \tag{1}$$

$$-\omega^2 I_G f'(l) = -EI_Y (f''(l) + (l_0 - l) f'''(l)) \tag{2}$$

where ω is the natural frequency of the mode and $f(z)$ is the standard Euler- Bernoulli mode shape for a beam clamped at $z = 0$ ($u(0,t) = u'(0,t) = 0$). That is

$$f(z) = C_1(\sin\lambda z - \sinh\lambda z) + C_2(\cos\lambda z - \cosh\lambda z) \tag{3}$$

where $\lambda^4 = \dfrac{\omega^2 m}{EI_Y}$.

A.1.2 Mode Shape Coefficients Analysis

Upon using equation (3), we can get the following expressions

$$f'(z) = \lambda[C_1(\cos\lambda z - \cosh\lambda z) - C_2(\sin\lambda z + \sinh\lambda z)] \tag{4}$$

$$f''(z) = \lambda^2[-C_1(\sin\lambda z + \sinh\lambda z) - C_2(\cos\lambda z + \cosh\lambda z)] \tag{5}$$

$$f'''(z) = \lambda^3[-C_1(\cos\lambda z + \cosh\lambda z) + C_2(\sin\lambda z - \sinh\lambda z)] \tag{6}$$

Substituting equations (4) to (6) into equations (1) and (2) leads to, respectively,

$$\begin{aligned} &C_1[-EI_Y\lambda^3(\cos\lambda l + \cosh\lambda l) + \omega^2 m_0(\sin\lambda l - \sinh\lambda l) + \omega^2 m_0(l_0 - l)\lambda(\cos\lambda l - \cosh\lambda l)] + \\ &C_2[\omega^2 m_0(\cos\lambda l - \cosh\lambda l) - \omega^2 m_0(l_0 - l)\lambda(\sin\lambda l + \sinh\lambda l) + EI_Y\lambda^3(\sin\lambda l - \sinh\lambda l)] = 0 \end{aligned} \tag{7}$$

$$C_1[EI_Y\lambda^2(\sin\lambda l+\sinh\lambda l)+EI_Y\lambda^3(l_0-l)(\cos\lambda l+\cosh\lambda l)+\omega^2 I_G\lambda(\cos\lambda l-\cosh\lambda l)]+$$
$$C_2[EI_Y\lambda^2(\cos\lambda l+\cosh\lambda l)-EI_Y\lambda^3(l_0-l)(\sin\lambda l-\sinh\lambda l)-\omega^2 I_G\lambda(\sin\lambda l+\sinh\lambda l)]=0 \quad (8)$$

From the Euler-Bernoulli theory of continuous beams, $\omega=\lambda^2\sqrt{\frac{EI_Y}{\rho A}}$, where ρ is the density and A is the cross-sectional area of the beam. Denoting $\beta=\lambda l$ and rewriting equations (7) and (8) yields

$$C_1[-(\frac{\beta}{l})^3(\cos\beta+\cosh\beta)+\frac{m_0}{\rho A}(\frac{\beta}{l})^4(\sin\beta-\sinh\beta)+\frac{m_0(l_0-l)}{\rho A}(\frac{\beta}{l})^5(\cos\beta-\cosh\beta)]+$$
$$C_2[\frac{m_0}{\rho A}(\frac{\beta}{l})^4(\cos\beta-\cosh\beta)-\frac{m_0(l_0-l)}{\rho A}(\frac{\beta}{l})^5(\sin\beta+\sinh\beta)+(\frac{\beta}{l})^3(\sin\beta-\sinh\beta)]=0 \quad (9)$$

$$C_1[(\frac{\beta}{l})^2(\sin\beta+\sinh\beta)+(\frac{\beta}{l})^3(l_0-l)(\cos\beta+\cosh\beta)+\frac{I_G}{\rho A}(\frac{\beta}{l})^5(\cos\beta-\cosh\beta)]+$$
$$C_2[(\frac{\beta}{l})^2(\cos\beta+\cosh\beta)-(l_0-l)(\frac{\beta}{l})^3(\sin\beta-\sinh\beta)-\frac{I_G}{\rho A}(\frac{\beta}{l})^5(\sin\beta+\sinh\beta)]=0 \quad (10)$$

where I_G is the moment of inertia of the end mass about an axis through its centre, parallel to the y-axis, which has this expression

$$I_G=\frac{1}{12}m_0(D^2+W^2) \quad (11)$$

D and *W* are the depth and width of the end mass, respectively.

Then the following system emerges,

$$\begin{cases}a_{11}C_1+a_{12}C_2=0\\ a_{21}C_1+a_{22}C_2=0\end{cases} \quad (12)$$

where β is unknown.

To have a unique solution of C_1 and C_2, the determinant of this system should equal to zero. That is,

$$a_{11}a_{22}-a_{12}a_{21}=0 \quad (13)$$

Solving equation (13) gives several numerical values of β, which correspond to the eigenvalues λ_i. From λ_i, the corresponding natural frequencies, ω_i, can be found. Equation (13) can also be used to find the ratio of C_2 to C_1. The ratio combined with the normalization equation can lead to the expressions of the mode shapes of the first and second bending modes. The mode shape coefficients can then be obtained on the basis of the mode shape expressions.

A.1.3 An Example

An example is taken to explain the above procedure. The feature of the system is listed in table A.1-1.

- β values

Equation (13) is used to get solutions of β. Setting different ranges for β in equation (13) yields different values. The first two are kept, corresponding to the first and second bending mode that we are interested in, marked as β_1 and β_2. The numerical results are shown in Fig A.1-1 and Fig A.1-2 when the β value range is made as [0, 1.5] and [1.5, 4.0].

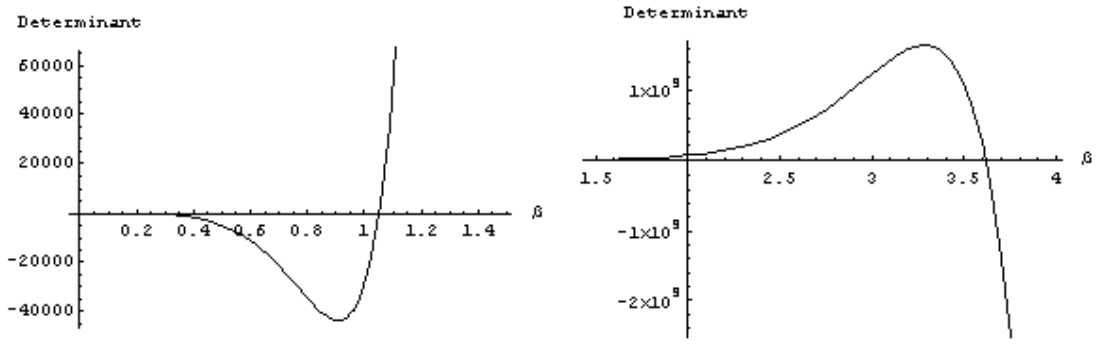

Fig A.1.1, Fig A.1.2 β values against the determinant in the [0, 1.5] and [1.5, 4.0] range.

$$\beta_1 = 1.05178 \quad \beta_2 = 3.61829 \tag{14}$$

- Ratio of C_2 to C_1.

Let us assume $C^* = -\frac{C_2}{C_1} = \frac{a_{11}}{a_{12}} = \frac{a_{21}}{a_{22}}$. Upon using equation (13) again and with the above β values in (14) gives

$$C_1^* = 1.06699 \qquad C_2^* = 0.98702 \tag{15}$$

C_1^* and C_2^* are the ratios of minus C_2 to C_1 corresponding to β_1 and β_2 respectively.

- C_1

Substituting $\beta = \lambda l$ and $C^* = -\frac{C_2}{C_1}$ gives

$$f_i(z) = C_1[(\sin\frac{\beta_i}{l}z - \sinh\frac{\beta_i}{l}z) - C^*(\cos\frac{\beta_i}{l}z - \cosh\frac{\beta_i}{l}z)] \qquad i = 1,2 \tag{16}$$

Reference (Forehand and Cartmell 2001) gives a detailed explanation that the mode shapes for bending modes can be normalized so that,

$$\int_0^l m(f_i(z))^2 dz + m_0(f_i(l) + (l_0 - l)f_i'(l))^2 + I_G(f_i'(l))^2 = m_0 \qquad i = 1,2 \tag{17}$$

The expression of $f_i(z)$ in (16) and its first order derivative $f_i'(z)$ with respect to z and with equation (17) leads to

$$C_{11} = 1.0083 \qquad C_{12} = 1.06236 \tag{18}$$

C_{11} and C_{12} are the values of C_1 corresponding to β_1 and β_2, C_1^* and C_2^* respectively.

- Mode shapes

Substituting β_i, C_i^*, C_{1i} and l into equation (16) and plotting the mode shape as a function of z gives Fig A.1.3 and Fig A.1.4.

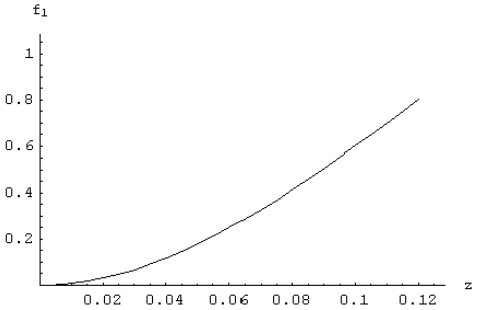

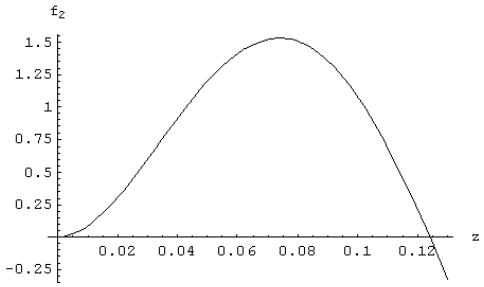

Fig A.1.3, Fig A.1.4 Modes for the first and second bending

	Name	Symbol	Value
Beam	length one (from the top of the base-clamp to the below end point of the beam)	l	$0.12\,m$
	length two(from the centre of the mass to the below end point of the beam)	l_0	$0.1275\,m$
	density	ρ	$7800\,kg/m^3$
	Thickness	t_b	$0.00072\,m$
	Width	W_b	$0.025\,m$
	section-cross area of the beam	A	$0.025*0.00072\,m^2$
	mass/meter	$m=\rho A$	$0.1404\,kg$
	Young's modulus	E	$201\,GPa$
	shear modulus	G	$79.3\ GPa$
End mass	mass of the end mass	m_0	$0.031\,kg$
	moment of inertia	I_G	$1.243*10^{-6}\ kg\cdot m^2$
	width of the end mass	W	$0.016\,m$
	depth of the end mass	D	$0.015\,m$

Table A.1.1 Features of a beam system

- Bending mode shape coefficients

Hence, the coefficients are calculated as the follows

$$X=\int_0^l (f_1')^2 dz = 6.4643 \quad N=\int_0^l (f_1'')^2 dz = 1119.63 \qquad Z=\int_0^l (f_2')^2 dz = 86.9849$$

$$P=\int_0^l (f_2'')^2 dz = 131036 \quad Y=\int_0^l (f_1' f_2') dz = -5.5520 \quad S=\int_0^l (f_1'' f_2'') dz = -5.0763*10^{-6}$$

$$Q=\int_0^l (g_1')^2 dz = 8.3333$$

- Natural frequencies of the bending modes

Manipulations on $\lambda^4=\omega^2 m/EI_Y$ leads to $\omega_i=(\beta_i/l)^2*\sqrt{(EI_Y/\rho A)}$. Here EI_Y is the flexural rigidity about the y-axis.

$$EI_Y=\frac{w_b {t_b}^3}{12} \tag{19}$$

$$\omega_1 = 81.06\ s^{-1} = 12.90 Hz \quad \omega_2 = 959.26\ s^{-1} = 152.67 Hz$$

- Mode Shape of the torsion mode

The general mode shape for a linear fundamental torsion mode is usually of the form: $g_1(z) = E_1 \sin pz + E_2 \cos pz$, where E_1 and E_2 are constants, $p = \omega\sqrt{\rho / Gg}$, ρ being the material density, G shear modulus of the material, ω natual frequency of the linear torsion mode.

The natural frequency expression for this system is,

$$\omega = \sqrt{\frac{GI_0}{lI_m}} \tag{20}$$

Where l is the beam length; I_0 is the polar moment of inertia of the beam; I_m is the mass moment of inertia of the lumped mass. They are calculated by using the following equations (21) and (22).

$$I_0 = I_x + I_y = \frac{1}{12} t_b w_b^3 + \frac{1}{12} w_b t_b^3 \tag{21}$$

$$I_m = \frac{1}{12} m_0 (D^2 + W^2) \tag{22}$$

Substitution of appropriate numerical quantities in Table A.1.1 into equations (21), (22) and (20) leads to $\omega = 22.34 \times 10^3\ 1/rad$, $p = 2.24 \times 10^{-3}$, $pl = 2.69 \times 10^{-4}$.

Substitution of the boundary condition $g_1(0) = 0$ leads to $E_2 = 0$. Using the normalisation $g_1(l) = 1$ gives $E_1 = \frac{1}{\sin pl} \approx \frac{1}{pl}$. Now the expression for the normalised, linear, torsional mode function is

$$g_1(z) = \frac{1}{pl} \times \sin pz \approx \frac{1}{pl} \times pz = \frac{z}{l} \tag{23}$$

So $$B_1 = \int_0^l (l - z) g_1 f_1'' dz = 0.2036 \qquad B_2 = \int_0^l (l - z) g_1 f_2'' dz = -1.5889$$

Appendix 2

Ordering Scheme for Cross-Coupling Terms

A.2.1 Abstract

This appendix presents a summary of a proposal for perturbation ordering a linear coupling term. The linear cross-coupling term appears in the zeroth order perturbation equations when the normal procedure of using the perturbation method of multiple scales is followed. On the grounds of appropriate numerical calculations it can be shown that this coupling term may be weaker than the other linear terms in the zeroth order equations. Therefore, this term can then be placed a higher order, and the zeroth order equations turn out to be solvable. The aim of this appendix discusses this matter.

A.2.2 Introduction

The normal procedure of applying the perturbation method of multiple scales in the stability and dynamical systems is as follows (Cartmell *et al* 2003): "*The linear terms are initially considered as strong terms compared to the forms of nonlinearity, or nonlinearities, and considered as the lowest order. The lowest order perturbation equations are normally expressed as* $D_0^2 u_0 + \omega^2 u_0 = 0$ *.The subscripts can be different dependent on the structure of the power series. The solution is expressed in complex form* $u_0 = Ae^{i\omega T_0} + \overline{A}e^{-i\omega T_0}$ *, noting that* ω *is an appropriate natural frequency of undamped vibration and that the overbar represents complex conjugacy. The amplitude A is determined by the process in which the secular terms are removed and then equated to zero. Once this stage has been reached, solutions can be obtained to higher orders of perturbation for each different resonance conditions. Finally, the perturbation solutions for the resonance condition of interest are recombined to give an approximate, but frequently very accurate, solution to the dependent variable(s) in the time domain"*. For the case of Su and Cartmell (2008), when the above procedure is followed the lowest order perturbation equations, in this case the zeroth order perturbation equations, are as given below

$$D_0^2 \overline{U}_{10} + \omega_1^2 \overline{U}_{10} + p^2 \overline{U}_{20} = 0$$

$$D_0^2\overline{U}_{20} + \omega_2^2\overline{U}_{20} + p^2\overline{U}_{10} = 0 \qquad (1)$$

These are not in the expected form,

$$D_0^2\overline{U}_{10} + \omega_1^2\overline{U}_{10} = 0$$

$$D_0^2\overline{U}_{20} + \omega_2^2\overline{U}_{20} = 0 \qquad (2)$$

where ω_1 and ω_2 are the natural frequencies of the first and second bending modes. $\overline{U}_1$ and $\overline{U}_2$ are the corresponding modal co-ordinates. p^2 is the cross coupling term extracted from the potential energy expressions after mode orthogonality has been implemented. Therefore, as required, the proposal for assigning the cross coupling term to higher perturbation order, and therefore changing the zeroth order perturbation equations into their usual format is discussed next.

A.2.3 Numerical Calculations on ω_1^2, ω_2^2 and p^2

The expressions for ω_1^2, ω_2^2 and p^2 are as follows:

$$\omega_1^2 = RN - gX \qquad \omega_2^2 = RP - gZ \qquad p^2 = RS - gY \qquad (3)$$

where

$$R = \frac{EI_Y}{m_0} \qquad S = \int_0^l (f_1'' f_2'')dz \qquad Y = \int_0^l (f_1' f_2')dz$$

$$N = \int_0^l (f_1'')^2 dz \qquad X = \int_0^l (f_1')^2 dz \qquad Z = \int_0^l (f_2')^2 dz \qquad P = \int_0^l (f_2'')^2 dz$$

As seen from Equation (3), ω_1^2, ω_2^2 and p^2 are constants if the geometry, density and Young's modulus of the beam and the end mass are given. Comparisons between p^2 and ω_1^2, and between p^2 and ω_2^2 are feasible. If p^2 is much smaller than ω_1^2 and ω_2^2, it may be considered to be indicative of a weaker term than ω_1^2 or ω_2^2 and therefore regarded to be at higher perturbation order. A few examples are taken to show that under certain circumstances, $p^2 << \omega_1^2$ and $p^2 << \omega_2^2$ can be satisfied in practise. The examples are based on

two types of beams and an end mass made of aluminium. Their geometries and properties are listed in Table A.2.1:

	steel beam	glass epoxy beam	end mass
Width (mm)	25	13	15
Thickness (mm)	0.7	2.2	15
Density (kg/m^3)	7800	1865	2700
Young's Modulus (GPa)	201	25	

Table A.2.1 Geometry and property of the two beams

Results of numerical calculations for $\omega_1^2, \omega_2^2, p^2$ as well as p^2/ω_1^2 and p^2/ω_2^2, are presented in Table A.2.2-5. p^2/ω_1^2 and p^2/ω_2^2 against certain factors are presented in Fig A.2.1-6. The influence of these factors on the results are: the material of the beam, the length of the beam l, the mass of the end mass m_0 and the moment of inertia of the end mass I_G. To study the influence of the moment inertia I_G, the width and thickness of the end mass are kept constant and equal as 15 mm. By increasing the length of the end mass, denoted by L_m, the mass is increased and so is the moment of inertia I_G.

l (mm)	p^2	ω_1^2	ω_2^2	p^2/ω_1^2	p^2/ω_2^2
100	71.45	35911.3	7.24*10^6	0.199%	0.000987%
150	71.06	11066.6	1.96*10^6	0.64%	0.00362%
200	57.77	4677.15	7.03*10^5	1.24%	0.00822%
250	46.64	2362.51	3.08*10^5	1.97%	0.0151%
300	38.36	1338.16	1.55*10^5	2.87%	0.0247%

Table A.2.2 Values of $\omega_1^2, \omega_2^2, p^2$, p^2/ω_1^2 and p^2/ω_2^2 against the steel beam length

($m_0 = 18.2g, I_G = 6.834\times10^{-7} kg.m^2$)

l (mm)	p^2	ω_1^2	ω_2^2	p^2/ω_1^2	p^2/ω_2^2
100	66.08	17911.9	1.88*10^6	0.369%	0.00351%
150	55.53	5267.55	4.63*10^5	1.054%	0.0120%
200	43.3	2130.63	1.63*10^5	2.032%	0.0266%
250	34.34	1032.59	7.14*10^4	3.326%	0.0481%
300	27.9	562.32	3.62*10^4	4.962%	0.0771%

Table A.2.3 Values of $\omega_1^2, \omega_2^2, p^2, p^2/\omega_1^2$ and p^2/ω_2^2 against the g-e beam length

($m_0 = 18.2g, I_G = 6.834\times10^{-7} kg.m^2$)

l (mm)	L_m (mm)	m_0 (g)	I_G (g.mm^4)	p^2/ω_1^2	p^2/ω_2^2
100	30	18.2	683.44	0.369%	0.00351%
	35	21.3	797.34	0.43%	0.00368%
	40	24.3	911.25	0.493%	0.00384%
150	30	18.2	683.44	1.054%	0.0120%
	35	21.3	797.34	1.25%	0.0127%
	40	24.3	911.25	1.440%	0.0134%
200	30	18.2	683.44	2.032%	0.0266%
	35	21.3	797.34	2.40%	0.0284%
	40	24.3	911.25	2.780%	0.0301%
250	30	18.2	683.44	3.326%	0.0481%
	35	21.3	797.34	3.92%	0.0517%
	40	24.3	911.25	4.536%	0.0549%
300	30	18.2	683.44	4.962%	0.0771%
	35	21.3	797.34	5.84%	0.0833%
	40	24.3	911.25	6.760%	0.0888%

Table A.2.4 Values of p^2/ω_1^2 and p^2/ω_2^2 against the end mass length L_m (steel beams)

l(mm)	L_m (mm)	m_0 (g)	I_G (g.mm^4)	p^2/ω_1^2	p^2/ω_2^2
100	25	15.2	569.53	0.166%	0.000929%
	30	18.2	683.44	0.199%	0.000987%
	35	21.3	797.34	0.231%	0.00104%
150	25	15.2	569.53	0.53%	0.00329%
	30	18.2	683.44	0.64%	0.00362%
	35	21.3	797.34	0.771%	0.00386%
200	25	15.2	569.53	0.99%	0.00761%
	30	18.2	683.44	1.24%	0.00822%
	35	21.3	797.34	1.49%	0.00878%
250	25	15.2	569.53	1.59%	0.0140%
	30	18.2	683.44	1.97%	0.0151%
	35	21.3	797.34	2.38%	0.0162%
300	25	15.2	569.53	2.31%	0.0228%
	30	18.2	683.44	2.87%	0.0247%
	35	21.3	797.34	3.46%	0.0264%

Table A.2.5 Values of p^2/ω_1^2 and p^2/ω_2^2 against the length of the end mass (g-e beams)

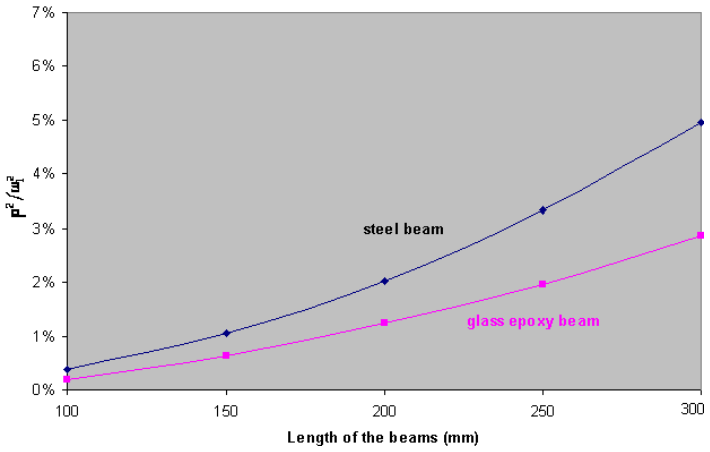

Fig A.2.1 Influence of the beam length on p^2/ω_1^2

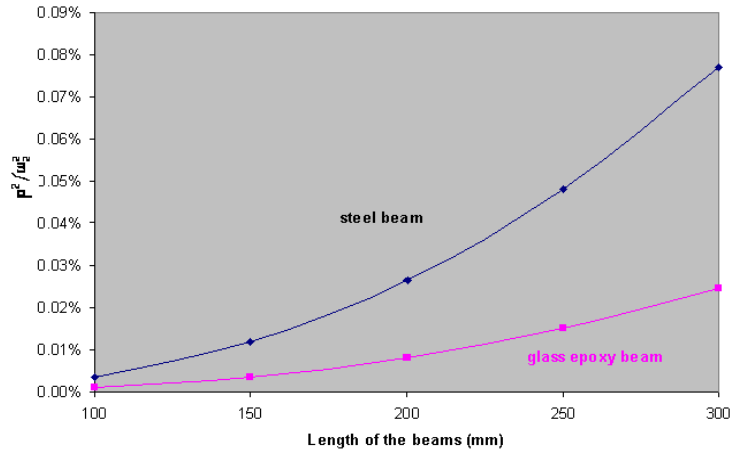

Fig A.2.2 Influence of the beam length on p^2 / ω_2^2

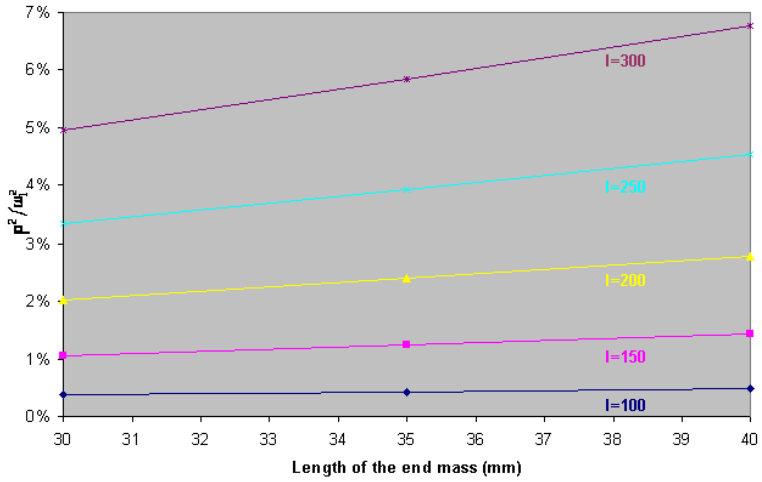

Fig A.2.3 Influence of the moment of inertia I_G on p^2 / ω_1^2 (steel beams)

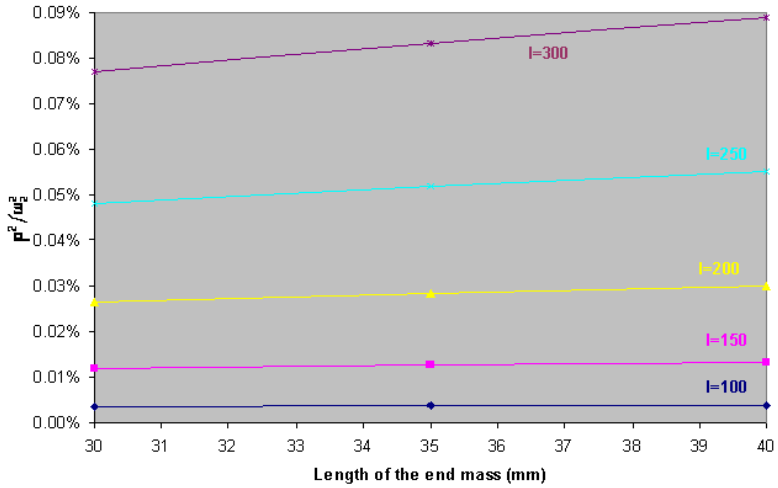

Fig A.2.4 Influence of the moment of inertia I_G on p^2 / ω_2^2 (steel beams)

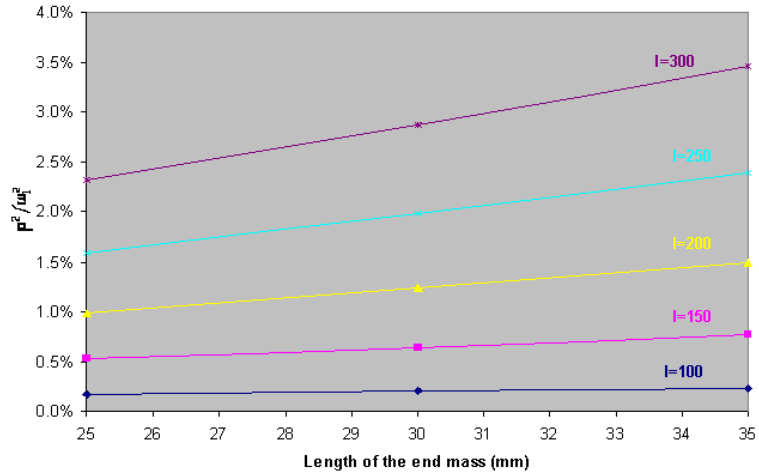

Fig A.2.5 Influence of the moment of inertia I_G on p^2/ω_1^2 (g-e beams)

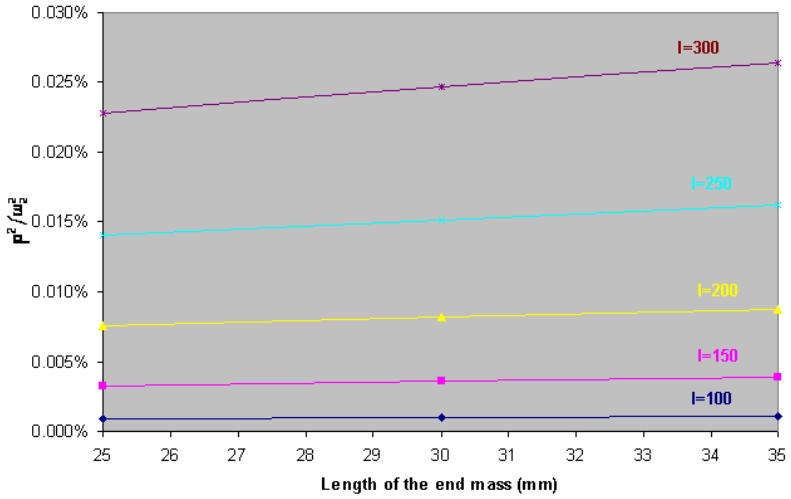

Fig A.2.6 Influence of the moment of inertia I_G on p^2/ω_2^2 (g-e beams)

A.2.4 Discussions

(1) In the above study, for both the steel and glass epoxy beams, the length range is from 100 mm to 300 mm. The end mass is made of aluminium with the same width and thickness at 15 mm. The range of the length of the end mass is from 25 mm to 45 mm. As seen from Tables 2-5, the maximum value of p^2 is only 6.74% of ω_1^2, and only 0.0888% of ω_2^2, numerically much less than ω_1^2 and ω_2^2.

(2) As can be seen from Fig A.2.1-2, the ratios, p^2/ω_1^2 and p^2/ω_2^2 increase as the length of both beams increases.

(3) As can be seen from Fig A.2.3-6, the ratios, p^2/ω_1^2 and p^2/ω_2^2 increase as the length of the end mass increases. Therefore the ratios increase as the mass of the end mass increases, and in the same manner for the moment of inertia I_G.

A.2.5 Conclusions

(1) For the above two beams shown in Table 1, under certain conditions, the ratios, p^2/ω_1^2 and p^2/ω_2^2 are numerically small, so the cross coupling term p^2 can possibly be considered to be at higher perturbation order.

(2) Such factors as the length of the beams, the mass of the end mass, and the moment of inertia of the end mass, all have an effect on the ratios, p^2/ω_1^2 and p^2/ω_2^2.

(3) Such a comparison is hard to generalise definitively, and so if it does turn out to be physically unacceptable, then this convenient ordering scheme cannot be used.

Appendix 3

Mathematica™ Programme for Solving $\overline{u}_{11}$ and $\overline{u}_{21}$ in the Non-resonant Case

In the non-resonant case, the solution to $\overline{U_{11}}$ in the first order equations, after the secular terms are removed, is obtained in this program. The same approach is applied to obtain the solution to $\overline{U_{21}}$.

The right hand side of $\overline{U_{11}}$ in the first order equations, denoted as RHS1_non-resonant, as shown in equation (28) in Chapter 3, is re-written as below

In[1]:=
$$RHS1\_non-resonant = e^{i\times T_0\times\omega_1}\left(-\frac{1}{2}e^{-i\Omega T_0}X\Omega^2\hat{A}_B A_1[T_1,T_2]-\frac{1}{2}e^{i\Omega T_0}X\Omega^2\hat{A}_B A_1[T_1,T_2]-e^{-iT_0\omega_1+iT_0\omega_2}\overline{p}^2 A_2[T_1,T_2]-\frac{1}{2}e^{-i\Omega T_0-iT_0\omega_1+iT_0\omega_2}Y\Omega^2\hat{A}_B A_2[T_1,T_2]-\frac{1}{2}e^{i\Omega T_0-iT_0\omega_1+iT_0\omega_2}Y\Omega^2\hat{A}_B A_2[T_1,T_2]-\frac{1}{2}e^{-i\Omega T_0-2iT_0\omega_1}X\Omega^2\hat{A}_B\overline{A}_1[T_1,T_2]-\frac{1}{2}e^{i\Omega T_0-2iT_0\omega_1}X\Omega^2\hat{A}_B\overline{A}_1[T_1,T_2]-e^{-iT_0\omega_1-iT_0\omega_2}\overline{p}^2\overline{A}_2[T_1,T_2]-\frac{1}{2}e^{-i\Omega T_0-iT_0\omega_1-iT_0\omega_2}Y\Omega^2\hat{A}_B\overline{A}_2[T_1,T_2]-\frac{1}{2}e^{i\Omega T_0-iT_0\omega_1-iT_0\omega_2}Y\Omega^2\hat{A}_B\overline{A}_2[T_1,T_2]\right);$$

Multiplying out the term $e^{iT_0\omega_1}$ in In[1], RHS1_non – resonant then becomes

In[2]:=
$$RHS1\_non-resonant = -\frac{1}{2}e^{iT_0(\omega_1-\Omega)}X\Omega^2\hat{A}_B A_1[T_1,T_2]-\frac{1}{2}e^{iT_0(\omega_1+\Omega)}X\Omega^2\hat{A}_B A_1[T_1,T_2]-e^{iT_0\omega_2}\overline{p}^2 A_2[T_1,T_2]-\frac{1}{2}e^{iT_0(\omega_2-\Omega)}Y\Omega^2\hat{A}_B A_2[T_1,T_2]-\frac{1}{2}e^{iT_0(\omega_2+\Omega)}Y\Omega^2\hat{A}_B A_2[T_1,T_2]-\frac{1}{2}e^{-iT_0(\omega_1+\Omega)}X\Omega^2\hat{A}_B\overline{A}_1[T_1,T_2]-\frac{1}{2}e^{-iT_0(\omega_1-\Omega)}X\Omega^2\hat{A}_B\overline{A}_1[T_1,T_2]-e^{-iT_0\omega_2}\overline{p}^2\overline{A}_2[T_1,T_2]-\frac{1}{2}e^{-iT_0(\omega_2+\Omega)}Y\Omega^2\hat{A}_B\overline{A}_2[T_1,T_2]-\frac{1}{2}e^{-iT_0(\omega_2-\Omega)}Y\Omega^2\hat{A}_B\overline{A}_2[T_1,T_2];$$

Assuming a trial solution for $\overline{U}_{11}$:

In[3]:=
$$\overline{U}_{11} = B e^{iT_0(\omega_1-\Omega)}+C e^{iT_0(\omega_1+\Omega)}+D e^{iT_0\omega_2}+F e^{iT_0(\omega_2-\Omega)}+G e^{iT_0(\omega_2+\Omega)}+H e^{-iT_0(\omega_1+\Omega)}+J e^{-iT_0\omega_2}+K e^{-iT_0(\omega_2+\Omega)}+L e^{-iT_0(\omega_2-\Omega)}+M e^{-iT_0(-\Omega+\omega_1)};$$

Differentiating In[3] twice with respect to T_0

In[4]:=
$$D[\overline{U}_{11},\{T_0,2\}]$$

Out[4]=
$$-B e^{iT_0(-\Omega+\omega_1)}(-\Omega+\omega_1)^2-e^{-iT_0(-\Omega+\omega_1)}M(-\Omega+\omega_1)^2-C e^{iT_0(\Omega+\omega_1)}(\Omega+\omega_1)^2-e^{-iT_0(\Omega+\omega_1)}H(\Omega+\omega_1)^2-D e^{iT_0\omega_2}\omega_2^2-e^{-iT_0\omega_2}J\omega_2^2-e^{iT_0(-\Omega+\omega_2)}F(-\Omega+\omega_2)^2-e^{-iT_0(-\Omega+\omega_2)}L(-\Omega+\omega_2)^2-e^{iT_0(\Omega+\omega_2)}G(\Omega+\omega_2)^2-e^{-iT_0(\Omega+\omega_2)}K(\Omega+\omega_2)^2$$

The left hand side of $\overline{U_{11}}$ in the first order equations, as shown in equations (28) in Chapter 3, is the following

In[5]:=
```
D[U11, {T0, 2}] + ω1^2 U11;
Simplify[Collect[ExpandAll[(D[U11, {T0, 2}] + ω1^2 U11)], {B, C, D, F, G, H, J, K, L, M}]]
```

Out[6]=

$$e^{-i T_0 (\Omega+\omega_1+\omega_2)} \left(-\left(B\, e^{i T_0 (2\omega_1+\omega_2)} + C\, e^{i T_0 (2\Omega+2\omega_1+\omega_2)} + e^{i T_0 (\omega_1+2\omega_2)} F + e^{i T_0 (\omega_1+2(\Omega+\omega_2))} G + e^{i T_0 \omega_2} H + e^{i T_0 \omega_1} K + e^{i T_0 (2\Omega+\omega_1)} L + e^{i T_0 (2\Omega+\omega_2)} M\right)\Omega^2 + 2\, e^{i T_0 \omega_2}\left(B\, e^{2 i T_0 \omega_1} - C\, e^{2 i T_0 (\Omega+\omega_1)} - H + e^{2 i \Omega T_0} M\right)\Omega\,\omega_1 + e^{i T_0 \omega_1}\left(D\, e^{i T_0 (\Omega+2\omega_2)} + e^{2 i T_0 \omega_2} F + e^{2 i T_0 (\Omega+\omega_2)} G + e^{i \Omega T_0} J + K + e^{2 i \Omega T_0} L\right)\omega_1^2 + 2\, e^{i T_0 \omega_1}\left(e^{2 i T_0 \omega_2} F - e^{2 i T_0 (\Omega+\omega_2)} G - K + e^{2 i \Omega T_0} L\right)\Omega\,\omega_2 - e^{i T_0 \omega_1}\left(D\, e^{i T_0 (\Omega+2\omega_2)} + e^{2 i T_0 \omega_2} F + e^{2 i T_0 (\Omega+\omega_2)} G + e^{i \Omega T_0} J + K + e^{2 i \Omega T_0} L\right)\omega_2^2\right)$$

Referring to In[2], the solutions to $\overline{U}_{11}$ can be derived as

$$B == \frac{-X\,\Omega^2\,\hat{A}_B\,A_1[T_1, T_2]}{2\,(-\Omega^2 + 2\,\Omega\,\omega_1)};$$

$$C == \frac{-X\,\Omega^2\,\hat{A}_B\,A_1[T_1, T_2]}{2\,(-\Omega^2 - 2\,\Omega\,\omega_1)};$$

$$D == \frac{-\overline{p}^2\,A_2[T_1, T_2]}{(\omega_1^2 - \omega_2^2)};$$

$$F == \frac{-Y\,\Omega^2\,\hat{A}_B\,A_2[T_1, T_2]}{2\,(-\Omega^2 + \omega_1^2 + 2\,\Omega\,\omega_2 - \omega_2^2)};$$

$$G == \frac{-Y\,\Omega^2\,\hat{A}_B\,A_2[T_1, T_2]}{2\,(-\Omega^2 + \omega_1^2 - 2\,\Omega\,\omega_2 - \omega_2^2)};$$

$$H == \frac{-X\,\Omega^2\,\hat{A}_B\,\overline{A}_1[T_1, T_2]}{2\,(-\Omega^2 - 2\,\Omega\,\omega_1)};$$

$$J == \frac{-\overline{p}^2\,\overline{A}_2[T_1, T_2]}{(\omega_1^2 - \omega_2^2)};$$

$$K == \frac{-Y\,\Omega^2\,\hat{A}_B\,A_2[T_1, T_2]}{2\,(-\Omega^2 + \omega_1^2 - 2\,\Omega\,\omega_2 - \omega_2^2)};$$

$$L == \frac{-Y\,\Omega^2\,\hat{A}_B\,\overline{A}_2[T_1, T_2]}{2\,(-\Omega^2 + \omega_1^2 + 2\,\Omega\,\omega_2 - \omega_2^2)};$$

$$M == \frac{-X\,\Omega^2\,\hat{A}_B\,\overline{A}_2[T_1, T_2]}{2\,(-\Omega^2 + 2\,\Omega\,\omega_1)};$$

The above expressions for B, C, D, F, G, H, J, K, L, and M are substituted into In[3]. The solution to $\overline{U_{11}}$ is therefore derived as

In[7]:=
$$\overline{U}_{11} = e^{i T_0 (\omega_1-\Omega)}\left(\frac{-X\,\Omega^2\,\hat{A}_B\,A_1[T_1,T_2]}{2(-\Omega^2+2\,\Omega\,\omega_1)}\right)+e^{i T_0 (\omega_1+\Omega)}\left(\frac{X\,\Omega^2\,\hat{A}_B\,A_1[T_1,T_2]}{2(\Omega^2+2\,\Omega\,\omega_1)}\right)+e^{i T_0\,\omega_2}\left(\frac{-\overline{p}^2\,A_2[T_1,T_2]}{(\omega_1^2-\omega_2^2)}\right)+$$
$$e^{i T_0 (\omega_2-\Omega)}\left(\frac{-Y\,\Omega^2\,\hat{A}_B\,A_2[T_1,T_2]}{2(-\Omega^2+\omega_1^2+2\,\Omega\,\omega_2-\omega_2^2)}\right)+e^{i T_0 (\omega_2+\Omega)}\left(\frac{-Y\,\Omega^2\,\hat{A}_B\,A_2[T_1,T_2]}{2(-\Omega^2+\omega_1^2-2\,\Omega\,\omega_2-\omega_2^2)}\right)+$$
$$e^{-i T_0 (\omega_1+\Omega)}\left(\frac{X\,\Omega^2\,\hat{A}_B\,\overline{A}_1[T_1,T_2]}{2(\Omega^2+2\,\Omega\,\omega_1)}\right)+e^{-i T_0\,\omega_2}\left(\frac{-\overline{p}^2\,\overline{A}_2[T_1,T_2]}{(\omega_1^2-\omega_2^2)}\right)+$$
$$e^{-i T_0 (\omega_2+\Omega)}\left(\frac{-Y\,\Omega^2\,\hat{A}_B\,\overline{A}_2[T_1,T_2]}{2(-\Omega^2+\omega_1^2-2\,\Omega\,\omega_2-\omega_2^2)}\right)+e^{-i T_0 (\omega_2-\Omega)}\left(\frac{-Y\,\Omega^2\,\hat{A}_B\,\overline{A}_2[T_1,T_2]}{2(-\Omega^2+\omega_1^2+2\,\Omega\,\omega_2-\omega_2^2)}\right)+$$
$$e^{-i T_0 (-\Omega+\omega_1)}\left(\frac{-X\,\Omega^2\,\hat{A}_B\,\overline{A}_1[T_1,T_2]}{2(-\Omega^2+2\,\Omega\,\omega_1)}\right);$$

Counter-- Checking the Solution to $\overline{U}_{11}$

In[8]:=
```
D[D[U11bar, T0], T0];
D[U11bar, {T0, 2}] + ω1^2 U11bar;
FullSimplify[
  % / (-1/2 e^(i T0 (-Ω+ω1)) X Ω^2 Âb A1[T1, T2] - 1/2 e^(i T0 (Ω+ω1)) X Ω^2 Âb A1[T1, T2] - e^(i T0 ω2) p̄^2 A2[T1, T2] -
    1/2 e^(i T0 (-Ω+ω2)) Y Ω^2 Âb A2[T1, T2] - 1/2 e^(i T0 (Ω+ω2)) Y Ω^2 Âb A2[T1, T2] -
    1/2 e^(-i T0 (-Ω+ω1)) X Ω^2 Âb Ā1[T1, T2] - 1/2 e^(-i T0 (Ω+ω1)) X Ω^2 Âb Ā1[T1, T2] -
    e^(-i T0 ω2) p̄^2 Ā2[T1, T2] - 1/2 e^(-i T0 (-Ω+ω2)) Y Ω^2 Âb Ā2[T1, T2] - 1/2 e^(-i T0 (Ω+ω2)) Y Ω^2 Âb Ā2[T1, T2])]
```

Out[10]= 1

Appendix 4

Resonance Derived from the Second-order Perturbation Equations

The resonances derived from equations (22) to (24) in Chapter 3 are listed in Table A.4.1.

Equation (22)		**Equation(23)**		**Equation(24)**	
External Forced Resonance	Internal Resonance	External Forced Resonance	Internal Resonance	External Forced Resonance	Internal Resonance
$\Omega = 2\omega_1$ $\Omega = \omega_1$ $\Omega = \omega_2 - \omega_1$ $\Omega = \omega_2 + \omega_1$ $\Omega = \frac{1}{2}(\omega_2 - \omega_1)$ $\Omega = \frac{1}{2}(\omega_2 + \omega_1)$	$\omega_1 = \frac{1}{3}\omega_2$ $\omega_1 = \frac{1}{2}\omega_2$ $\omega_1 = \frac{2}{3}\omega_2$ $\omega_1 = \frac{2}{3}\omega_t$ $\omega_1 = \frac{1}{4}\omega_2$ $\omega_1 = \omega_2 - 2\omega_t$ $\omega_1 = 2\omega_t - \omega_2$ $\omega_1 = 3\omega_t - \omega_2$ $\omega_1 = 2\omega_t - 2\omega_2$ $\omega_1 = 2\omega_2 - 2\omega_t$ $\omega_1 = \frac{1}{2}\omega_t$ $\omega_1 = \omega_2 - \omega_t$ $\omega_1 = \omega_t - \omega_2$ $\omega_1 = 2\omega_2 - 2\omega_t$ $\omega_1 = 2\omega_t - 2\omega_2$	$\Omega = 2\omega_2$ $\Omega = \omega_2$ $\Omega = \omega_2 - \omega_1$ $\Omega = \omega_2 + \omega_1$ $\Omega = \frac{1}{2}(\omega_2 - \omega_1)$ $\Omega = \frac{1}{2}(\omega_2 + \omega_1)$	$\omega_2 = 2\omega_t$ $\omega_2 = 2\omega_t - 2\omega_1$ $\omega_2 = 2\omega_1 - 2\omega_t$ $\omega_2 = \omega_t$ $\omega_2 = \frac{3}{2}\omega_t$ $\omega_2 = \frac{2}{3}\omega_t$ $\omega_2 = 2\omega_t$ $\omega_2 = 3\omega_1$ $\omega_2 = 4\omega_1$ $\omega_2 = 2\omega_t + \omega_1$ $\omega_2 = 3\omega_t + \omega_1$ $\omega_2 = 2\omega_t - \omega_1$ $\omega_2 = 3\omega_t - \omega_1$ $\omega_2 = 2\omega_1$ $\omega_2 = \frac{3}{2}\omega_1$ $\omega_2 = \omega_t + \omega_1$ $\omega_2 = \omega_t - \omega_1$ $\omega_2 = \frac{1}{2}\omega_t$ $\omega_2 = 2\omega_t - \omega_1$ $\omega_2 = 2\omega_1 + 2\omega_t$		$\omega_t = \omega_1$ $\omega_t = \frac{1}{2}(\omega_2 - \omega_1)$ $\omega_t = \omega_1 + \omega_2$ $\omega_t = \frac{1}{2}\omega_1$ $\omega_t = \omega_2 - \omega_1$ $\omega_t = \frac{1}{3}(\omega_1 + \omega_2)$ $\omega_2 = 2\omega_1$ $\omega_t = \frac{1}{3}(\omega_2 - \omega_1)$ $\omega_t = \omega_2$ $\omega_t = \omega_1 - \frac{1}{2}\omega_2$ $\omega_t = \frac{1}{2}(\omega_2 + \omega_1)$ $\omega_t = \omega_2 - \frac{1}{2}\omega_1$ $\omega_t = \frac{2}{3}\omega_1$ $\omega_t = \frac{1}{2}\omega_2$ $\omega_t = \frac{2}{3}\omega_2$ $\omega_t = 2\omega_2$ $\omega_t = \frac{1}{2}\omega_1 + \omega_2$ $\omega_t = 2\omega_1$ $\omega_t = \frac{1}{2}\omega_2 - \omega_1$ $\omega_t = \frac{1}{2}\omega_1$ $\omega_t = \frac{3}{2}\omega_2$ $\omega_t = \omega_1 + \frac{1}{2}\omega_2$

Table A.4.1 List of resonances derived from the second-order perturbation equations

Appendix 5

Mathematica™ Programme for Natural Frequencies and Mode Shape Coefficients in Chapter 5 and 6

f [z]: mode shape functions of bending modes
f [l]: mode shape functions at z=l
Fa: The recovery force
LHS1: Left hand side of Eq. (29) in Chapter 5
LHS2: Left hand side of Eq. (30) in Chapter 5
a11, a21: Coefficient of C_1 in LHS1, LHS2 respectively
a12, a22: Coefficient of C_2 in LHS1, LHS2 respectively

```
f[z] = C1 (Cosh[λ1 z] - Cos[λ2 z]) + C2 (Sinh[λ1 z] - (λ1/λ2) Sin[λ2 z]);

f[l] = C1 (Cosh[λ1 l] - Cos[λ2 l]) + C2 (Sinh[λ1 l] - (λ1/λ2) Sin[λ2 l]);

LHS1 = EIy * D[D[D[f[l], l], l], l] + 2 Fa * D[f[l], l] +
    ω^2 m0 (f[l] + (l0 - l) * D[f[l], l]);

LHS2 = -ω^2 IG * D[f[l], l] +
    EIy * (D[D[f[l], l], l] + (l0 - l) * D[D[D[f[l], l], l], l]);
```

To obtain the coefficient of C_1 and C_2 in LHS1, LHS2 respectively

```
Collect[Collect[Expand[LHS1], C1], C2];

Collect[Collect[Expand[LHS2], C1], C2];
```

```
GetFreq[Fa_] := Module[{ω1, ω2},
  l = 0.3; E_s1 = E_s2 = 26.3 * 10^9; m_0 = 2700 * 0.015 * 0.015 * 0.045;
  I_G = 1/12 * m_0 * (0.015^2 + 0.015^2); w_b = 0.013; w_s1 = w_s2; t_s1 = t_s2 = 0.0005;
  ρ_s1 = ρ_s2 = 6448.1; ρ = 1865; t_b = 0.0022; E_b = 25 * 10^9; m_s = ρ_s1 * (v_s1 + v_s2);
  m_b = ρ * v; v_s1 = w_s1 * t_s1 * l; v_s2 = w_s2 * t_s2 * l; v = w_b * t_b * l;
  A = w_b * t_b + w_s1 * t_s1 + w_s2 * t_s2;
  I_y1 = 1/12 * w_s1 * (t_s1)^3 + w_s1 * t_s1 * ((t_b + t_s1)/2)^2 + 1/12 * w_s2 * (t_s2)^3 +
    w_s2 * t_s2 * ((t_b + t_s2)/2)^2;
  I_y2 = 1/12 * w_b * (t_b)^3; ρ = (m_s + m_b)/(v_s1 + v_s2 + v); m = ρ * A;
  EI_y = (E_s1 * I_y1 + E_b * I_y2); l_0 = l + 0.0150 / 2;
  λ_1 = (-Fa/EI_y + ((Fa)^2/(EI_y)^2 + m ω^2/EI_y)^0.5)^0.5; λ_2 = (Fa/EI_y + ((Fa)^2/(EI_y)^2 + m ω^2/EI_y)^0.5)^0.5;
  a11 = (-ω^2 Cos[l λ_2] m_0 + ω^2 Cosh[l λ_1] m_0 + 2 Sinh[l λ_1] Fa λ_1 -
      l ω^2 Sinh[l λ_1] m_0 λ_1 + ω^2 Sinh[l λ_1] l_0 m_0 λ_1 + Sinh[l λ_1] EI_y λ_1^3 +
      2 Sin[l λ_2] Fa λ_2 - l ω^2 Sin[l λ_2] m_0 λ_2 + ω^2 Sin[l λ_2] l_0 m_0 λ_2 - Sin[l λ_2] EI_y λ_2^3);
  a12 = (ω^2 Sinh[l λ_1] m_0 - 2 Cos[l λ_2] Fa λ_1 + 2 Cosh[l λ_1] Fa λ_1 +
      l ω^2 Cos[l λ_2] m_0 λ_1 - l ω^2 Cosh[l λ_1] m_0 λ_1 - ω^2 Cos[l λ_2] l_0 m_0 λ_1 +
      ω^2 Cosh[l λ_1] l_0 m_0 λ_1 + Cosh[l λ_1] EI_y λ_1^3 - ω^2 Sin[l λ_2] m_0 λ_1 / λ_2 +
      Cos[l λ_2] EI_y λ_1 λ_2^2);
  a21 = (-ω^2 Sinh[l λ_1] I_G λ_1 + Cosh[l λ_1] EI_y λ_1^2 - l Sinh[l λ_1] EI_y λ_1^3 +
      Sinh[l λ_1] EI_y l_0 λ_1^3 - ω^2 Sin[l λ_2] I_G λ_2 + Cos[l λ_2] EI_y λ_2^2 + l Sin[l λ_2] EI_y λ_2^3 -
      Sin[l λ_2] EI_y l_0 λ_2^3);
  a22 = (ω^2 Cos[l λ_2] I_G λ_1 - ω^2 Cosh[l λ_1] I_G λ_1 + Sinh[l λ_1] EI_y λ_1^2 -
      l Cosh[l λ_1] EI_y λ_1^3 + Cosh[l λ_1] EI_y l_0 λ_1^3 + Sin[l λ_2] EI_y λ_1 λ_2 -
      l Cos[l λ_2] EI_y λ_1 λ_2^2 + Cos[l λ_2] EI_y l_0 λ_1 λ_2^2);
  determinant = a11 * a22 - a12 * a21;
  ω1 = FindRoot[determinant == 0, {ω, 5}];
  ω2 = FindRoot[determinant == 0, {ω, 390}];
  {ω1, ω2}]
```

```
GetC1star[Fa_, ω_] :=
 Module[{Cstar1, Cstar2},
  Cstar1 = a11 / a12; Cstar2 = a21 / a22; {Cstar1, Cstar2}]

GetC1[C1star_] :=
 Module[{C1},
  fz = (Cosh[λ1 z] - Cos[λ2 z]) - C1star * (Sinh[λ1 z] - λ1/λ2 Sin[λ2 z]);
  fl = (Cosh[λ1 z] - Cos[λ2 z]) - C1star * (Sinh[λ1 z] - λ1/λ2 Sin[λ2 z]) /. z → l;
  Dfl = D[fz, z] /. z → l;
  C1 = Sqrt[ m0 / ((∫0^l (m * (fz)^2) dz) + m0 * (fl + (l0 - l) * Dfl)^2 + IG * (Dfl)^2 ) ]
 ]

Getlambda[Fa_, ω_] := Module[{λ1, λ2},
  λ1 = (-Fa/EIy + ((Fa)^2/(EIy)^2 + m ω^2/EIy)^0.5)^0.5;
  λ2 = (Fa/EIy + ((Fa)^2/(EIy)^2 + m ω^2/EIy)^0.5)^0.5; {λ1, λ2}]
```

Appendix 6

Lists of Instruments ---- Experimental Work

The instruments used in the experimental work are listed below and their photographs are shown in Fig A.6.1.

- Laser Vibrometer: Model Polytech OFV 303
- Electro-dynamics Shaker: LDS Model V 455
- Vibrometer Controller: Model Polytech OFV 3001
- Power Amplifier: LDS Model PA 1000L
- Spectrum Analyzer: HP 3582A
- Charge Amplifier: DJB Model RM/04
- Function Generator: TTi Model TG 320
- Oscilloscope: Tektronix TDS 1012B
- Accelerometer: DJB A 23/E
- Power Supply Unit: Palstar PS – 30M

(1) Laser Vibrometer

(2) Electro-dynamics Shaker

(3) Vibrometer Controller

(4) Power Amplifier

(5) Spectrum Analyzer

(6) Charge Amplifier

(7) Function Generator

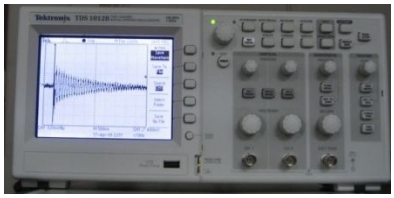

(8) Oscilloscope

(9) Rheostat

(10) Ammeter

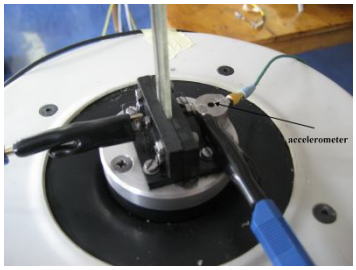

(11) Accelerometer

(12) Power Supply Unit

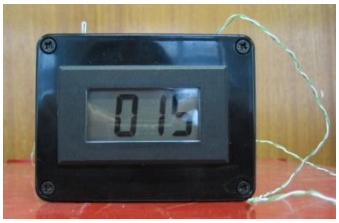

(13) Thermo-couple

Fig A.6.1 Photos of the instruments used in tests